

2006

## Heat treatment study of titanium-boron alloys and thermal stability of the TiB phase

Dale Joseph McEldowney  
*University of Dayton*

Follow this and additional works at: [https://ecommons.udayton.edu/graduate\\_theses](https://ecommons.udayton.edu/graduate_theses)

---

### Recommended Citation

McEldowney, Dale Joseph, "Heat treatment study of titanium-boron alloys and thermal stability of the TiB phase" (2006). *Graduate Theses and Dissertations*. 4303.  
[https://ecommons.udayton.edu/graduate\\_theses/4303](https://ecommons.udayton.edu/graduate_theses/4303)

This Dissertation is brought to you for free and open access by the Theses and Dissertations at eCommons. It has been accepted for inclusion in Graduate Theses and Dissertations by an authorized administrator of eCommons. For more information, please contact [mschlange1@udayton.edu](mailto:mschlange1@udayton.edu), [ecommons@udayton.edu](mailto:ecommons@udayton.edu).

# **Heat Treatment Study of Titanium-Boron Alloys and Thermal Stability of the TiB Phase**

Dissertation

Submitted to

The School of Engineering of the

UNIVERSITY OF DAYTON

In Partial Fulfillment of the Requirements for

The Degree

Doctor of Philosophy in Materials Engineering

by

Dale Joseph McEldowney

UNIVERSITY OF DAYTON

Dayton, Ohio

August 2006

## Heat Treatment Study of Titanium-Boron Alloys and Thermal Stability of the TiB Phase

### APPROVED BY:




Eylon, Daniel, D.Sc.  
Committee Chairman  
Director and Professor,  
Graduate Materials Engineering



Murray, T. Paul, Ph.D.  
Committee Member  
Professor, Graduate Materials  
Engineering Program



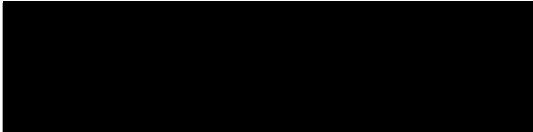
Voevodin, Andrey, Ph.D.  
Committee Member  
Professor, Graduate Materials  
Engineering Program



Shaughnessy, Gerald,  
Committee Member  
Professor, Department of  
Mathematics



Seshacharyulu Tamirisakandala, Ph.D.  
Advisor  
Assistant Research Professor,  
Mechanical Engineering, Ohio University



Miracle, B. Daniel, Ph.D.  
Advisor  
United States AFRL/MLLM  
Wright-Patterson AFB



Moon, L. Donald, Ph.D.  
Associate Dean  
Graduate Engineering Programs and  
Research, School of Engineering



Saliba, E. Joseph, Ph.D., P.E.  
Dean  
School of Engineering

© Copyright by

Dale Joseph McEldowney

All rights reserved

2006

## ABSTRACT

### Heat Treatment Study of Titanium-Boron Alloys and Thermal Stability of the TiB Phase

McEldowney, Dale Joseph  
University of Dayton, 2006

Advisor: Dr. Daniel B. Miracle

Titanium-Boron alloys have gained significant interest in the last few years, especially in the aerospace community where emphasis has been on developing more structurally efficient materials. The new class of alloys achieves higher strength and stiffness, up to 60% in some cases, than most conventional titanium alloys utilized today. An *in-situ* reaction precipitates the important needle-like TiB reinforcement phase, which is responsible for the tremendous increase in properties. Strengths as high as 1700MPa and stiffness near 200 GPa have been realized in laboratory mechanical testing. The compatibility of the TiB phase with the surrounding alloy, and the low solid solubility provide a stable material system, yet much is not known in regards to the thermal stability of the TiB phase. As it is well understood that heat treatment conditioning of conventional Ti alloys can produce a wide array of microstructural and property results, therefore, it

is expected that Ti-B alloys may respond to thermal exposure in similar fashion. Two alloys, Ti-6Al-4V-1.0B and Ti-6Al-4V-1.7B, produced via a pre-alloyed powder metallurgy approach and subsequent extrusion, were selected for this research. The goal of this research was two-fold, i) to analyze and quantify the thermal stability of the *in situ* TiB phase present in a pre-selected Ti-B alloy, ii) to study the microstructural-mechanical property response of the two pre-selected Ti-B alloys via exposure to pre-determined heat treatments and compare to conventional Ti-6Al-4V.

## ACKNOWLEDGEMENTS

I would like to thank everyone that made this work possible, whether through financial support, technical guidance, or moral support along the way. First, I would like to extend my gratitude for the financial support from the United States Air Force Research Laboratory, Materials and Manufacturing Directorate at Wright-Patterson AFB, OH, specifically through Dr. Daniel B. Miracle at Wright-Patterson AFB and contracted via the Southwest Ohio Council for Higher Education (SOCHE). Also, I am grateful for the financial support from the University of Dayton Graduate Materials Engineering Department under Dr. Danny Eylon and tuition and fellowship assistance from the Dayton Area Graduate Studies Institute (DAGSI). Without the aforementioned financial assistance, known of this would have been possible.

I would like to thank my advisory committee for their time commitment and advice during my research and dissertation: Dr. Daniel Miracle and Dr. Sesh Tamirisa my prime technical advisors, Dr. Danny Eylon my chairman, Dr. P.T. Murray, Dr. Andrey Voevodin, and Professor Gerald Shaughnessy. In particular Dr. Daniel Miracle and Dr. Sesh Tamirisa deserve special thanks for their untiring contributions and guidance they made throughout my research. I appreciate their attention to detail

which was very rewarding in the end. Finally, not only is their endless advice acknowledged and appreciated, I am grateful for their friendship.

I would also like to thank the chief metallographer at Wright-Patterson AFB, Mr. Bob Lewis for his assistance in metals preparation and techniques, and Mr. John Murry, heat treat technician, for quick turnaround on my experimental efforts. Also, I would like to thank Mrs. Cheryl Seitz, program administrator at the University of Dayton, for her guidance in the PhD administrative process.

Most of all, I would like to thank my family, especially my wife, Lisa, for her undying love and support through the entire PhD process. Her belief in my abilities gave me strength beyond what any words can describe.



## TABLE OF CONTENTS

ABSTRACT.....	iii
ACKNOWLEDGEMENTS.....	v
LIST OF ILLUSTRATIONS.....	x
LIST OF TABLES.....	xiv
CHAPTER	
I. INTRODUCTION.....	1
Titanium Alloys for Structural Applications.....	1
Tailorability via Composition and Microstructure.....	3
Tailorability via Heat Treatment.....	4
Tailorability via Composition.....	6
Current Status of Conventional Titanium Alloys.....	8
Titanium Metal Matrix Composites (Continuous and Discontinuous).....	10
Needs and Benefits of Advanced Titanium Alloys.....	13
Titanium Alloys Modified with Boron (Ti-B Materials).....	14
History of Ti-B Materials Technology.....	14
Processing routes for Ti-B materials.....	19
Ti-B Material System.....	25
TiB Phase.....	28
Crystal Structure and Properties.....	28

Size, Morphology and Distribution.....	31
Objectives and Approach.....	33
Heat Treatment Study of Ti-6Al-4V-1.0 and Ti-6Al-4V-1.7B....	33
Thermal Stability of TiB Phase.....	34
Significance of Research.....	36
II. EFFECT OF HEAT TREATMENT ON MICROSTRUCTURE AND PROPERTIES OF Ti-6Al-4V-B ALLOYS.....	37
Summary.....	37
Experimental.....	38
Program Materials.....	38
Thermo-mechanical processed material.....	39
Heat Treatments.....	42
Metallography.....	43
Mechanical Testing.....	44
Fractography.....	45
Results and Discussion.....	45
Starting Microstructure.....	45
Microstructures post-Heat Treatment.....	52
Mechanical Properties.....	56
Elastic Modulus.....	59
Strength and ductility.....	60
Fractography.....	62

Strength and Stiffness Modeling.....	65
Conclusions.....	77
Recommendations.....	79
III. THERMAL STABILITY OF TiB PHASE.....	81
Summary.....	81
Experimental.....	82
Program Materials.....	82
Annealing Parameters.....	84
Metallography and Preparation.....	84
Image Analysis and Microstructural Quantification .....	85
Results and Discussion.....	87
Starting Microstructure.....	87
Annealing Parameters.....	89
Microstructural Evolution.....	89
Diameter and Length.....	89
Point density and Interparticle spacing.....	95
Origin of nano-TiB.....	97
Coarsening Kinetics Modeling.....	98
Conclusions.....	107
Recommendations.....	109
REFERENCES.....	110

## LIST OF ILLUSTRATIONS

1. SEM micrographs of various Ti alloy microstructures.....	4
2. Titanium-Boron binary phase diagram.....	14
3. Image of Toyota automotive intake and exhaust valves.....	17
4. Flow diagram of PA and BE powder processing.....	19
5. SEM micrographs comparison of PA and BE powder size, morphology, microstructure.....	20
6. SEM micrographs of PA and BE as-compacted.....	21
7. SEM micrograph of PA in the HIP+Forged condition.....	22
8. SEM micrograph of as-extruded microstructure indicating aligned micron TiB.....	22
9. SEM micrograph of as-cast Ti-6Al-4V microstructure.....	23
10. SEM micrograph of transverse interface as-extruded Ti-6Al-4V can and Ti-6Al-4V-1.7B.....	25
11. Structural efficiency diagram of various engineering materials.....	27
12. Crystal structure (B27) of TiB Phase.....	29
13. TEM image of nano-TiB.....	31
14. SEM micrograph illustrating presence of primary TiB.....	32

## LIST OF ILLUSTRATIONS (CONTINUED)

15. SEM image illustrating randomly distributed TiB.....	33
16. Plot of starting powder particle size distribution.....	40
17. SEM micrographs of powder starting PA powder size, morphology, and microstructure.....	40
18. Process flow diagram used in study.....	41
19. Photograph of typical Ti-6Al-4V-xB compacted powder in Ti-6Al-4V canister.....	41
20. Photograph of typical as-extruded Ti-6Al-4V-xB material.....	41
21. Schematic of heat treatment schedules used in study.....	42
22. Photograph of representative round tensile specimen.....	44
23. SEM micrograph and mating schematic of Ti-6Al-4V canister and PM Ti-6Al-4V-xB as-extruded.....	46
24. SEM images of starting microstructures of Ti-6Al-4V-1B & Ti-6Al-4V- 1.7B in longitudinal and transverse.....	47
25. SEM of as-received wrought Ti-6Al-4V mill material.....	49
26. SEM micrographs illustrating presence of tri-modal TiB.....	50
27. SEM micrographs illustrating random nano-TiB post-extrusion....	51
28. SEM micrographs after various heat treatments.....	53
29. Plots of tensile stress-strain curves after heat treatments.....	57
30. Plots of tensile properties after heat treatments.....	58
31. Fractographs of tensile tested specimens.....	63

## LIST OF ILLUSTRATIONS (CONTINUED)

32. Schematic illustration of elastic and plastic contributions of individual phases.....	66
33. Plot of elastic modulus as a function of vol% TiB.....	73
34. Flow diagram of the steps used in thermal stability study of the TiB phase.....	82
35. Schematic of anneal times and temperatures in study.....	84
36. Modified SEM images illustrating TiB length and diameter capturing technique.....	86
37. SEM images of material starting microstructures.....	88
38. SEM micrographs illustrating nano-TiB presence.....	89
39. Thresholded SEM images of heat treated Ti-6Al-4V-1.7B in transverse direction.....	91
40. Plots of equivalent diameter and average length distributions as a function of time and temperature.....	93
41. Plots of mean equivalent diameter at various times as a function of temperature.....	94
42. Plots of mean average length at various times as a function of temperature.....	94
43. Plots of point density and interparticle spacing for TiB phase...	96
44. SEM images illustrating dissolution of nano-TiB as a function of time and temperature.....	97

## LIST OF ILLUSTRATIONS (CONCLUDED)

45. Plot of LSE equation up to $n=5$ for 1100 C.....	104
46. Plot of effective diameter as a $f(t,T)$ .....	104
47. Plot of modified LSW model.....	105

## LIST OF TABLES

1. Property and attribute comparison of hard particles.....	30
2. Summary of TiB size-scale and corresponding attributes.....	32
3. Chemical composition of PA powder used in study.....	38
4. Heat treatment conditions used in study.....	42
5. Summary of yield strength individual mechanistic contributors....	67
6. Summary of predicted stiffness using various models.....	67



## CHAPTER I

### INTRODUCTION

#### Titanium Alloys for Structural Applications

Titanium (Ti) and its alloys have become increasingly important engineering materials with properties that satisfy a variety of applications. Titanium exhibits an extraordinary balance of mechanical and physical properties that appeal to many sectors. Ti alloys have found a role in medical applications with such uses as hip and knee joint replacements, vascular stents, and other prosthetics. The combination of biocompatibility, strength, and modulus of Ti alloys make them a better candidate for implants than other materials that have been used in the past (i.e. cobalt alloys and stainless steel). The aerospace industry has found titanium to be one of the most important materials available today. Ti alloys ( $\rho=4.5 \text{ g/cc}$ ) weigh 50% less than steel and superalloys, are 2-3 times stronger (up to  $\sigma_y= 1200\text{MPa}$  (174ksi)) than aluminum, and have better corrosion-resistance than most metals. [1] The high strength and superior corrosion-resistance provide desired properties for use in aerospace, marine, and chemical environments.

The ability to exhibit high specific strength and stiffness at relatively higher temperatures (up to 550 °C), while possessing high corrosion-resistant properties, allows Ti alloys to be used in many commercial and military aircraft applications. Gas turbine engines have become one of the major areas for use of Ti alloys, along with structurally important regions of the aircraft that call for high modulus. In the Air Force F-22 Raptor some 42% of all structural weight is composed of Ti. In the aft fuselage alone, almost two-thirds of the weight is Ti [2]. During the life of the Ti industry, various compositions have had transient usage, but one alloy, Ti-6Al-4V, has been consistently responsible for about 45% of industry application [3], where aerospace accounts for about 80% of this usage [4].

Rotating components within the turbine engine require a material that can maximize strength efficiency and metallurgical stability at elevated temperatures. These alloys also must exhibit low creep rates along with predictable behavior with respect to stress rupture and low cycle fatigue. In order to reproducibly provide these properties, often the user requires stringent specifications on controlling the homogeneity of the microstructure and elemental control of the alloy. This demands tight melt process controls to avoid such detrimental effects as alpha segregation, tramp inclusions and unhealed ingot porosity [5].

Within this realm of requirements for high temperature exposure applications, microstructural stability and thermal response of the material is quite important. Grain coarsening often leads to a reduction in properties. For example, static grain growth, particle coarsening, spheroidization of a lamellar microstructure, and other diffusional processes may lead to substantial losses in both first and second tier properties, such as yield strength and creep resistance, during service exposure [6]. Therefore, a considerable amount of attention has focused on the phenomenological and mechanistic descriptions of such changes in microstructure [7,8]. Such emphasis as understanding the effects of various deformation parameters on dynamic globularization of the alpha phase in an alpha-beta Ti have been investigated extensively [9-13]. These studies have focused primarily on conventional Ti alloy microstructures without the addition of any dispersion-strengthening or *in situ* precipitated phases.

#### Tailorability via Composition and Microstructure

Certainly one of the most important characteristics of Ti alloys is the ability to tailor the morphology and microstructure to suit potential applications that require specific properties. Most often this is accomplished via thermo-mechanical processing (TMP), post-heat treatment conditioning, or a combination of both. By working and/or

heat treating alpha+beta alloys below or above the beta transus (100% beta transformation temperature), substantial microstructural changes can be produced. The wrought processing of high-integrity components from conventional alpha+beta titanium alloys often involves a series of hot working steps and final heat treatment [14]. Figure 1 illustrates the

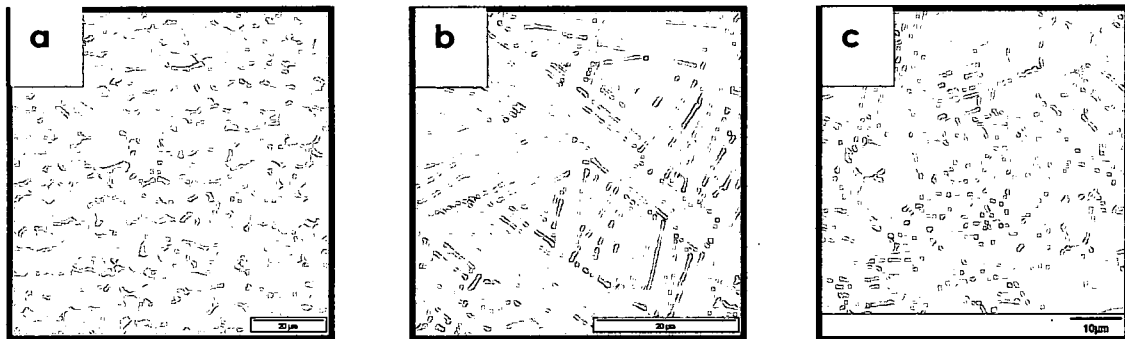


Figure 1 SEM micrographs of an alpha+beta Ti alloy illustrating a variety of microstructures: a) equiaxed  $\alpha$ ; b) lenticular  $\alpha/\beta$  (Widmanstätten); and c) equiaxed  $\alpha$  with transformed beta (duplex).

tailorability of a typical Ti alloy, Ti-6Al-4V, and some potential microstructures that may be produced via TMP and subsequent post-heat treatment conditioning. These particular micrographs represent only some of the possible microstructures that may be achieved in order to fit specific application requirements.

#### *Tailorability via Heat Treatment*

Often the final heat treatment of an alpha+beta titanium (i.e. Ti6Al-4V) is accomplished at a temperature dependent on the service requirements [15]. For instance, an application that may require high strength and

ductility, and high temperature low-cycle fatigue (LCF) resistance, a fine-grained equiaxed- $\alpha$  type microstructure (see Fig 1a) via a post-heat treatment in the  $\alpha$ + $\beta$  phase region would be desired. The combination of refined grain size and morphology would assure optimum property balance for the aforementioned criteria. To optimize fracture toughness, on the other hand, a heat treatment of  $\beta$  annealing, above the  $\beta$  transus, followed by air cooling (AC) or furnace cooling (FC) to produce a Widmanstätten or basketweave-type microstructure may be completed (see Fig. 1b). The lamellar structure varies with cooling rate, ranging from colonized platelike  $\alpha$  at a low cooling rate, a basketweave morphology at an intermediate cooling rate, Widmanstätten at a high cooling rate, to martensite when quenched in water [16,17].

The mill anneal condition is a general purpose treatment given to all mill products, and accounts for the highest percentage of Ti-6Al-4V product used commercially [18]. Mill annealing the material can also be an intermediate step prior to machining operations and final heat treatment, as machinability of the material is optimum at this condition. The treatment produces a globular structure of  $\beta$  in an  $\alpha$  matrix, whereby the ductility is optimized.

Another annealing treatment, termed  $\beta$  anneal, is used to maximize damage tolerance properties (i.e. fracture toughness, fatigue

crack propagation resistance), with a slight loss in ductility as compared to other anneal conditions. A lamellar microstructure is produced via beta anneal heat treatment consisting of plates of alpha phase separated by beta phase.

Duplex anneal is often used to gain a balance of properties by combining the strength-gaining contribution of equiaxed-alpha structure with damage tolerance characteristics of intermixed lamellar structure. Another important heat treatment, solution treatment and age (STA), is used to take advantage of the high hardenability of alpha+beta alloys, and is often used to maximize strength of an alloy.

#### *Tailorability via Composition*

The category (which encompasses the various compositions) of the particular Ti alloy most often dictates the application in which the alloy is used. Alpha and near-alpha alloys (i.e. Ti-6Al-2Sn-4Zr-2Mo-0.1Si) are often used for high temperature applications. These alloys contain higher amount of alpha-stabilizing elements such aluminum and tin, which increase the temperature at which the alpha phase is stable. The main reason for use in higher temperature applications is due to their better resistance to creep and high temperature oxidation than beta or alpha+beta alloys. The presence of miniscule amounts of beta phase in an alpha or near-alpha alloy provide a favorable response to higher

temperatures, as the beta phase has poor high temperature creep resistance. Inevitably, when a metal has good creep resistance, the formability or forgeability is most often low. With fewer slip systems than a bcc alloy and lack of phase transformation, the hcp structured alpha does not respond to thermo-mechanical processing (TMP) as well as the bcc-structured beta or alpha+beta alloys (i.e Ti-6Al-4V) (above the beta-transus). This results in a greater tendency towards forging defects. Small reductions during mechanical deformation and frequent reheating can minimize these problems [19].

In general, as the content of beta stabilizer increases, the hardenability increases (i.e. Ti-5Al-2Sn-2Zr-4Mo-4Cr better than Ti-6Al-4V) [20]. Extra-low-interstitial (ELI) grades, with controls on amount of elements such as O, Fe, and C, are often used for higher fracture toughness, higher ductility and better corrosion resistance. It is well known that of all interstitial elements, oxygen possesses the greatest impact on properties with minimal additions, therefore, control is definitely a necessity. Alpha+beta alloys are most often used in aerospace applications, pressure vessels, aircraft turbine disks and blades, marine and chemical environments, and medical implants. The combination of high strength and toughness, along with excellent corrosion resistance, make these alloys ideal for a variety of applications.

Beta alloys, which make up a smaller percentage of the Ti alloys utilized today, are generally easier to form than alpha or alpha+beta alloys, but possess relatively poor low and high temperature properties. Yet, in the fully aged condition, with finely dispersed alpha grain structure, the beta alloys possess the highest strength of any group of Ti alloys. These metastable alloys can be cold formed more readily than alpha and alpha+beta alloys making them good candidates for sheet applications. The Blackbird SR-71 aircraft is a prime example of beta alloy or metastable alloy (i.e. Ti-13V-11Cr-3Al) use, and was actually the first use of beta Ti alloys in aerospace structural application [21].

Indeed, microstructural manipulation plays a very important role in the mechanical properties of Ti alloys, and depends primarily on the chemical composition, processing history and thermal treatment procedures [22-24].

### Current Status of Conventional Titanium Alloys

Since the 1940s when it became apparent that Ti was an important metal with a wide potential, Ti has become increasingly prominent as an engineering metal. Commercial Ti production soon began in earnest in the United States, and by the 1950s U.S. production of Ti mill products was more than 6 million kg/yr [25]. As soon as titanium appeared attractive for military aircraft in the early 1950's, a large effort ensued in alloy



development [26]. By 1997 U.S. mill product shipments peaked at over 27 million kilograms (60 million pounds) [27]. Even though the aerospace industry continually represented the highest usage sector at approximately 40% by 1997, other markets began to expand use in Ti. Some major examples include the industrial/consumer market in such applications as golf clubs and baseball bats, the medical field in prosthetics and joint replacement needs, and the chemical sector in pumps, piping and tanks. A recent analysis conducted and presented by the International Titanium Association in 2004 on Ti alloy worldwide markets suggests the commercial aerospace and military sectors now hold a smaller market combined at approximately 45% versus 55% for industrial/consumer goods [28]. This does suggest a decrease in Ti usage by the aerospace sector after peaking in the late 1990s, but also a trend in widening of Ti usage by others sectors. The future does, however, look bright for Ti production with the advancement of the aerospace sector's future commercial aircraft industry in the Boeing 787 and Airbus A380 new jumbo jetliners. In fact, the Boeing 787 has the potential to incorporate more Ti in its design than all of the past major commercial Boeing aircraft combined [29]. The downside still remains the cyclical nature of Ti demand, as shown by the graph on U.S. Ti mill shipments [30], and the higher cost as compared to historically used engineering metals steel and aluminum.

Today, all Ti categories (i.e. alpha, alpha/beta, etc.) are seeing at least some usage in one sector or another, yet most of these alloys are used in more niche-type applications meeting specific needs (i.e. fracture-critical, low modulus, etc.). The most frequently used Ti alloy used today still remains the conventional alpha/beta alloy Ti-6Al-4V, with CP Ti second due primarily to its better corrosion resistance. History shows the popular Ti-6Al-4V alloy was a result of early research [31], with introduction in 1954, and was immediately designed into existing engines and airframes. Today, about 55% of the USA production is in Ti-6Al-4V, most of it in a billet, sheet or plate form. In fact, about 80% of current total production is in CP and Ti-6Al-4V, two compositions that were developed and used nearly 50 years ago [32]. With increasingly higher demands on conventional Ti alloys, design margins becoming tighter due to better NDE techniques, and a promising outlook for Ti market demands, an apparent need has arisen for a new Ti material class that can fulfill the needs without sacrificing the inherent benefits of conventional Ti alloys used today.

#### Titanium Metal Matrix Composites (Continuous and Discontinuous)

Researchers turned their attention in the 1950s and 1960s to a class of materials known as metal matrix composites (MMCs) with initial motivation to dramatically extend the structural efficiency of metallic materials while retaining their advantages [33]. The majority of work in the

early stages focused on enhancing aluminum with fiber reinforcements such as SiC. Much research effort was conducted throughout the 1960s and 1970s on fiber-reinforced aluminum and titanium MMCs. Issues associated with processing, fiber damage, and fiber-matrix interactions were overcome to produce useful materials [34]. Ti alloys, primarily Ti-6Al-4V, have been used in combination with SCS-6 silicon carbide monofilament reinforcements for MMC applications with reasonable success [35]. However, these continuously reinforced materials were best suited for more niche-type applications, primarily due to their anisotropic properties and higher cost. While efforts continued in the way of continuously reinforced metals, progress was made in the use of discontinuously reinforced MMCs in the 1980s. A major reason for the shift in focus to discontinuously reinforced MMCs (i.e. via particulates, short fibers) primarily concentrated on the potential to achieve relatively isotropic properties. Another major advantage for using discontinuously reinforced materials over continuously is that the processing techniques are generally the same as those used in typical Ti alloy processing, yet still retaining the added benefits of a reinforcing phase.

The concept of MMCs is based on utilizing the best characteristics of two separate materials, such as the ductility and toughness of metallic matrices and the strength and stiffness of a reinforcement phase, in order to produce an overall material with superior bulk properties compared to

unreinforced metals [36]. Combining the individual attributes of the separate phases allows for a seemingly infinite number of possibilities in terms of tailorability of the material to fit the specific demands of the application. Emphasis has been on developing metals with higher specific properties for use in such applications as aircraft structural components and automotive engine and wheel components which require high strength and modulus properties without added weight. For example, a significant amount of work has been done in Japan to develop discontinuously reinforced Ti for automotive applications [37-39]. Using an elemental powder approach in processing the titanium, reduction in the overall cost of the product was achieved. Some of the negative aspects of the MMC approach include increases in cost as compared to traditional metals, and often a reduction in fracture properties. Today, the class of MMCs can be considered a relatively established material system, and the continuously and discontinuously reinforced metals class of materials was able to provide some contribution to fill the void for higher specific property materials, however, a need still exists for advanced engineering metals to meet the need of ever-increasing demands.

### Needs and Benefits of Advanced Titanium Alloys

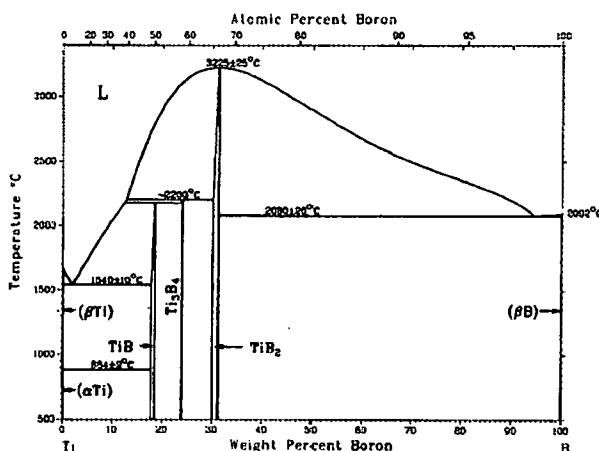
While the conventional Ti alloy material class and MMC class of materials have taken great strides over the past few decades, and continue to gain recognition as reliable materials, there still remains a quest for titanium alloys that possess better combination of properties at a higher level. A push towards higher structural efficiency continues, while focus on driving the overall material cost down. Strides have been made in cost reduction of titanium, primarily in the extraction and mill processing arenas, and great potential still remains. Such extraction processes as the Cambridge and Armstrong processes have potential to reduce the overall Ti production costs. However, a more structurally efficient titanium alloy class would provide for great opportunities where weight is an issue, especially in the aerospace sector. For example, an increase in strength and stiffness by as much as 10-20% over conventional Ti alloys, without debit in other properties could open up new applications in the jet engine industry where heavier metals are currently used. Advances in the properties of cast or powder metallurgy (P/M) Ti alloys may allow substitution for components that are currently cast plus wrought and machined, providing an approach for reduced overall cost. There is an emerging class of advanced Ti alloys, known as the Ti-B alloy and composite system, which is gaining tremendous momentum towards

potential replacement for currently used conventional titanium alloys, possibly even heavier engineering metals.

## Titanium Alloys Modified with Boron (Ti-B Materials)

### History of Ti-B Materials Technology

Research and development of Ti-B alloys was initiated in the 1950s. In 1953, the United States Army sponsored work by New York University in the area of titanium-boron and titanium-nitrogen systems. Paltry, Margolin and Nielsen [40] investigated the binary and ternary phase diagrams for the aforementioned alloys via delineation from microstructure, x-ray, and melting point data. The Ti-B binary diagram, Fig.



2, illustrates the stable and metastable phases, and the eutectic point for formation of TiB. The TiB phase is an intermediate phase between Ti and TiB<sub>2</sub>.

In 1962 the Royal Aircraft

Establishment conducted

Figure 2 Phase diagram of Ti-B system. [3]

experiments to study the modulus of titanium alloys produced via additions of boron. Brown et al [41] reported increases in Young's Modulus at an average rate of 14.5 MPa, or 12% for each 1 wt% boron added in the range investigated. The alloys investigated were

predominately  $\alpha$ -titanium alloys, Ti-Al with the addition of B. It was stated that an addition of up to 2 wt% B resulted in approximately 30% increase in modulus, with reasonable ductility, 7-10 %elongation. Strength was also reported as increasing with the addition of boron, achieving up to 1020 MPa. This study reported a eutectic point at approximately 2 wt% B. Conclusions indicated the alloys studied as having potential for applications requiring much higher stiffness while retaining ductility, 7-10% elongation.

Research subsided for Ti-B alloys after the early 1960s, until commercial applications were finally realized in non-fracture critical applications in the 1980s [42]. Applications such as ice skate blades and pocket knives relied on the advantages of strength, stiffness, hardness, and wear resistance over conventional steel. Abkowitz et al [43] reported the superior sharpness retention of a Ti-B alloy (CermeTi-B-5) over the typically used high-performance steel material.

In the mid-1990s, Crucible Research in Pittsburgh, PA, USA investigated the possibility of mechanical property improvements in several Ti-alloys enhanced with boron. Crucible utilized a P/M approach with subsequent thermo-mechanical processing. Improvement was reported in strength and stiffness over the same alloys without B, however, ductility was somewhat discouraging at 5 %elongation maximum.

Research was conducted on adding interstitial elements to produce strengthening precipitates. Abkowitz et al [44] studied the effects of TiC, SiC, TiAl, and TiB<sub>2</sub> particulate reinforcements via the blended elemental (BE) powder metallurgy approach, concluding the "composites" could not be used for automotive industry due to their high cost and insufficient performance.

In the mid-to-late 1990s, Boeing and NASA jointly investigated a replacement alloy for typical Ti-6Al-4V, which included an alloy of Ti-6Al-4V with 0.6 wt% B, to be used in a High Speed Civil Transport (HSCT) application [45]. The intent of the study was to develop an extruded Ti alloy with 20% higher modulus than Ti-6Al-4V while maintaining or improving other relevant mechanical properties. Several alloys were investigated in the study along with the B-containing alloy. The B-containing alloy exhibited acceptable formability properties, and met the increased stiffness requirements. However, marginal ductility in the transverse direction, and low fatigue initiation characteristics compared to Ti-6Al-4V, coupled with drastic cuts in the HSCT program, discontinued effort on these alloys.

In 1998 the first significant commercial application of a titanium-boron alloy) was realized when Toyota Motor Corporation adopted simultaneously the intake and exhaust valve made of  $\beta$ -titanium based alloy with boron in the Altezza, Fig. 3. [46] In this



particular application, a novel BE P/M approach was used to produce a cost-effective alloy product that typically demands low cost steel. The material was specifically designed for mechanical properties at elevated temperatures up to 875 °C. The weight reduction while maintaining exceptional strength and stiffness properties provides

increase in engine performance. Over 500,000 valves have been manufactured and incorporated into market use since 1998, however, cost still remains a factor in future use expansion as the TiB reinforced component costs approximately twice that of steel. Titanium automobile components will never find continued practical application unless they can compete in cost/performance with steel components. [47]

Over the last decade, and especially the last five years there has been great strides in Ti-B alloy development, utilizing the effects of the TiB phase for enhanced properties. The United States Air Force Research Laboratory (AFRL) at Wright-Patterson AFB has taken on a lead role in much of the Ti-B alloy development. Utilizing the powerful grain

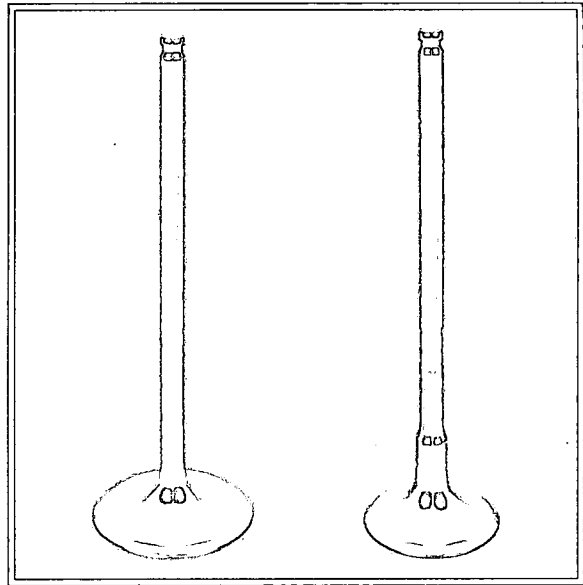


Figure 3. Ti-B alloy intake and exhaust valves used in the Toyota Altezza [64]

refinement attributes of B in Ti alloys has led to a number of important advances. For instance, the grain size of as-cast Ti-6Al-4V was shown to reduce by an order of magnitude with the addition of 0.1 wt% B, and similar trends were observed in other alloys [68]. Using a variety of techniques, the influence of B on the  $\beta$  transus of Ti-6Al-4V was established. It was determined that the addition of B provides grain stabilization above the  $\beta$  transus, and ultimately increasing the  $\beta$  transus by approximately 60 °C [54]. The usefulness of this stabilization behavior above the beta transus has led to superplastic behavior in Ti-B alloys above the beta transus [52]. This influence of B on the alloy microstructure and stability provides a need to establish how a B-modified Ti-6Al-4V alloy will respond to conventional heat treatments. Other work at AFRL has centered on commercialization of the Ti-B alloy technology through the aforementioned attributes. For instance, the superplastic behavior of the Ti-B alloy has important implications in potential applications that may demand high formability of sheet or plate. Other instrumental advances in Ti-B technology by the AFRL will be mentioned throughout the remainder of the paper.

## Processing Routes for Ti-B Materials

Much of the past research has centered on P/M processing of titanium-boron materials. Ti-B alloys can be produced and processed using conventional P/M techniques of pre-alloyed (PA) and blended elemental (BE) powders. The flow diagram in Fig 4 illustrates the

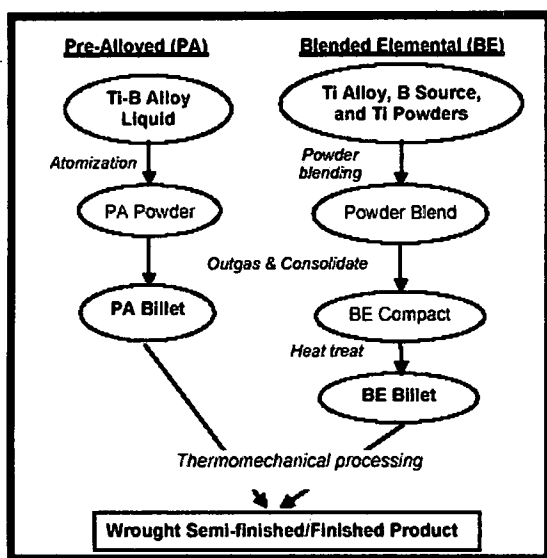


Figure 4 Flow diagram of two powder metallurgy approaches to Ti-B alloy production. [52]

comparative processing steps of both P/M techniques. The BE approach is typically completed via blending appropriate amounts of commercially available powders of Ti alloy and  $\text{TiB}_2$ . After adequate blending of the elemental powders, the powder can then be filled into a container for compaction or hot isostatic pressing (HIP). The

compaction process is carried out after prior degas and seal of the container. A final heat treatment is performed on the compact in order to complete the chemical conversion process of  $\text{Ti} + \text{TiB}_2 \rightarrow 2\text{TiB}$ .

Additional Ti is added to the powder blend in order to replenish the elemental Ti that is scavenged by the  $\text{TiB}_2$  during the conversion process.

A low-cost BE technique developed by Saito et al. [48] is presently used to

produce near-net shape automobile valves, (Fig. 3). Typical powder morphologies are shown in Fig.5(b).

The pre-alloyed (PA) approach is another relatively cost-effective approach to produce Ti-B alloys. In the PA approach, the powder is often produced via inert gas atomization or some other commercially available rapid solidification technique of the master Ti alloy and B source (most often in the form of  $TiB_2$ ). The boron completely dissolves into the melt and is precipitated as TiB in the solid state during rapid solidification of the powder. Fig. 5a shows a typical PA Ti-6Al-4V-1.7B powder morphology and cross-section of a powder particle revealing the presence of TiB that is

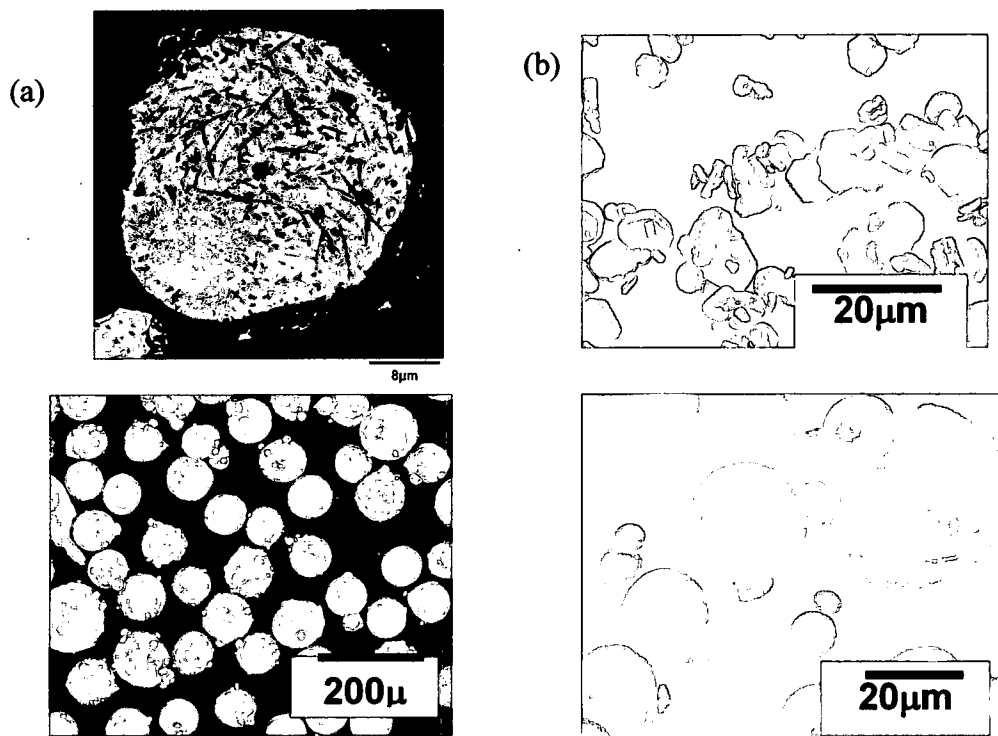


Figure 5 Size and morphologies of typical (a) PA gas-atomized (and cross-section) Ti-6Al-4V-1.7B, and (b) BE  $TiB_2$  and Ti-6Al-4V powders, respectively.

randomly distributed in the microstructure. The PA powder is filled into a container that is subsequently degassed and sealed in like manner as in the BE process, and compacted under heat and pressure. The densification of the powder occurs during the hot compaction process (e.g. HIP). Since TiB is already present in the PA powder particle itself, no further heat treatment is necessary for conversion.

Figures 6a and b illustrate the microstructural differences realized by the BE and PA processes. Note the coarser TiB phase (dark particles) in



Figure 6 SEM image of Ti-6Al-4V-1.7B P/M (a) blended elemental (BE), and (b) pre-alloyed (PA) microstructure as-compacted.

the BE, which is typical of this technique. The PA approach results in a finer TiB phase of approximately 5x, yet a similar, but smaller equiaxed- $\alpha$  matrix microstructure. The PA approach is limited to the hypoeutectic composition to avoid formation of coarse primary TiB. The BE approach, on the other hand, provides the ability to produce high stiffness MMCs by introducing higher volume fractions of TiB without encountering primary TiB

formation. Compositions with as high as 40vol% TiB produced via BE P/M approach have shown Young's modulus, E, up to 200 GPa [49]. Both P/M techniques have shown to have potential in commercial applications.

The densified billet can be further subjected to standard thermo-mechanical processing techniques such as forging, rolling and extrusion.

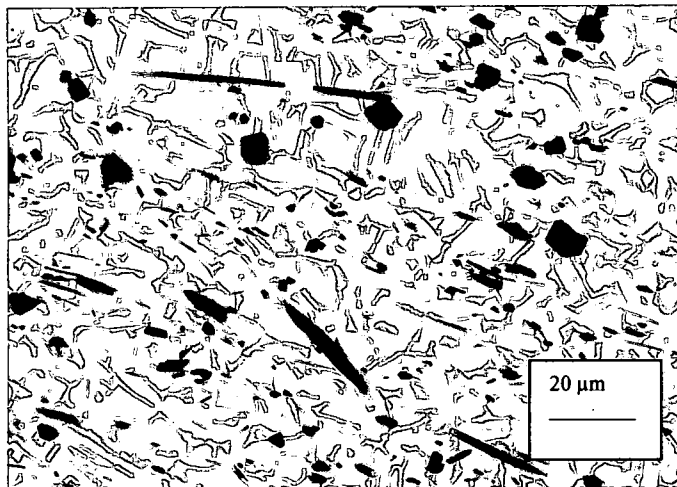


Figure 7 SEM microstructure of Ti-6Al-4V-1.7B PA P/M in the HIP+forged condition.

uniformly and randomly distributed throughout the matrix after forging.

Subjecting a billet to hot extrusion (see Fig.8) produces a quite different microstructure than a forged billet.

The TiB precipitates align along the extrusion direction. The micrometer-size TiB whiskers follow this trend,

The ability to form titanium-boron product via forging was demonstrated. [50] Fig. 7 depicts the typical microstructure attained via PA powder compaction and subsequent forging.

The TiB whiskers remain

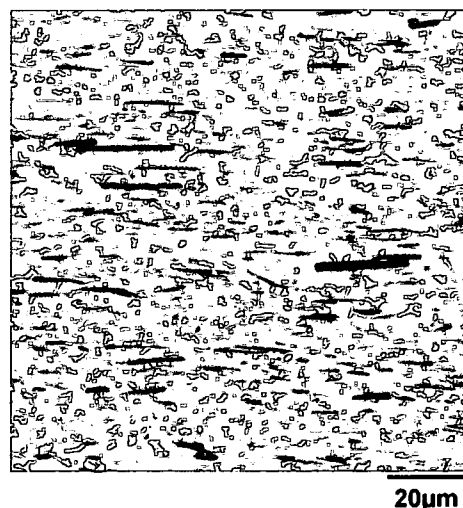


Figure 8 SEM image of micrometer-scale TiB (dark) w/in Ti-6Al-4V matrix.

however nano-TiB remain randomly dispersed throughout the matrix even after the material is subjected to extrusion.

The ability to form titanium-boron product via forging and casting approaches has been investigated [51,52]. In general, casting produces a fine TiB morphology with higher aspect ratio than typically achieved via P/M and subsequent forging. Figure 7 and 9 illustrate the typical microstructures attained via the forging and casting approaches, respectively. The casting approach to Ti-B alloy processing is already being investigated as a cost-effective alternative to current wrought alloy in some U.S. Navy applications. Both TMPs have promise for the specific needs of commercial applications in the aerospace industry.

Another approach being studied for processing Ti-B materials is direct laser deposition or Laser Engineered Net-Shaping (LENS<sup>TM</sup>). A research group at The Ohio State University studied the response of Ti-6Al-4V-xB to direct laser deposition [53]. The goal of the research was to deposit the material to a particular dimensional size, study the microstructure and crystallographic orientations, and understand the thermal stability. The material was deposited from

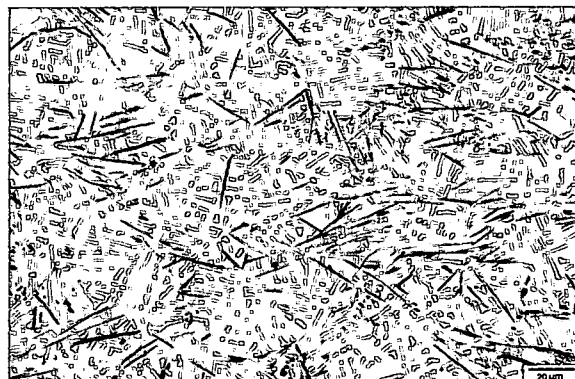


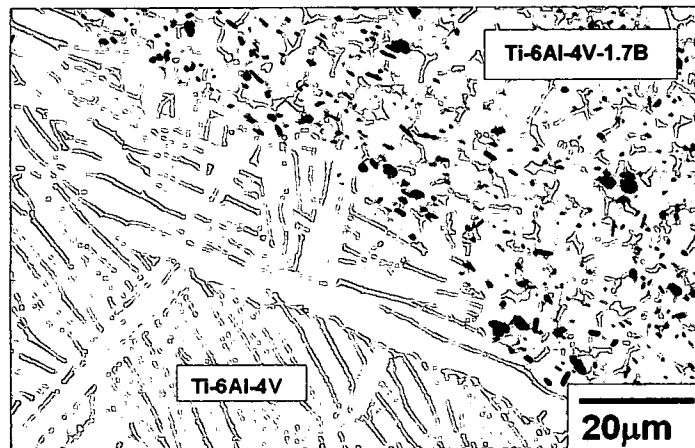
Figure 9 SEM micrograph of Ti-6Al-4V-1B as-cast microstructure. Note random TiB [68]

powder feedstocks consisting of a blend of PA Ti-6Al-4V and elemental boron. Utilizing SEM and TEM to characterize the microstructure, the group concluded that the LENS<sup>TM</sup> process produced a much more refined dispersion of TiB than capable of typical P/M processing. Post-heat treatments carried out after LENS<sup>TM</sup> deposition, suggested that LENS<sup>TM</sup> fabricated Ti-B materials were thermodynamically stable, exhibiting limited TiB coarsening.

Recently, from research on titanium-boron processing at AFRL at Wright-Patterson AFB, scientists realized that important enhancements can be provided by the addition of B to Ti or Ti alloys [54]. It is well known that a lamellar structure will ensue after thermally treating titanium above the  $\beta$ -transus and cooling back down. Below the  $\beta$ -transus, a more equiaxed structure exists. However, it has been found that titanium-boron alloys possess an equiaxed structure even after thermally treating above the  $\beta$ -transus. For example, it is known that the  $\beta$ -transus for the well known  $\alpha$ + $\beta$  alloy Ti-6Al-4V has a  $\beta$ -transus at  $995 \pm 10$  °C. Yet, inducing the composition Ti-6Al-4V-1.6B up to 1200 °C and bringing back to RT still retains an equiaxed- $\alpha$  matrix microstructure, as shown in Fig 10. Note the dramatic microstructural differences between the region on the right that has TiB (dark regions) randomly dispersed throughout the equiaxed- $\alpha$  matrix microstructure, while the region on the left, without TiB, has a lamellar structure. The Ti-6Al-4V and Ti-6Al-1.7B PM alloys in Fig. 10.



experienced exactly the same processing and post heat treatment conditions. A team at Ohio State University analyzed this phenomenon and concluded  $\alpha$ -particle nucleation occurred at TiB particles, along with pinning of grain growth caused by TiB [55]. This effect is



important for the fact that processing above

Figure 10 SEM image of the transverse section of P/M Ti-6Al-4V-1.7B powder extruded at 1100°C using wrought Ti-6Al-4V can.

the  $\beta$ -transus during typical Ti mill operations such as cogging is required to breakdown the microstructure. Essentially, the potential exists for alleviating the entire series of cogging operations simply by the addition of boron. Scientists from the Air Force at AFRL have applied for a United States patent on this specific topic [56].

### Ti-B Material System

Ti alloy development has progressed over the last few decades to where a wide range of alloys are available, [57] yet most of the Ti alloys cannot possess the higher levels of strength and stiffness combinations that are being sought after today, especially in the aerospace industry. The material response to applications has become more demanding, with

more rigid requirements of higher loads and/or system life expectancy, while industry designers have concentrated on pushing the envelope to reduce overall weight of the systems. The demand has stretched most light structural metals (i.e. Al, Mg, Ti) to their limit, therefore requiring other materials as replacements, or demanding enhancements to the metals. Much research and effort has been done in the particulate reinforced metals, metal matrix composites, and many have found their way primarily into niche-type applications.

However, a new class of Ti alloy has become even more promising over the 5-10 years, as researchers have found promising results in several key areas of Ti-B alloys. Strengths near that of commonly used high strength steels (i.e. 4130 and 4340) have been reached in higher B-containing alloys (generally above 1.5 wt% B), while maintaining tensile ductility around 3.5%. Alloys with lower B concentration have shown higher ductility, up to 13% elongation, with a slight drop in strength, up to 1200 MPa (ksi). A nearly linear relationship exists between the amount of B (vol%TiB) present and the Young's Modulus. Generally, it can be said that the main stiffness-controlling factor in the material is driven by the TiB volume percent.

The combination of high strength and stiffness, while having a density that is approximately half that of typical steels, makes Ti-B alloys very promising structurally efficient materials. Fig. 11 illustrates the specific

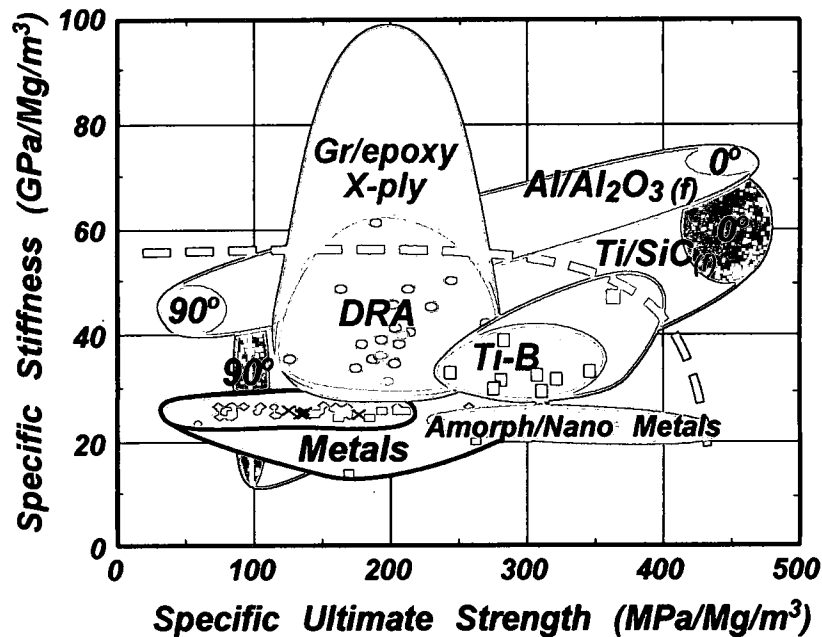


Figure 11 Structural Efficiency of Various Engineering Materials.[63]

properties of this class of alloys versus conventional and advanced engineering materials that are often utilized in aerospace applications. Ti-B alloys provide an overall system weight savings, and opportunity for reducing the size of the design envelope with reduction on cross-sectional area of a component.

The Ti-6Al-4V-xB material system can be separated into two classes of materials; alloys and composites. The Ti-B binary phase diagram (Fig.3) shows a eutectic reaction at approximately 2 wt% B. Careful study of the Ti-6Al-4V-xB system has shown that this eutectic reaction shifts to 1.55 +/- 0.05 wt% B [58]. The eutectic composition in Ti-B alloys provides a boundary between alloy-like and composite-like behavior. Hypoeutectic (B poor) compositions generally display a balance of strength, stiffness

and especially fracture properties (ductility, fracture toughness, etc.) that are broadly similar to conventional Ti alloys. Further, primary and secondary metallurgical working techniques identical to those used for conventional Ti alloys are effective for Ti-B alloys. On the other hand, hypereutectic alloy compositions (B rich) display a balance of mechanical properties that are clearly distinct from conventional Ti alloys. In particular, dramatic increases in stiffness and compressive strength are achieved at the expense of fracture properties, which drop below levels generally required for fracture-critical applications. The formation of large primary TiB particles via solidification generally restricts processing to solid state approaches more commonly used with MMCs. Thus, for the purpose of this work, the hypoeutectic composition studied is considered as a B-modified Ti alloy, while the hypereutectic composition is considered as a discontinuously reinforced MMC.

Therefore, with the advancement of these particulate-reinforced Ti alloys as potential replacements for applications that typically demand metals, there has been a growing need for better understanding of this relatively new class of material.

## The TiB Phase

### Crystal Structure and Properties

As mentioned, the addition of boron to Ti alloys provides dramatic increases in strength and stiffness, while maintaining microstructural stability. Boron is essentially insoluble in titanium, and the TiB phase precipitates *in situ* from the chemical reaction of  $\text{Ti} + \text{TiB}_2 \rightarrow 2\text{TiB}$ .

The TiB phase preferentially grows in the form of whiskers with a B27

orthorhombic crystal

structure [59]. Figure 12

depicts the crystal

structure of the TiB

phase with relative

indices. Due to the

anisotropic nature of the TiB crystal structure, the tendency of growth is

toward the [010] direction that leads to whisker morphology [60]. These

whiskers are chemically compatible with the titanium matrix, which further substantiates the phase as an ideal candidate for a reinforcement phase.

In addition, the density (4.56 g/cc) and coefficient of thermal expansion (CTE) ( $7.15 \times 10^{-6}/^\circ\text{C}$ ) [61] are comparable to titanium (4.5 g/cc and  $8.2 \times 10^{-6}/^\circ\text{C}$ , respectively) providing thermal stability and minimal residual stresses.

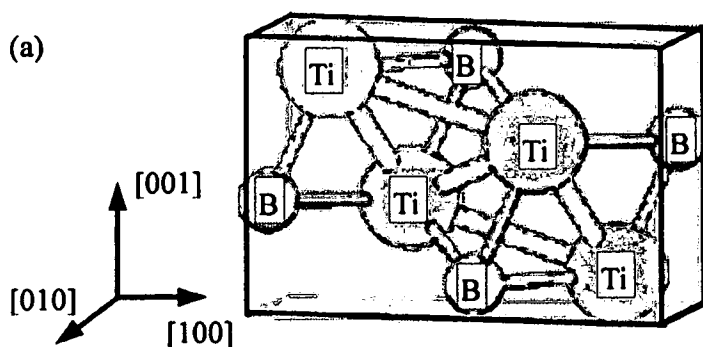


Figure 12 Crystal structure (B27) of TiB. [62]

There are several factors that accompany the selection of the candidate strengthening phases for particular application. For potential applications requiring increased strength, stiffness, and wear resistance with good matrix compatibility, the TiB phase ranks better than other reinforcements. Table 1 summarizes several important properties of some well-known hard particle phases (TiC, SiC, TiB<sub>2</sub>, B<sub>4</sub>C, Al<sub>2</sub>O<sub>3</sub>, TiN, Si<sub>3</sub>N<sub>4</sub>) that

Table 1 Property & attribute comparison of some typical hard particles[62]

Particle	Knoop Hardness (GPa)	Young's Modulus (GPa)	Coefficient of Linear Expansion*	Maximum Solubility [Matrix] [Particle] (at.%)
TiB	28.0	550	8.6	<0.001 1.0
TiC	24.7	460	7.4	1.2 15.0
TiN	24.0	250	9.3	22.0 26.0
SiC	25.0	420	4.3	Unstable in Ti alloy
Si <sub>3</sub> N <sub>4</sub>	14.7	320	3.2	Unstable in Ti alloy
TiB <sub>2</sub>	34.0	529	6.4	Unstable in Ti alloy
B <sub>4</sub> C	27.5	449	4.5	Unstable in Ti alloy
Al <sub>2</sub> O <sub>3</sub>	22.5	350	8.1	Unstable in Ti alloy

\* Coefficient of linear expansion of titanium alloy is around  $9 \times 10^{-6} \text{K}^{-1}$ .

have been considered in the past. TiB is the second hardest material on the list next to its diboride counterpart, and possesses the greatest individual stiffness. This table also indicates that the coefficient of linear expansion of TiB is very close to titanium, which, along with the very low solid solubility, provides a stable material system with minimal internal stresses. TiB is thermodynamically superior to other candidate reinforcing compounds, with outstanding physical and mechanical properties [62].

### *Size, Morphology and Distribution*

The formation of TiB whiskers is primarily via a eutectic reaction whereby micrometer size (2-5  $\mu\text{m}$  diameter) whiskers form with an aspect ratio on the order of 10. Figure 8 shows typical micrometer scale TiB present within an  $\alpha+\beta$  matrix of Ti-6Al-4V. The applicable phases present in the Ti-B alloys are depicted as: TiB (dark), alpha (gray), beta (white), and this means of identification is accurate for subsequent micrographs in this paper. In P/M alloys, it is possible to produce a small volume fraction of nanometer-size TiB whiskers with similar aspect ratio, which precipitate from the supersaturated solid solution during subsequent thermal

exposure. Figure 13 shows a representative microstructure to illustrate the presence of these nano-TiB within the titanium-boron alloy. Note the presence of a dislocation pileup in the TEM image located at one of the nano-

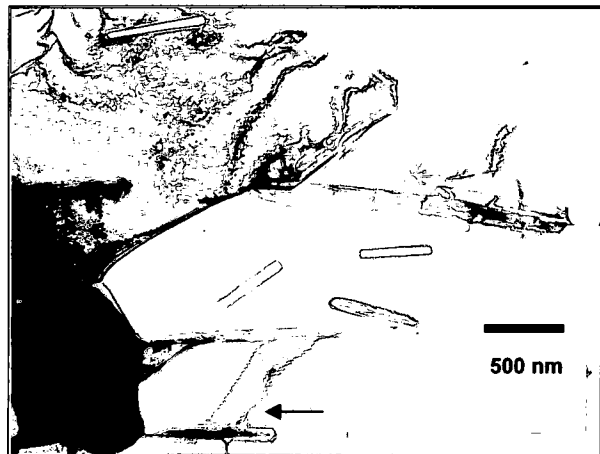


Figure 13 TEM image showing presence of nano-TiB. Note dislocation pileup at TiB indicated by arrow. [68]

TiB. These nano TiB whiskers have the potential to enhance the material strength via Orowan mechanism [63] which will be discussed in more detail in the strength modeling section of chapter II. There also exists a third length-scale TiB phase in hypereutectic compositions. These primary

TiB are on the order of 100-300 microns in length, Fig 14. The existence of primary TiB even at very low volume fraction becomes a major limiting factor for ductility of these materials. However, elimination of these large borides have become reality due to a better understanding and advancements in the Ti-B system and processing

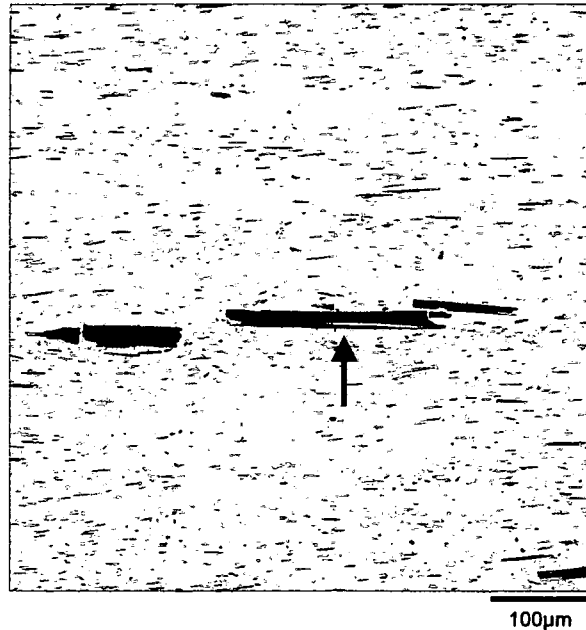


Figure 14 SEM image of primary TiB indicated by the arrow.

improvements, which will be discussed in chapter II. Table 2 summarizes the tri-modal TiB attributes for a composition in the hypereutectic regime, Ti-6Al-4V-1.7B produced via P/M.

Table 2 Summary of size-scale and related attributes of TiB phase in P/M Ti-6Al-4V-1.7B.

Size Scale	Aspect Ratio	Length	Vol%
Primary	5:1	100-300 µm	0.5
Micrometer	10:1	1-20 µm	8
Nanometer	10:1	0.1-0.5 µm	2



Both nanometer and micrometer TiB will uniformly disperse within  $\alpha$ ,  $\beta$ , or  $\alpha+\beta$  titanium matrix. Subsequent hot extrusion will preferentially align the micro-TiB, while the nano-TiB remain randomly dispersed throughout the

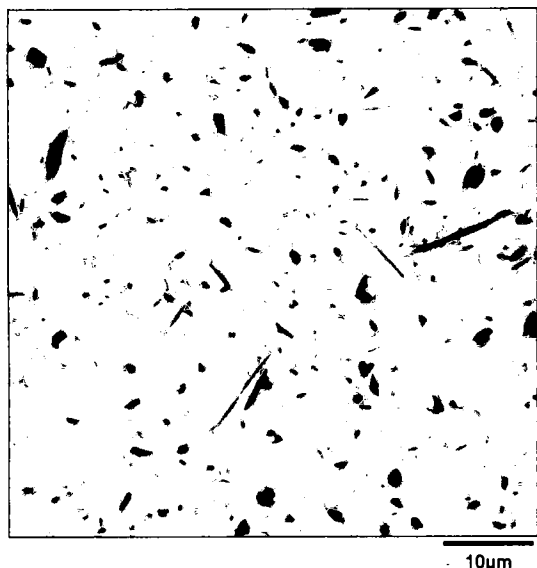


Figure 15 SEM image illustrating typical randomly dispersed TiB within Ti-6Al-4V matrix for as-compacted conditions.

matrix even after the extrusion.

Figure 8 is a representative image of TiB aligned along the extrusion direction (horizontal) while Figure 15 shows a typical microstructure of a P/M hot compacted composition with randomly dispersed TiB (10 vol% in this case) within the equiaxed- $\alpha$  matrix.

### OBJECTIVE AND APPROACH

#### Heat Treatment Study of Ti-6Al-4V-1.0B and Ti-6Al-4V-1.7B

From the preceding discussions, B additions provide the opportunity for important improvements in the processing and properties of Ti alloys. Although the alloy microstructural constituents are the same as for conventional Ti alloys, the TiB phase provides dramatic grain refinement, and stabilizes the alpha and beta phases significantly relative to Ti alloys without TiB. It is important to understand the relationship between the

material microstructure as it responds to thermal exposure, and how it relates to the bulk mechanical properties of the alloy. It is fundamentally known the microstructure of any metal directly relates to the overall bulk properties of the material. It is well known a finer-grained equiaxed microstructure will produce optimum strength properties, while a coarser lamellar-type structure will provide better toughness and FCPR properties (see titanium alloy categories section). Thus, it is pertinent to understand how the material system will respond to thermal conditioning, and the corresponding relationship between the Ti-B alloy microstructure and particular mechanical properties. In the present research, this is done via a post heat treatment study of the selected Ti-B alloys, Ti-6Al-4V-1.0B and Ti-6Al-4V-1.7B.

#### Thermal Stability of TiB Phase

As microstructural modification through heat treatment is a primary approach for controlling the properties of Ti alloys, it is vital to establish the influence of B additions on the microstructural response to various thermal treatments. Further, the evolution of the size and morphology of the TiB phase is likely to be important in the properties of the Ti-B alloys. The improved strength and stiffness of these Ti-B alloys are a function of the volume fraction, size and orientation of the TiB needles. Hence, it is important to establish the stability of these needles under thermal

exposure. The only known significant thermal stability study of TiB phase to date is that of T. Saito et al [64], who investigated the thermal stability of the TiB phase in beta-titanium, and qualitatively described the particle size increasing only slightly. The study also compared the coarsening rate of the TiB to TiC particulates, and it was concluded that TiB is much more thermally stable than that of TiC. In a limited study, Philliber also concluded the TiB phase to be thermally stable, and recommended the phase as usable for most alloys [65]. As these studies provided insight into the thermal stability of the TiB phase, a more systematic approach needs to be conducted. Specifically addressing the coarsening behavior of the reinforcement phase, and its effect on the overall material system is quite vital. A focus on the thermal stability or coarsening kinetics of the TiB particulate phase has been completed here, and quantifying the thermal stability of the TiB phase will provide useful kinetics information for dynamic property relationship of these particular alloys, and the potential for predictive coarsening tools for alloy use.

The goal of this research was two-fold, i) to analyze and quantify the thermal stability of the *in situ* TiB phase present in a pre-selected Ti-6Al-4V-1.7B alloy, ii) to study the microstructural-mechanical property response of Ti-6Al-4V-1B and Ti-6Al-4V-1.7B via exposure to pre-determined heat treatments and compare to conventional Ti-6Al-4V.

## SIGNIFICANCE OF RESEARCH

By understanding how B additions modify the microstructural response to heat treatments, a clear foundation for controlling the properties of Ti-B alloys via thermal treatment is established. This understanding provides guidance for achieving desired engineering properties.

## CHAPTER II

### EFFECT OF HEAT TREATMENT ON MICROSTRUCTURE AND PROPERTIES OF Ti-6Al-4V-XB ALLOYS

#### SUMMARY

The Ti-B alloys considered in this study had the nominal compositions in weight percent of Ti-6Al-4V-1.7B and Ti-6Al-4V-1.0B, respectively. The study conducted on these alloys evaluated microstructural/property response after subjecting to predetermined heat treatments. Each alloy powder was consolidated via blind-die compaction then subsequent hot extrusion, which established one baseline for comparison, or as-extruded (AE) condition. The wrought RMI Ti-6Al-4V material was also heat treated, and became the primary baseline for comparison in this study. The outer layer of Ti-6Al-4V canister material will also be briefly alluded to for microstructural comparison purposes. The study involved post heat-treating the baseline materials at predetermined parameters above and below the  $\beta$ -transus, which produced a variety of microstructures. Microstructural analysis was performed on the baseline and post heat-

treated specimens, and mechanical testing was conducted. Strength and stiffness modeling was also completed in order to ascertain the individual component contributions to the overall alloy bulk properties. It will be clear from this study that the two alloys respond somewhat similarly microstructurally to the heat treatment conditioning, yet produce different property results. These results and other details pertaining to the heat treatment study will be discussed in this chapter.

### Experimental

#### Program Materials

The Ti-6Al-4V-xB alloy powders used in this study were produced via inert gas-atomization at Crucible Research Corporation, Pittsburgh, PA. The two alloys will henceforth be referred to as 1.0B alloy and 1.7B alloy. The complete chemical compositions of these powders in actual wt% per the combination of atomic absorption spectrometry, plasma emission spectrometry, and interstitial gas analysis are given in Table 3.

Table 3 Chemical composition (in wt%) of pre-alloyed (PA) powder used in this study.

Composition	Al	V	B	O	C	N	Fe	Ti
Ti-6Al-4V-1.7B	6.17	3.99	1.61	0.182	0.148	0.016	0.064	Bal.
Ti-6Al-4V-1.0B	6.30	4.03	0.99	0.104	0.087	0.009	0.040	Bal.

The powder size distribution plots are shown in Fig. 16, which indicate a mean particle diameter of 40  $\mu\text{m}$  for the alloy containing 1.7B and around 240  $\mu\text{m}$  for the 1.0B alloy. Secondary electron micrographs shown in Figs. 17a and b reveal the relative morphology and size of the powders for both B-containing alloys prior to consolidation. Figs. 17c and d illustrate the existence of the TiB whiskers (dark particles) within each rapidly solidified powder particle for both alloys, and typical microstructures of individual powder particle cross-sections used in the studies.

#### *Thermo-mechanical processed material*

Fig. 18 illustrates the processing steps used to produce the final extruded product. PA powder of approximately 1 kg (2.2 lbs.) was transferred into a 6.35mm (0.25 in) thick wrought Ti-6Al-4V canister with dimensions 15.2cm (6 in) length x 7.6cm (3 in) diameter, degassed at 300°C for 24 hours and sealed via crimp and weld under vacuum. The sealed can was subjected to 1400 MPa pressure for 3 minutes in an extrusion chamber using a blind-die. Fig. 19 shows a photograph of compacted Ti-6Al-4V canister prior to subsequent extrusion. After soaking the billet for 1h at 1100°C the compacted canister was extruded using a ram speed of 6mm/s and an extrusion ratio of 15:1, utilizing a round-to-round conical die:

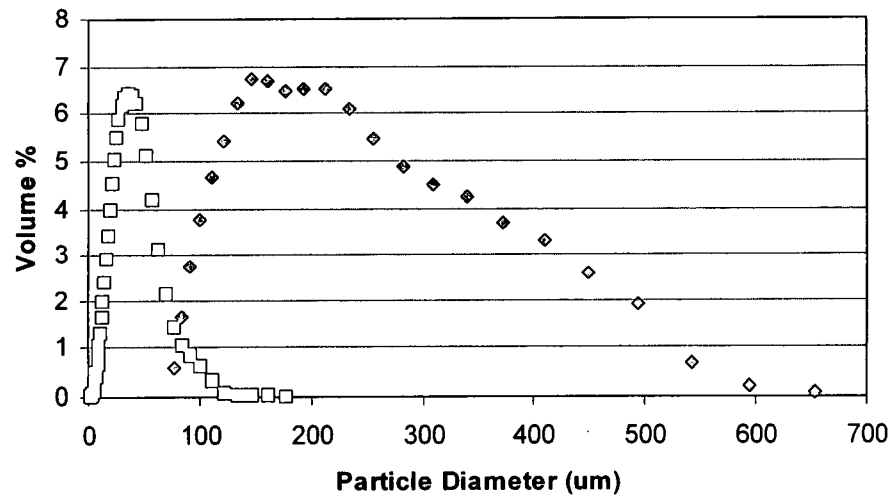


Figure 16 Powder size distribution plots of as-received pre-alloyed (PA) powder, Ti-6Al-4V-1.0B and Ti-6Al-4V-1.7B alloys.

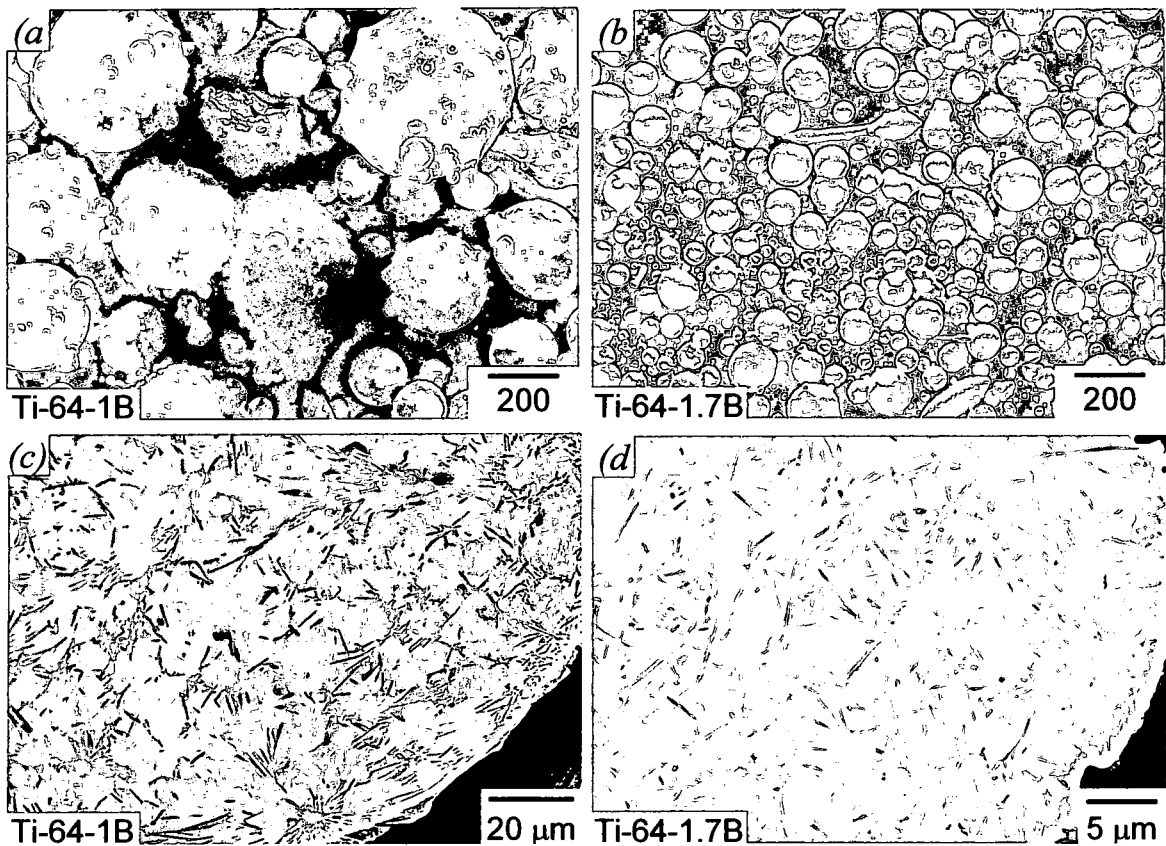


Fig. 17 (a, b) Morphology (secondary electron images) and (c, d) powder particle cross-section microstructure (backscattered electron images) of pre-alloyed powders used in this study: (a, c) Ti-64-1B and (b, d) Ti-64-1.7B.



The photograph of a typical final extrusion of approximate geometry of 1.5 meter x 2cm diameter is shown in Fig. 20. The extruded product in the as-extruded (AE) condition, is the baseline for comparison in the heat treatment study. The

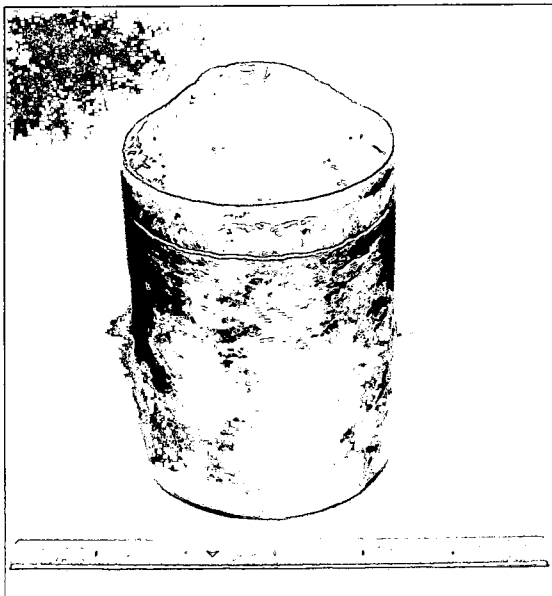


Figure 19 Photograph of Ti-6Al-4V canister after blind-die compaction of Ti-6Al-4V-1.0B pre-alloyed powder prior to extrusion.

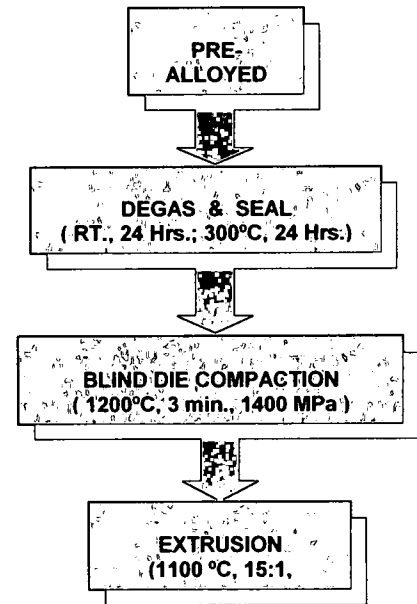


Figure 18 Processing flow diagram of material used in study.

approximately 1.5 meter  
extrusions were cut into 15 cm  
rod sections to be further  
subjected to heat treatment  
conditioning. The wrought RMI  
Ti-6Al-4V supplied in mill anneal  
condition, which will be used for

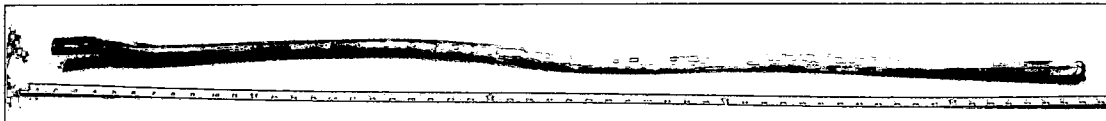


Figure 20 Photograph of a typical extruded Ti-B alloy used in this study.  
comparison, experienced only heat treatment conditioning.

## Heat Treatments

All heat treatments were performed in air using an induction furnace.

Standard heat treatments used for Ti-6Al-4V were chosen, as well as, non-standard Ti-6Al-4V heat treatments. These heat treatments were chosen in order to attain a variety of final microstructures for a direct comparison

Table 4 Heat conditions used in PM Ti-6Al-4V-1.7B and Ti-6Al-4V-1B experiment.

I.D. No.	HT Name	HT Condition
0	No HT	as-extruded
1	Duplex Anneal	940C/10min/AC/675C/4h/AC
2	Beta Anneal	1035 C/30min/AC/730C/2h/AC
3	Mill Anneal	735C/2h/AC
4	ST, Q&A	940C/10min/WQ/525C/4h/AC
5	High Beta Anneal 1100	1100C/30min/AC/730C/2 h/AC
6	High Beta Anneal 1200	1200C/30min/AC/730C/2h/AC

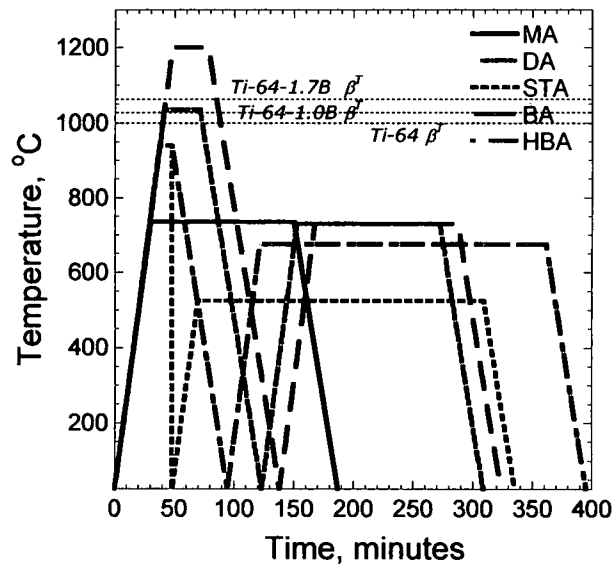


Fig 21 Various heat treatment schedules performed on Ti-6Al-4V-xB alloys in this study with relative  $\beta$ -transus temperatures.

to Ti-6Al-4V microstructures and properties at these particular conditions.

Table 4 summarizes the heat treatments and parameters used in this study

with typical industry nomenclature. The schematic shown in Figure 21 illustrates the time-temperature relationship of the heat treatments, with reference to the  $\beta$ -transus temperature. Heat treatments identified 1 through 4 are typical for Ti-6Al-4V alloy, and are often used in commercial applications [3]. The non-standard heat treatment conditions, numbered 5 and 6, were chosen based on factors including knowledge of the beta transus at approximately  $1050 \pm 20^\circ\text{C}$  for the 1.7B alloy [54], and  $1025 \pm 20^\circ\text{C}$  for the 1.0B alloy [66]. These two non-standard treatments were selected to explore conditioning above the  $\beta$ -transus at 1100 and 1200  $^\circ\text{C}$ , respectively.

## Metallography

Material was extracted from the heat treated rods and grip section of the tensile specimens in order to perform metallography and subsequent microstructural analysis using scanning electron microscopy (SEM). Sections from both the transverse and longitudinal extrusion directions were mounted in conductive material. Sections were also extracted from the wrought Ti-6Al-4V mill material and mounted in like manner. The B-containing alloys, as well as, the Ti-6Al-4V RMI wrought material were represented for each heat treat condition. Subsequent SEM observations using backscatter electron image (BEI) mode, with an accelerating voltage of 15kV and a probe current of 400pA, were

performed on the mounted specimens. Typical microstructural features were quantified for each post-heat treatment condition.

## Mechanical Testing

Round  $\frac{1}{4}$ -20 threaded mechanical tensile test specimens, Fig. 22, were machined from the as-extruded



Figure 22 Representative  $\frac{1}{4}$ "-20 round dumb-bell tensile specimen used for testing. Specimens were extracted along the length of the extrusions.

and heat-treated 15cm rods. The gage section surface was finished to an RMS surface finish of  $16\text{ }\mu\text{m}$  using a low stress grind operation. Three tensile specimens at each heat treatment condition were extracted from the center portion of the extrusion rods in the longitudinal (extrusion) direction. The tensile tests were performed following ASTM E 8M at room temperature using an MTS 810 servo-hydraulic tensile test machine at a cross-head speed of  $10^{-2}\text{ mm/s}$ , which corresponds to an initial strain rate of  $10^{-3}/\text{s}$ . Displacement was measured using a 10mm clip extensometer. Mechanical test results from the B-containing alloys were compared to Ti-6Al-4V values reported in ASM Handbook, and compared microstructurally to the wrought Ti-6Al-4V heat treated material.

## Fractography

Fracture surfaces of the post-tensile tested specimens were comprehensively examined using SEM to determine the predominant fracture mode and initiation site(s), and microscopic mechanisms governing tensile fracture. Additional samples for SEM observation were obtained from the deformed post-test specimens by sectioning perpendicular to the fracture surface near the fracture (parallel to the extrusion direction) as to expose the profile of the fracture surface, as well as, the deformed microstructure near the fracture. The microstructures near the fracture surface, as well as, in the grip section (non-deformed) of the tensile specimen were both analyzed for any significant differences that may be related to, or provide an indication of the failure mode(s) or mechanism(s).

## Results and Discussion

### Starting Microstructure

Examination of the extruded product revealed the material to have an outer thickness of approximately 3mm composed of Ti-6Al-4V alloy (canister material), while the inner majority cross-section contained the particular Ti-B alloy. A representative cross-section prior to heat treatment (i.e. in the AE condition) is illustrated in Fig. 23, with the Ti-6Al-4V alloy on

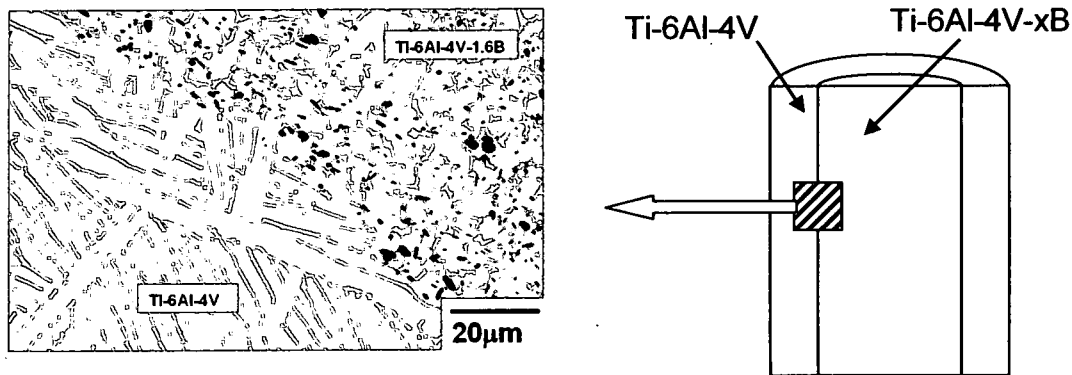


Figure 23 SEM micrograph of transverse section of wrought Ti-6Al-4V canister and PA P/M Ti-6Al-4V-1.7B post extrusion at 1100°C, demonstrating the obvious difference in microstructures.

the left and 1.7B alloy on the right. Note the dramatic microstructural differences between the region on the right that has TiB (dark particles) uniformly dispersed throughout the equiaxed- $\alpha$  matrix microstructure, while the region on the left, without TiB, has a fully lamellar colony structure. The Ti-6Al-4V canister and Ti-6Al-4V-1.7B materials in Fig. 23 experienced exactly the same TMP conditions. It is well known that a lamellar-type structure will result after thermally treating  $\alpha+\beta$  titanium above the  $\beta$ -transus and slow cooling to room temperature. Previous studies have shown that TMP of Ti-6Al-4V above the  $\beta$ -transus temperature leads to a 'lamellar' microstructural morphology, consisting of  $\alpha$  platelets with an inter-platelet  $\beta$  phase [67].

However, it has been found that Ti-B alloys can possess an equiaxed structure even after thermally treating above the  $\beta$ -transus. The  $\beta$ -transus for the classical  $\alpha+\beta$  alloy Ti-6Al-4V is reported to be  $995\pm 10^\circ\text{C}$  [3]. The

1.0B and 1.7B alloys retain an equiaxed- $\alpha$  matrix microstructure even after compacting at 1200C, followed by extruding at 1100 °C, as shown in Fig. 24. The cause of the equiaxed structure in the Ti-B alloys has been attributed primarily to two mechanisms, i) pinning of the grains by the TiB

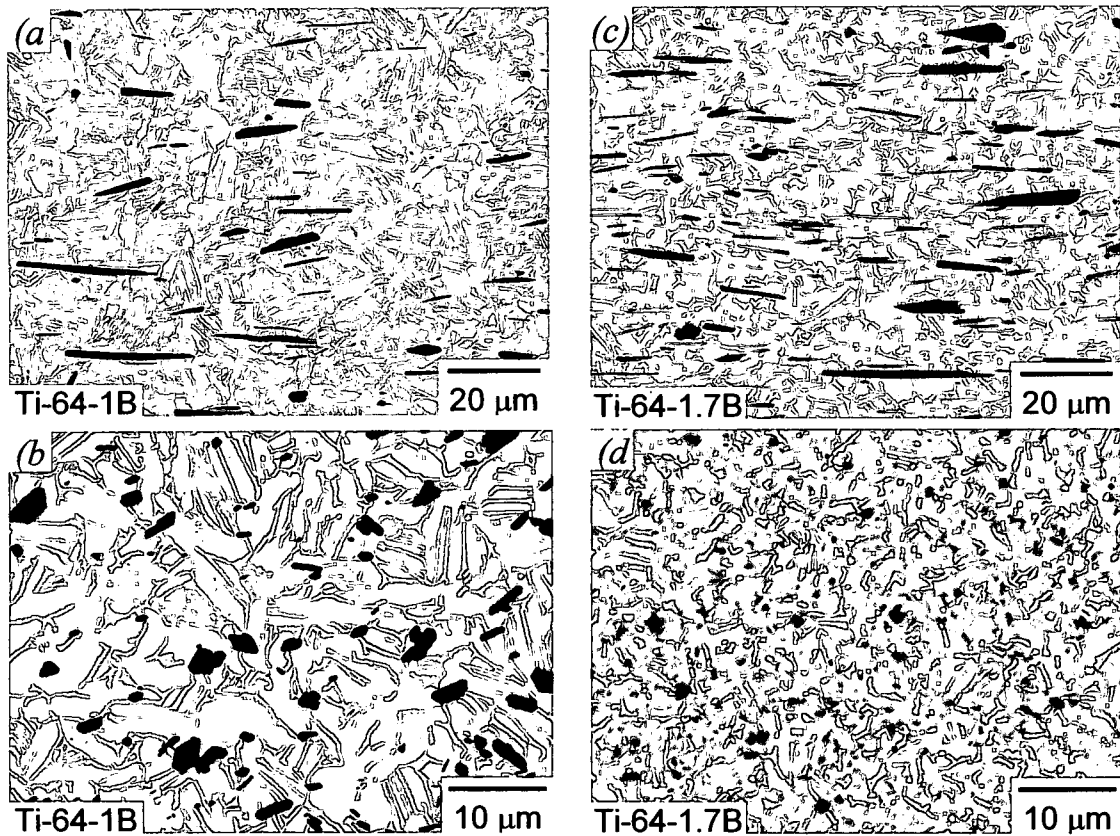


Fig. 24 Backscattered electron images of extruded (a, b) Ti-64-1B and (c, d) Ti-64-1.7B in the (a, c) longitudinal (extrusion direction is horizontal) and (b, d) transverse direction. These are the microstructures of the starting materials that were subjected to various heat treatment schedules in this study.

phase particles [68], and ii) TiB phase acting as nucleation sites for alpha phase during beta to alpha transformation. Banerjee *et al* analyzed this phenomenon and concluded  $\alpha$ -particle nucleation occurs at TiB particles,

along with pinning of grain growth caused by TiB [53,2]. Further details on this phenomenon are illustrated in the referenced papers.

This nucleation, growth and sustainment of equiaxed grains has important implications. One such implication, mentioned in the introduction chapter, involves alleviating time-consuming processing steps at the mill operation. During titanium alloy production, a series of processing steps known as mechanical cogging is used to essentially breakdown or refine the grain structure via thermo-mechanical work. This typical mill processing step can potentially be alleviated via pre-imposed grain refinement with the addition of B, saving industry time and money at the mill production site [69].

The as-extruded microstructures for both Ti-B alloys, Ti-6Al-4V-1.0B and Ti-6Al-4V-1.7B, are shown in Figs. 24 (a-d), respectively. The phases are depicted as: TiB (dark),  $\alpha$  (gray),  $\beta$  (white), and this means of identification is accurate for subsequent micrographs. Figure 24a,c depict the as-extruded microstructure for 1.0B and 1.7B, respectively, while Figs. 24b,d show the same in the transverse direction. The 1.7B alloy had an equiaxed- $\alpha$  microstructure having a grain size on the order of 2-5  $\mu\text{m}$ , with grain boundaries decorated with  $\beta$  phase. The 1.0B alloy, with slightly coarser grains, 5-10  $\mu\text{m}$ , had a somewhat bimodal structure of intermixed globular  $\alpha$  and colonized lamellar  $\alpha$  decorated with  $\beta$  phase. The larger average grain size for the 1.0B alloy can be



attributed to the coarser starting powder particle size used for the 1.0B versus the 1.7B alloy (see Fig 16 powder particle distribution). The as-received wrought mill Ti-

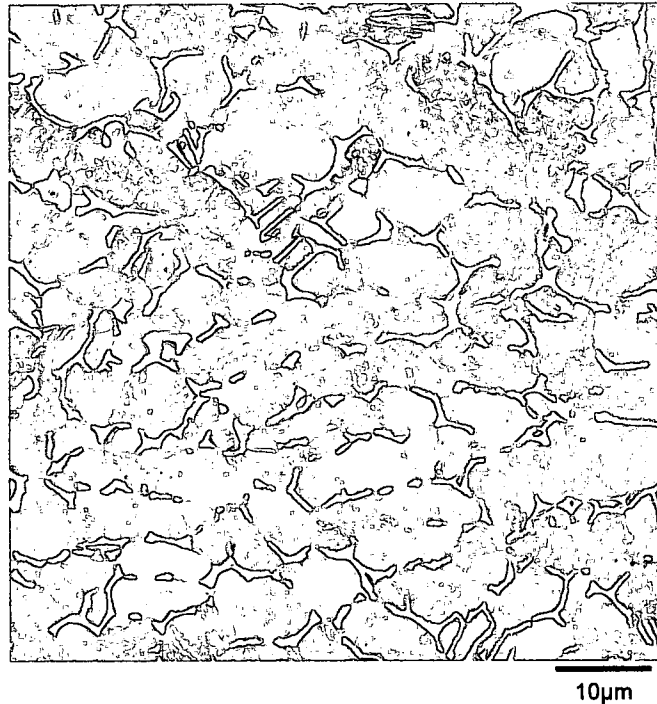


Figure 25 Ti-6Al-4V wrought as-received mill material.

6Al-4V material, as shown in Fig.25, used for comparison, had an initial globularized alpha microstructure of average grain size ranging 10-15 µm with beta phase at the grain boundaries.

The TiB phase, which developed *in-situ* in the form of randomly distributed needles or rods (evident in the as-compacted microstructure shown in Fig 15), primarily had a mean length around 10-20 micron and aspect ratio around 10, and were subsequently aligned parallel to the extrusion direction during the extrusion process. The 1.7B alloy, with 10vol% TiB, demonstrated a tri-modal size effect for the TiB phase (see Fig. 26). The highest volume percent of approximately 8% was on the order of 10-20 micron in length, termed micro-TiB, while approximately 1-2% was sub-

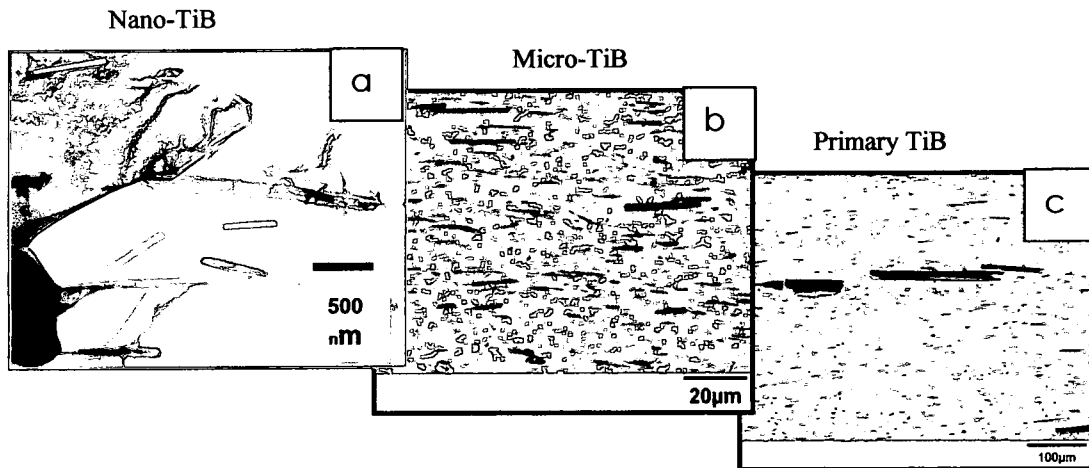


Figure 26 Representative starting (pre-HT) Ti-6Al-4V-1.7B microstructure, illustrating the tri-modal TiB size scale presence. micron (or nano-TiB) size of less than 500 nm. A relatively small percentage (<0.5%) of primary TiB was also present for the 1.7B alloy, which influenced mechanical properties dramatically, and will be discussed in more detail later in this paper. The sub-micron scale TiB particles had similar mean aspect ratio as the micron size TiB, yet remained predominantly randomly dispersed rather than aligned after extrusion as shown in Fig 27c. Figs 27a and b illustrate the alignment of the TiB phase as a result of the extrusion process, and Fig27c shows a closeup of the transverse direction, which depicts the non-alignment of the nano-TiB. This phenomenon could possibly be attributed to the smaller surface area of the sub-micron TiB relative to the alpha grain size. The size, aspect ratio and uniform distribution of TiB was very similar for the Ti-6Al-4V-1.0B alloy, however, with a uni-modal presence of micron TiB only. Perhaps related to the wt% B in the alloy, and influenced thermodynamically by

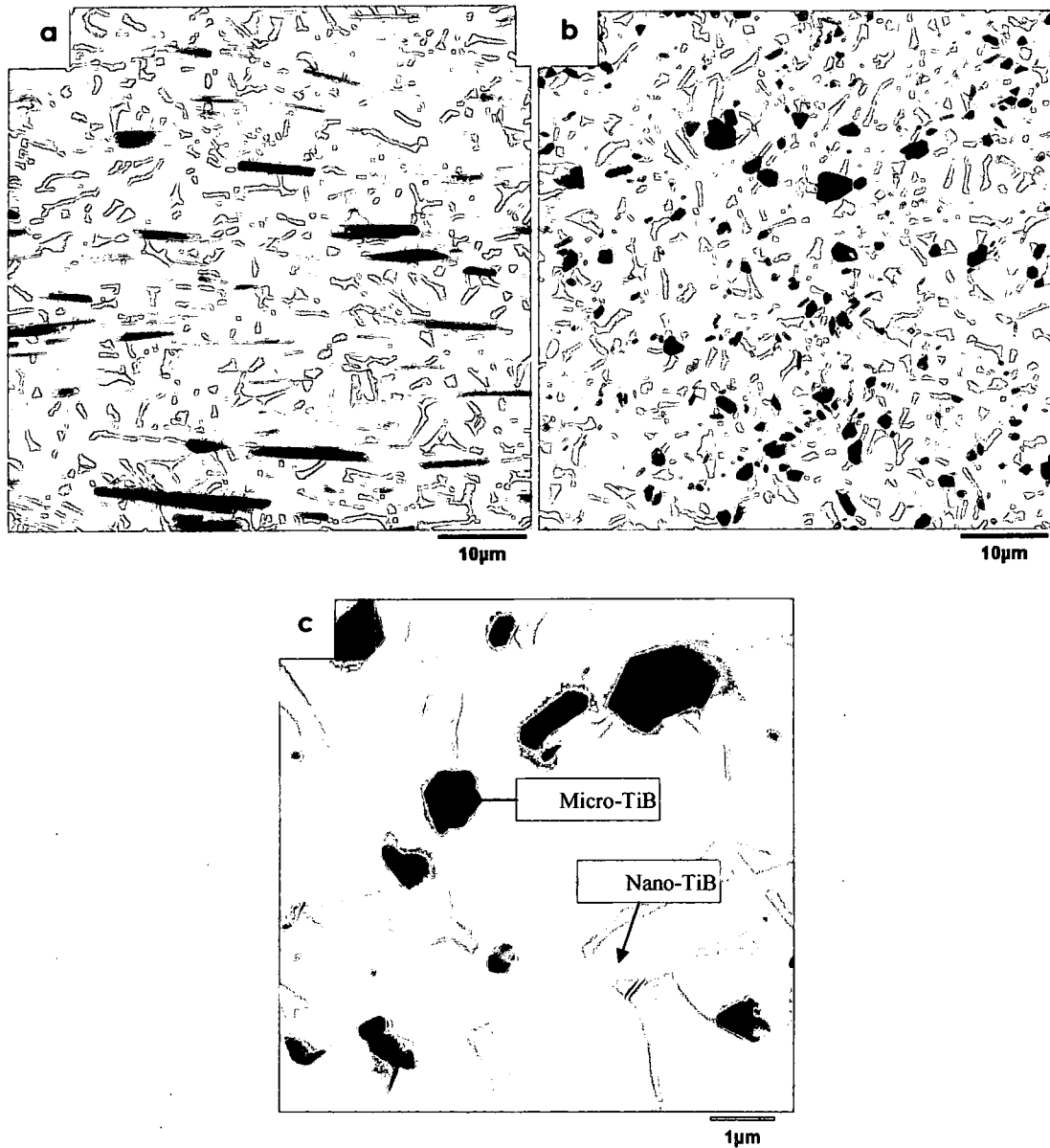


Figure 27 Ti64-1.7B alloy (a) longitudinal (b) transverse, illustrating alignment of micro-TiB from extrusion, and (c) closeup of transverse section, illustrating randomly distributed nano-TiB after extrusion.

the difference in alloy starting powder particle size (see Fig.16), the B is not trapped during powder rapid solidification in the 1.0B alloy and precipitated during further thermal exposure, as has been noticed in the 1.7B alloy, and will be discussed in more detail in chapter III.

## Microstructures post-Heat Treatment

The heat treatment conditioning produced a variety of microstructures leading to microstructural differences between the two alloys, and especially evident between the Ti-B alloys as compared to the Ti-6Al-4V wrought mill and Ti-6Al-4V wrought canister material (see Fig.10). As noted previously, the as-extruded (AE) microstructure illustrated the differences in the Ti-6Al-4V and Ti-6Al-4V-xB alloys (see Fig 10) where the Ti-B alloys had an equiaxed- $\alpha$  type microstructure, while the Ti-6Al-4V canister composition evolved the expected lamellar-type morphology since the material was subjected to temperatures above the  $\beta$ -transus for typical Ti-6Al-4V (995 $\pm$  20C) [3].

The 1/4 inch thick discs were individually heat treated according to the parameters detailed in Table 4. Again, standard heat treatments used for Ti-6Al-4V were used, as well as, non-standard heat treatments known to be above the  $\beta$ -transus for these particular alloys [54,66]. The terminology used to describe the individual heat treatments is also standard, except for the two heat treatment conditions of high beta anneal at 1100 °C (HBA1100) and high beta anneal 1200 °C (HBA1200). The array of SEM images in Figs.28 (a-o) show representative side-by-side microstructures of the wrought Ti-6Al-4V alloy, Ti-6Al-4V-1.0B and Ti-6Al-4V-

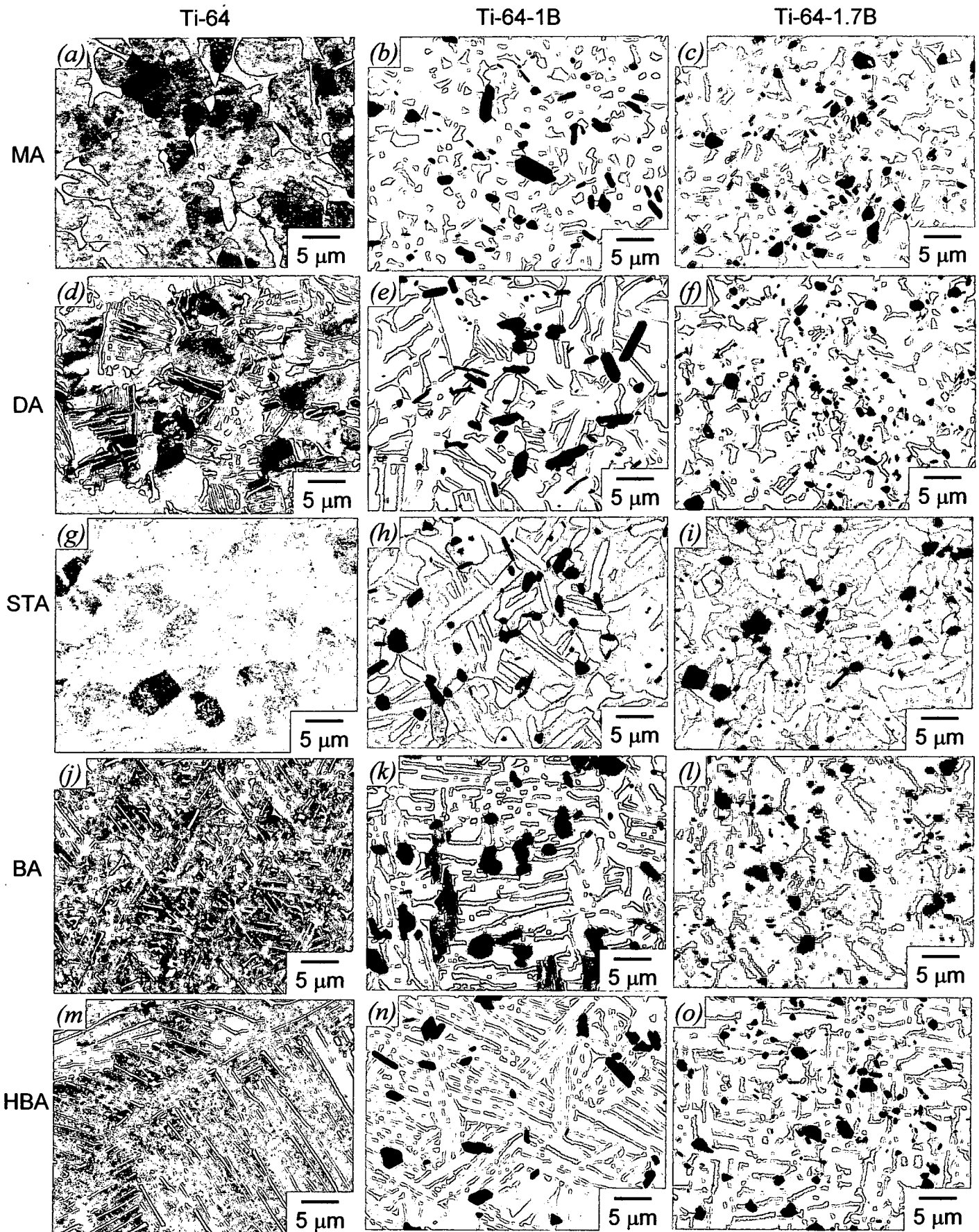


Fig. 28 Backscattered electron images of Ti-64, Ti-64-1B, and Ti-64-1.7B after various heat treatments..

1.7B P/M alloys, respectively, that have been exposed to heat treat conditions per Table 4. The selected heat treatment schedule resulted in a variety of  $\alpha+\beta$  matrix microstructures, while the intermixed TiB phase remained primarily stable in terms of size, morphology, distribution, and orientation. For consistency and purpose of this paper, the discussion of microstructural response and evolution will focus primarily on the  $\alpha+\beta$  matrix only.

Ti-6Al-4V is most commonly used in the fully annealed condition, often referred to as mill annealed (MA) [3], and is most often supplied by the respective titanium mill in this condition. The MA condition gives very good ductility with moderate strength. The wrought Ti-6Al-4V alloy in this paper was supplied directly from the mill factory (RMI industries, Niles, OH USA), and possessed a MA structure (see Fig. 28a). Further MA heat treatment processing coarsened the microstructure only slightly from an average grain size of 10 to 15  $\mu\text{m}$  (see Figs. 25, 28a) respectively. The Ti-B alloys shown in Figs 28b and c also show a typical equiaxed microstructure, but an order of magnitude smaller than the boron free alloy as shown in Fig. 28a. Again, microstructural evidence of alpha grain pinning attributed to the uniformly dispersed TiB phase.

Often a duplex structure allows for a good overall combination of properties. The duplex structure provides the strength via equiaxed  $\alpha$  grains, and optimal combination of toughness through the intermixed

colonized lenticular or lamellar structure. This type of structure is accomplished via duplex anneal (DA) heat treatment just below the beta transus, and most representative of a DA structure in Fig. 28d for the wrought Ti-6Al-4V alloy, and Fig 16k to a lesser degree. The Ti-B alloys that underwent DA conditioning demonstrate a more globular or equiaxed alpha microstructure (Figs. 28 e,f), with the 1.0B alloy having a slightly larger average grain size. The grain size coarsened only slightly beyond the original as-extruded condition to approximately 4-8 micron in range for the 1.7B alloy, and approximately 6-12 micron for the 1.0B alloy.

The solution treat and age (STA) condition exhibited similar  $\alpha+\beta$  microstructures for both B-containing alloys and the Ti-6Al-4V wrought material alike. Relying on the good hardenability characteristics of Ti-6Al-4V (up to a maximum material thickness of approximately 30mm), entrapment of a certain percentage of  $\alpha'$  martensitic structure, followed by aging to decompose the as-quenched beta phase [2] produced a typical globular primary alpha structure in an aged martensitic structure shown in Figs. 28(g-i) for these STA parameters. Note the Ti-B alloys (Figs. 28h,i) produced a lower percentage of prior  $\beta$  (or martensite) phase due primarily to quenching lower in the  $\alpha+\beta$  region, since the Ti-B alloys have higher  $\beta$  transus temperatures compared to Ti6Al-4V. The STA heat treatment condition is primarily used for highest strength conditions,

however, often the ductility will suffer due to the presence of a metastable martensitic structure.

High temperature application such as a jet engine turbine blade would see benefit in a microstructure such as Figs. 28(j,m-o) produced via BA and HBA, whereby creep resistance and damage tolerance properties (i.e. fracture toughness and FCPR) are maximized. This Widmanstätten and lamellar-type microstructures are often accomplished via heat treatment above the  $\beta$ -transus, followed by AC. Note the wrought Ti-6Al-4V alloy exhibited a typical Widmanstätten structure for a BA conditioning, Fig.28j, while the Ti-B alloys exhibited a more acicular and globular alpha structure for 1.0B and 1.7B, respectively. Since the BA heat treatment was accomplished at the standard 1035C temperature for Ti-6Al-4V, the beta transus was most likely not crossed for the 1.7B alloy and was borderline for the 1.0B alloy [54,66], allowing for a more acicular and globular structure, respectively. The HBA conditioning assured to be above the  $\beta$ -transus at 1200°C, giving rise to a resultant lamellar structure.

## Mechanical Properties



Figure 29 provides the tensile stress-strain curves at RT for both B-containing alloys as a function of heat treatment condition. Results of the

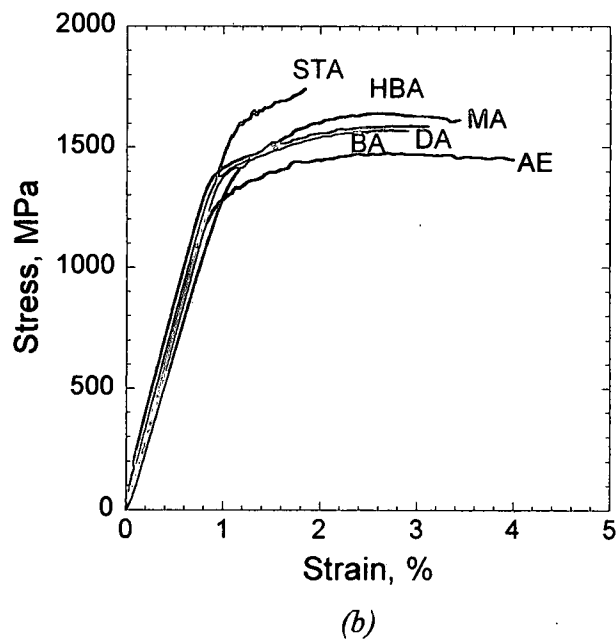
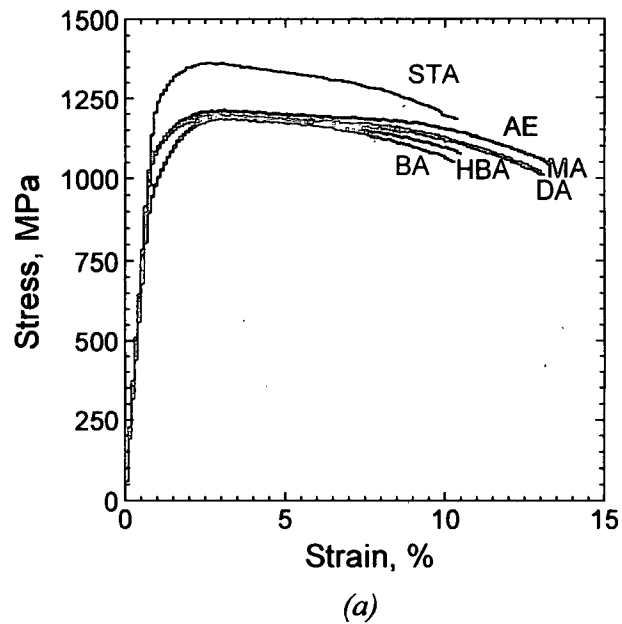


Fig. 29 Tensile stress-strain curves of (a) Ti-6Al-4V-1B and (b) Ti-6Al-4V-1.7B after various heat treatments.

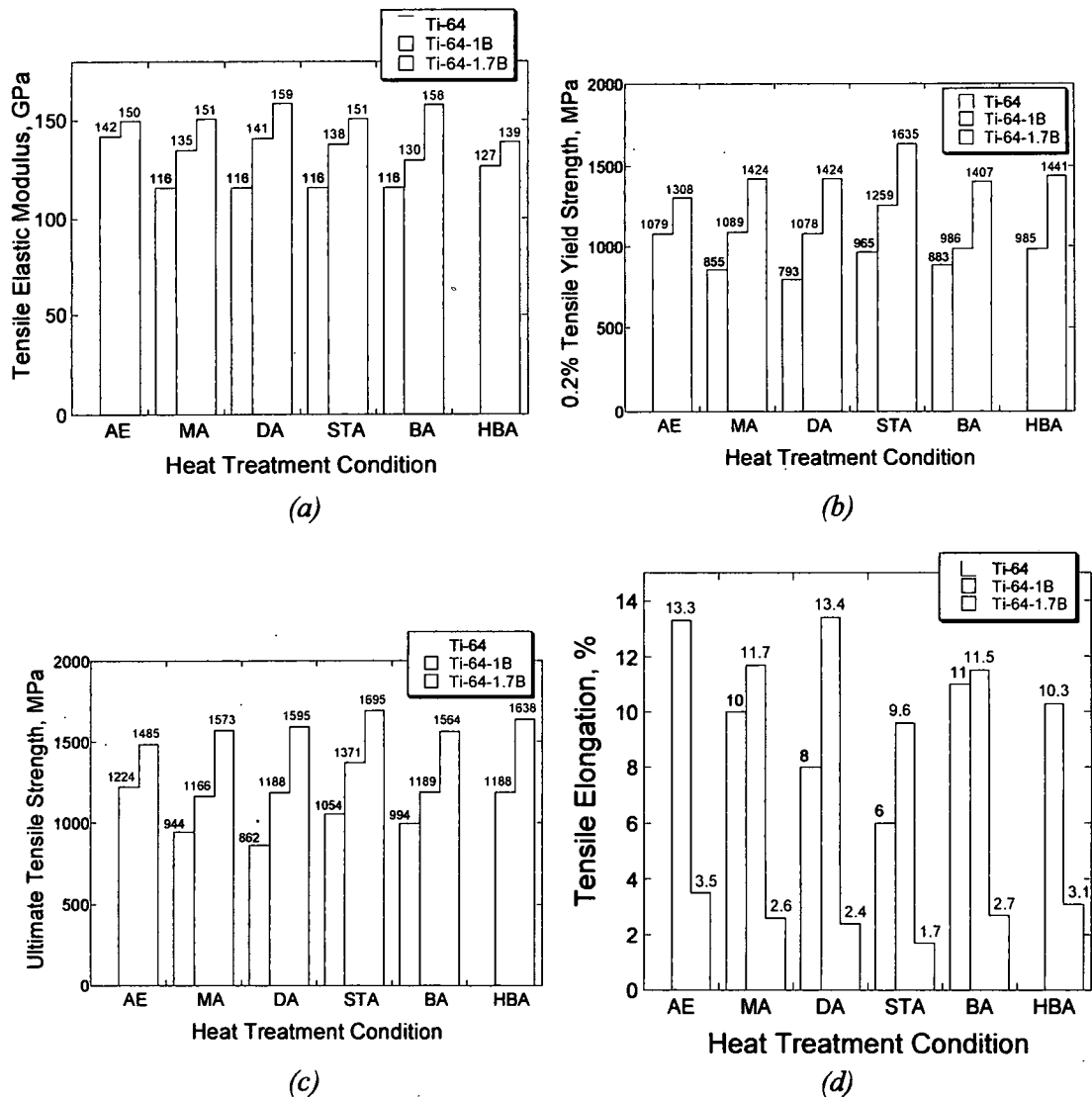


Fig. 30 Tensile properties of Ti-6Al-4V-1B and Ti-6Al-4V-1.7B after various heat treatments: (a) elastic modulus, (b) 0.2% yield strength, (c) ultimate tensile strength, and (d) elongation to failure. Data on Ti-6Al-4V taken from reference [ASM Hbk] are included for comparison.

testing showed the 1.7B alloy consistently produced the highest strength (up to 1695 MPa tensile) and stiffness (150 GPa) in each heat treatment condition, but the 1.0B alloy consistently demonstrated higher ductility for

all conditions. In the majority of aerospace applications that call for structural alloys, design engineers require a minimum specified ductility of 6% [70]. Figure 30 summarizes the tensile test results in chart form for both Ti-B alloys, and compares to standard Ti-6Al-4V textbook values at the same heat treatment conditions.

### *Elastic Modulus*

Confirmation that stiffness relied heavily on the amount of TiB present in the alloy was demonstrated by the higher stiffness values with increasing TiB vol%. Figure 30a shows the 1.7B alloy consistently resulted in higher stiffness values (139-159 GPa) than 1.0B alloy (127-142 GPa) as a function of heat treatment condition. The 1.0B alloy stiffness values were all higher than the reported 116 GPa of Ti-6Al-4V for all heat treatment conditions. Overall, as compared to Ti-6Al-4V, the 1.7B alloy showed 20-37% increase in stiffness, while the 1.0B alloy demonstrated a 10-27% increase. This coincides quite well with the near linear relationship that exists between stiffness and vol% TiB, and earlier reported results by others [66,71-73].

Heat treatment conditioning appeared to be only slightly influential in the stiffness of the Ti-B alloys, which is consistent with the suggestion that the TiB phase is the major controlling factor in the material stiffness. Both Ti-B alloys demonstrated lower stiffness values for the HBA condition, which

may be attributed to the fully lamellar morphology of the  $\alpha+\beta$  phases. The orientation of the TiB whiskers also played a key role in the total stiffness of the Ti-B alloys. The tensile specimens were tested in the longitudinal (as-extruded) direction, and the majority of the TiB whiskers were aligned along the load direction. Since the TiB morphology is in the form of whiskers of typical aspect ratio around 10, loading in the length direction would produce a higher modulus than perpendicular (transverse direction) to the TiB. Experimental data show that oriented fibers misaligned with the loading direction rapidly lose strengthening efficiency with increasing angle [74]. Miracle et al reaffirmed this physical relationship in reported results for alloys with 20-40 vol% TiB, whereby alloys tested in the longitudinal direction consistently resulted in higher modulus values than those tested in the transverse [71].

### *Strength and ductility*

The tensile stress-strain curves in Fig. 29 illustrate the ductile behavior of the 1.0B alloy versus the 1.7B alloy. McCallister et al terms a fracture strain of less than 5% as a brittle material [75], however, general material science acceptance of a brittle material is classified as having no plastic deformation. Both 1.0B and 1.7B alloys demonstrate plastic deformation in the mechanical testing performed. The strength values are clearly higher in the 1.7B alloy, with relatively good strength for the 1.0B alloy

when compared to Ti-6Al-4V. Even at the strength levels for the Ti-B alloys shown in Figs. 30b and c, the 1.0B alloy demonstrated very good ductility, as much as 13.4% in the duplex anneal (DA) condition, as shown in Fig. 30d. The ductility levels for both B-containing alloys and handbook Ti-6Al-4V for their respective heat treatment conditions are shown in Fig. 30d. Where the 1.7B alloy had limited ductility for all conditions (up to 3.5%), the 1.0B alloy consistently possessed very good ductility levels ranging from 9.6-13.4 total %elongation, for all heat treatment conditions, with the highest in the AE (13.3%) and DA (13.4%) conditions. Both of these conditions, AE and DA, had an equiaxed- $\alpha$  grain structure, which explains the higher ductility values. It is well known the STA condition for Ti-6Al-4V produces the highest strength and lowest ductility, but it is truly worthy of noting that the 1.0B alloy still achieved ductility of 9.6% for this condition.

In both alloys the STA condition produced the highest strength, with the 1.7B alloy reaching a tensile of 1695 MPa and 1371 MPa for the 1.0B alloy, respectively, which is a 60 and 30% increase over Ti-6Al-4V in the STA condition. Furthermore, these strengths are reaching those of high strength steels (i.e. 4140, 4340) at 60% of the weight. Within the heat treatment schedule, the 1.0B alloy demonstrated a range in strength of around 274 MPa, with the lowest yield strength condition HBA heat treatment at 985 MPa, which most likely can be attributed to the fully lamellar-type  $\alpha+\beta$  microstructure. The load direction was in the

longitudinal direction, or aligned with the TiB phase, producing optimal TiB orientation strengthening-effect conditions. Based on the results of the tensile tests for the Ti-B alloys it is clear that the amount of TiB phase present, plus the type of heat treatment conditioning induced on the material influence the overall strength properties of the alloys.

### Fractography

The post-tensile tested specimens were analyzed for both Ti-B alloys to acquire an understanding of the fracture mode. As mentioned, judging from the stress-strain curves (see Fig.29) for these alloys, the 1.7B alloy exhibited a less ductile-type fracture than the 1.0B alloy. However, the 1.7B alloy did indicate ductility as indicated by the yield stress and ultimate stress. The 1.0B and 1.7B alloy fracture surfaces (see Fig. 31a,b) were analyzed using a scanning electron microscope (SEM) in secondary mode. After analyzing the 1.7B alloy fracture surfaces, it was evident that all specimens shared a common fracture surface pattern. The lines or ridges emanating radially from a single location indicated the origin of fracture initiation, which will be explained in more detail. While this is true for the 1.7B alloy, the fracture surface for the 1.0B alloy specimens exhibited more ductile-type characteristics with no clear single initiation site (see Fig. 31b). An explanation for the difference in fracture modes could be determined and will be discussed further in detail.

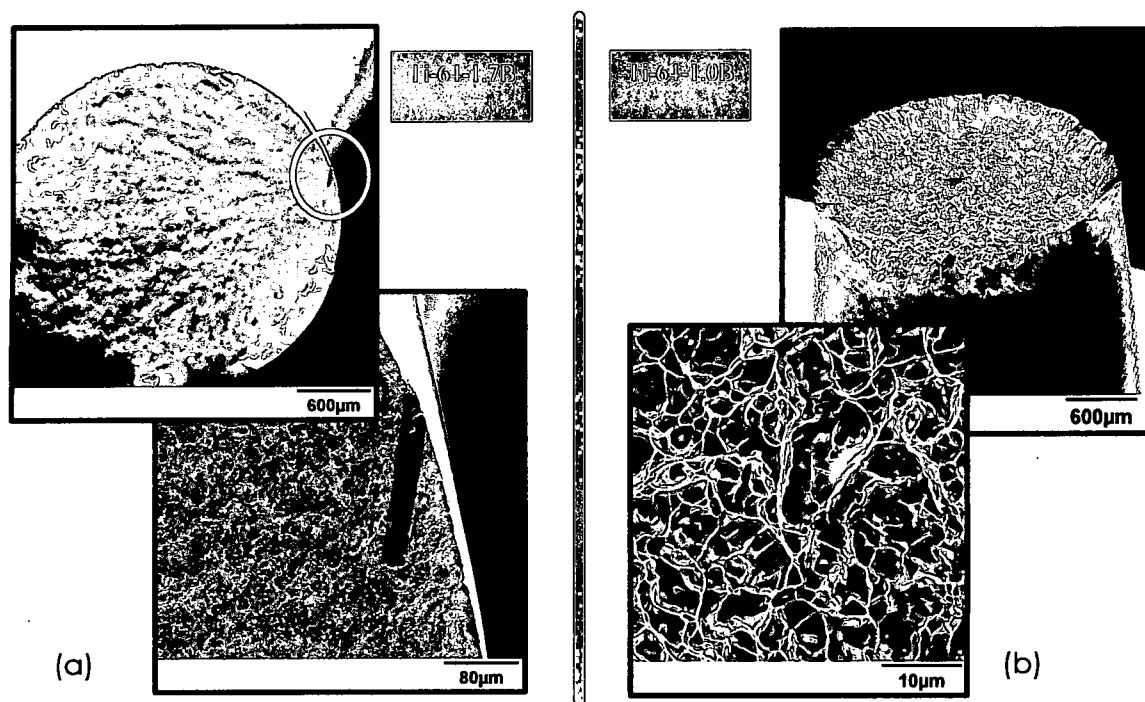


Figure 31 Fractographs of tensile specimens using SEM secondary mode revealing entire fracture surfaces and closeups of (a) Ti-6Al-4V-1.7, and (b) Ti-6Al-4V-1B alloys, respectively.

As previously reported, there exists a trimodal length scale for TiB in the 1.7B alloy. The relatively larger TiB (0.5 vol% presence), or "primary borides" are on the order of 100-300 microns in length (see Fig. 26). However, even at the lower volume fraction, the "primary TiB" becomes the major limiting factor in macroscopic ductility for the 1.7B alloy. Fractography analysis of the 1.7B alloy shows tensile specimen fracture surfaces revealed 100% of the time that the initiation site is at a primary TiB particle. The 1.7B alloy exhibited limited plastic deformation, with the highest ductility of 3.5%. Characteristics of ductile-type fracture were evident from the presence of ductile dimpling of the  $\alpha+\beta$ . Also, the stress-strain curves as shown in Fig.29 indicate yielding and a clear ultimate stress. In Fig. 31 (a) the fracture surface of a typical Ti-6Al-4V-1.7B

mechanical tensile test specimen is analyzed through SEM secondary mode, where the fracture flow markings clearly indicate initiation at the dark primary boride. Figure 31 also shows a closeup of the fracture initiation boride, which most often exhibit inter-fracturing along the cross-section. Ultimately, the ductility of the 1.7B alloy was limited by the elastic limit of the primary TiB, allowing limited plastic deformation.

With this understanding of the mechanism of fracture in the Ti-B alloy leading to limited ductility in the 1.7B alloy, it was evident these primary borides needed to be eliminated to improve the tensile ductility. Recent findings have shown remaining in the hypoeutectic region ( $< 1.55\%B$ ) of the Ti-6Al-4V-xB phase diagram assures elimination of these primary borides [58]. Therefore, no primary borides exist in the 1.0B alloy, essentially alleviating the influential initiation site, and limiting ductility factor of these Ti-B alloys. Nevertheless, Ti-B alloys with greater than 1.55% B may have usefulness in applications that are designed for high specific stiffness with lower ductility requirements, or applications allowing transversely isotropic properties (i.e. some structural applications). For the 1.0B alloy no individual primary initiation site could be found within any of the tensile tested specimens. Strong evidence of work hardening followed by an ultimate load was indicated by the mechanical tensile results (see Fig. 29a), with ductility up to 13.5%. The fracture surfaces of the 1.0B alloy tensile specimens exhibited void coalescence and typical



ductile dimpling, with cup-cone behavior evident of ductile fracture mode (see Fig. 31(b)).

### Strength and Stiffness Modeling

It has been shown that the 1.7B alloy exhibited higher strength and stiffness than the 1.0B alloy. Influence of B amount was demonstrated by these higher properties, but loss in overall ductility could also be attributed to the increase in TiB phase. The response of the alloy to an applied load depends on many factors, including, and not limited to, the respective properties of the matrix and TiB phase, their relative volume fraction, the relative attributes of the TiB phase (i.e. aspect ratio, orientation relative to the applied load, distribution). There are two general approaches to assess the strengthening effects of second phases, continuum plasticity theory and dislocation models. In continuum theory strengthening can most often be represented by two mechanisms, load transfer to the harder TiB phase and constraint of matrix material flow [65]. The dislocation models relate the interaction of individual dislocations to barriers including TiB particulates, phase boundaries and grain boundaries. Strength will be increased due to the impedance of the dislocation glide by the harder TiB particles. The contribution of the TiB phase to overall strength will be analyzed using various strength models. In general, the strengthening contributions of the TiB phase can also be

separated by the size scale within the alloys. The micron size will contribute primarily in a load sharing role, while the sub-micron will demonstrate a more critical contribution in dislocation motion. It will be assumed that the needle-like TiB phase has a uniform strength, and fails when the applied stress exceeds their strength limit. Via *in situ* tensile testing, Boehlert *et al* [76] observed on tensile specimen surfaces TiB micro cracking in similar alloys prior to global yielding of the respective material when subjected to tensile loading. It will also be assumed that the stress-strain response of the TiB whiskers and  $\alpha+\beta$  matrix is a combination of elastic-TiB+matrix and plastic-matrix to fracture. A generalized stress-strain curve depicting the individual and combined elastic-plastic

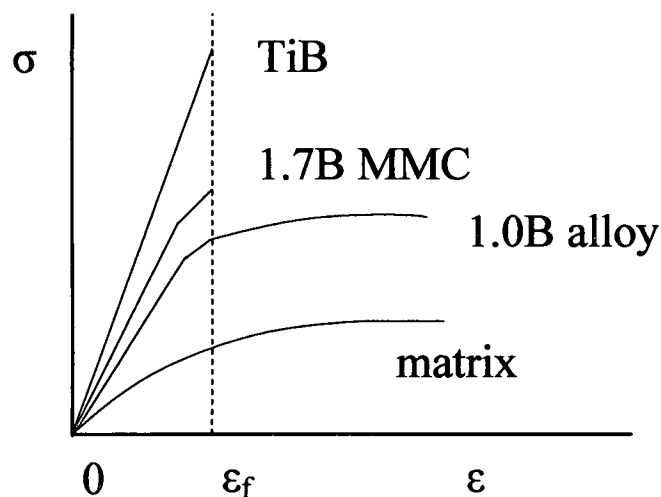


Figure 32 Illustration of elastic and plastic mechanistic contributions of individual components (phases) and resultant alloy, via  $\sigma$ - $\epsilon$  curve.

characteristics of the phases and alloys is shown in Fig. 32. A summary of the results and a comparison of the theoretical and experimental values are shown in Tables 5 and 6 for the strength and stiffness, respectively.

Table 5 Summary of yield strength increase,  $\Delta\sigma$  (in MPa), contributions from various mechanisms predicted using models.

Material	$\sigma_{LS}$	$\sigma_{HP}$	$\sigma_{SS}$	$\sigma_{OR}$	Total $\Delta\sigma$	
					Pred.	Expt.
Ti-6Al-4V-1.0B	257	56	-	-	313	249
Ti-6Al-4V-1.7B	411	74	-	20	505	478

Table 6 Summary of predicted total stiffness (elastic modulus, E) using various known models. Values in GPa.

Material	ROM Upper Bound	ROM Lower Bound	Voight	Halpin-Tsai	Shear-Lag	Experimental (ave)
Ti-6Al-4V-1.0B	134	116	N/A	129	124	142
Ti-6Al-4V-1.7B	144	118	N/A	139	125	150

## Strength Modeling

### *Load Sharing*

A material system where there are separate phases present, with distinctly different elastic/plastic properties, typically a stiff reinforcement phase surrounded by a softer matrix, the mechanism of preferential load sharing can be considered. Bao et al [77] predicted for relatively dilute systems (vol% < 0.2), the yield stress increase is approximated by,

$$\Delta\sigma_{LS} = \sigma_o \chi f \quad (1)$$

where  $\sigma_0$  is the Ti-6Al-4V matrix yield strength and  $\chi$  is the reinforcement factor. Bao *et al* derived the following expressions to estimate  $\chi$  for different particle shapes:

$$\chi = 0.38 \text{ for spheres}$$

$$0.69\lambda + 0.44/\lambda - 0.75 \text{ for aligned elliptical needles}$$

where  $\lambda$  is the aspect ratio of the needles. Since the TiB phase precipitates in the form of needles, and becomes aligned after the completion of the extrusion process, the TiB were modeled as aligned elliptical needles, and only the micron size-scale TiB were considered for both alloys.

Using an average aspect ratio,  $\lambda$ , equal to 10 for both alloys, and accounting for the micron scale TiB only, the volume%,  $f$ , equal to 5 and 8 for 1.0B and 1.7B, respectively, the increase in strength can be calculated. The strengthening effect due to load sharing of the TiB phase was realized by an increase in theoretical strength of 257 MPa for the 1.0B alloy and 411 MPa for the 1.7B alloy, respectively.

*Hall-Petch (grain boundary strengthening)*

It has been demonstrated that the Ti-B alloys being studied maintain a finer grain size than conventional Ti-alloys (i.e. Ti-6Al-4V), attributed to TiB phase acting as nucleation sites for additional grains, and the pinning effect of TiB on the grain boundaries. Figure 24 illustrates the grain size reduction that takes place with the addition of TiB particles, versus typical Ti-6Al-4V without TiB as shown in Fig. 25. This refinement of grain size provides a significant strength contribution. Tamirisa *et al* [63] proposed estimating the strengthening from this effect by assuming that each particle nucleates a single grain. Additional grains per unit volume, implies an increase in grain boundaries of the material. Dislocations pile up against grain boundaries and exert a force on slip systems in the adjacent grain. When the stress induced by the pile-up is sufficiently large to activate slip in the adjacent grain(s), macroscopic yielding will occur [78]. This grain size effect of the TiB particle contribution can be incrementally accounted for using the Hall-Petch relation [79,80]. The Hall-Petch relationship is probably the most commonly used theory that relates the strength of a particular metal to the observed average grain size. The Hall-Petch contribution can be estimated using the following equation, providing the relationship of yield stress to grain size

$$\Delta\sigma_y = k_d d^{-1/2} \sim k_d p^{-1/2} ((1-f)/f)^{1/6} \quad (2)$$

where  $\Delta\sigma_y$  is the change in yield stress,  $k$  is a material constant related to relative hardening contribution of the grain boundaries (typically around 0.1 MPa $\sqrt{m}$ ),  $d$  is the grain size,  $d_p$  is the particle size. Using average grain size,  $d$ , equal to 8  $\mu m$  and 4  $\mu m$  for 1.0B and 1.7B alloys, respectively, and volume fractions of 0.05 and 0.08, respectively, the H-P strength contributions for both alloys was determined. With higher volume fraction of TiB and smaller mean grain size, the 1.7B alloy (74 MPa) experiences a greater H-P strengthening contribution than 1.0B alloy (56 MPa).

### *Solid Solution Strengthening*

Another strengthening technique used in metals is alloying pure metals with impurity atoms that go into solid solution, either by substitutional or interstitial methods. Most often this is utilized to strengthen softer and weaker pure metals, and one of the most common examples is the addition of C to strengthen steels. Carbon is a very good solid solution strengthener in steels, and also has a high solid solubility (up to 0.5 wt%) [81] in titanium alloys. However, B on the other hand has a very small solid solubility (<0.1 at%) in Ti [81] therefore, no solid solution strengthening via B addition is expected for these alloys. In fact, the limited B that is temporarily trapped in the solid solution is eventually transformed into sub-

micron TiB for the 1.7B alloy via heat treatment, essentially eliminating any solid solution strengthening.

### *Orowan Strengthening*

A dislocation approach that may also contribute to the overall strength of the Ti-B alloys is the Orowan stress mechanism. In Orowan-strengthening the matrix is assumed to yield when the stress is large enough for the dislocations to bypass rigid particles. The stress that circumvents the resistance to dislocation movement is the critical stress, or Orowan stress. One caveat that becomes very important in whether or not the Orowan stress is applicable is the size of the TiB whiskers. Tamirisa et al illustrated the parabolic relationship that exists between the whisker diameter and the Orowan stress increment as a function of whisker volume fraction. The plot shows that nano-scale whiskers, with  $(l/d=10)$  are very effective in obstructing the dislocations for diameters less than approximately 50 nm, and a strength increment of up to around 100 MPa can be obtained [63]. Since the sub-micron TiB exist in the 1.7B alloy only, Orowan strengthening will be discounted for the 1.0B alloy. The majority of the sub-micron TiB diameters are on the order of 50-100 nm, and the volume fraction is less than 0.02, therefore, a conservative approach using the referenced Orowan  $\sigma$ -to-whisker diameter chart [63], results in an Orowan strengthening increment of around 20 MPa.

Table 4 summarizes the predicted strength contributions for the various models, and compares to the experimental values attained via mechanical tensile tests. The additive values of the individual contributions are in good agreement with the actual values predicting slightly higher yield strength for both alloys. The benefit of the TiB phase is clearly shown through load sharing mechanism, which accounts for more than 80% of the additional strength for both alloys. The stronger, but limited plastic TiB phase provides a means by which the localized load can be transferred from the more ductile  $\alpha+\beta$  phases to the stiffer TiB phase, ultimately, allowing for more load per unit volume. Additionally, reduction in grain size via grain boundary pinning by the TiB phase increases the strength through the Hall-Petch relationship. This theoretically accounts for the remainder of the strength increase in the 1.0B alloy and the majority of the remaining strength increase in the 1.7B alloy, with some contribution shown by Orowan strengthening with the presence of the nano-TiB needles.

### *Stiffness Modeling*

In general terms for these Ti-B alloys, stiffness is controlled primarily by the vol% TiB phase present in the alloy. Gorsse and Miracle et al [71] demonstrated this relationship in Ti-6Al-4V with 20 and 40% TiB present in the alloys, respectively. It was concluded that a near linear relationship



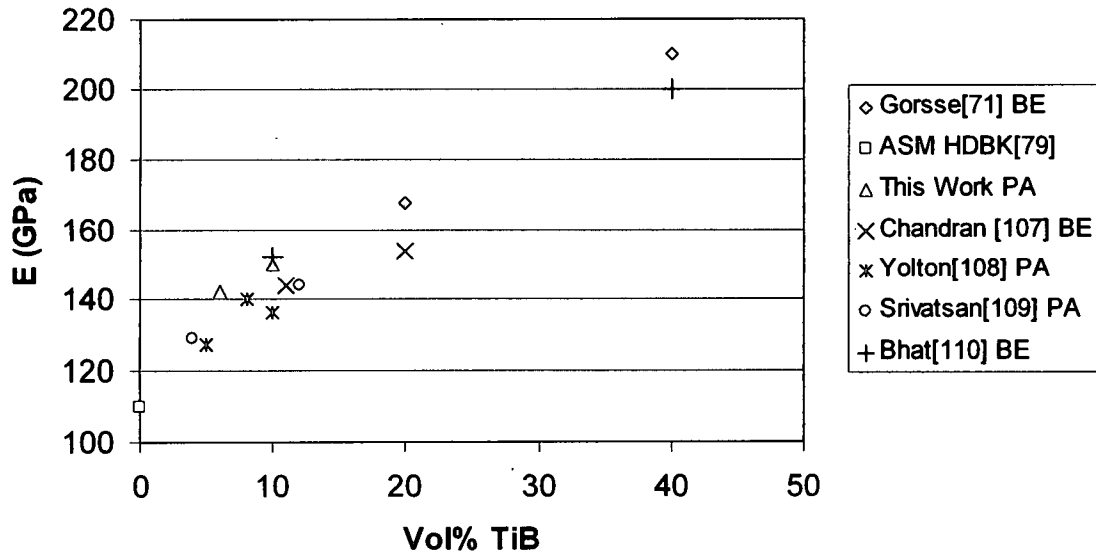


Fig 33 Tensile test (RT) results for Young's modulus as a function of vol% TiB in Ti-6Al-4V.

exists, and as the vol% of TiB phase in the material is increased, the bulk stiffness of the material increases. In Fig. 33 other published results of Young's modulus has been compiled and organized on a plot of Young's modulus versus vol% TiB in Ti-6Al-4V, demonstrating a near-linear relationship. When comparing the two Ti-B alloys analyzed in this study, Ti-6Al-4V-1.7B has a higher stiffness than Ti-6Al-4V-1.0B. However, other major factors such as morphology and distribution of the TiB phase also become important in influencing the overall stiffness. Additionally, orientation of the TiB needles relative to the applied load will also be instrumental in the stiffness response of the alloy.

### Rule of Mixtures

The prediction of the stiffening effect of hard particles in a metal has been demonstrated by various models [61,71,75,82]. Perhaps the simplest approach to evaluating the stiffness effect of the TiB phase particles in the Ti-B alloys being studied is by using the "rule of mixtures" methodology. The following equations [75] represent upper and lower stiffness bounds, respectively

$$E_c(u) = E_m V_m + E_p V_p \quad (3)$$

$$E_c(l) = E_m E_p / (V_m E_p + V_p E_m) \quad (4)$$

where , E and V denote the elastic moduli and volume fraction, respectively, and the subscripts c, p, m represent the composite, reinforcement and matrix, respectively. Using  $E_m$ ,  $E_p$ ,  $V_m$ , and  $V_p$  equal to 110 GPa [3], 482 GPa [71], 0.91 and 0.09 for 1.7B alloy results in an upper and lower bound of 144 and 118 GPa, respectively. Using 0.94 and 0.06 for  $V_m$  and  $V_p$ , respectively, for 1.0B alloy predicts 134 and 116 GPa for the upper and lower bounds. These bounds appear to underestimate the stiffness for the upper bound for both alloys, perhaps due to lack of the TiB alignment influential aspect ratio of the TiB taken into account.

Continuing the assessment of theoretical stiffness using forms of rule of mixtures approach, the Voigt model was evaluated. This modified rule of mixtures model was formulated for systems in which the matrix and "reinforcing" constituents have equivalent strains during elastic loading. An alternative model, Reuss model [83], was formulated with the assumption that the matrix and reinforcement have equivalent stresses under loading. These aforementioned models, with the qualifying assumptions of equal strain and equal stress do not accurately represent the conditions observed in particulate reinforced MMCs [84].

In the two alloys studied in this paper, the reinforcing TiB phase can be assumed to be aligned with the longitudinal direction (extrusion direction) of the extruded bar. This alignment of TiB whiskers provides a stiffer material versus one with randomly dispersed TiB whiskers. Philliber *et al* [65] noted the difference in resultant stiffnesses of aligned versus random TiB by using various prediction models for stiffness. It was concluded that randomly oriented needles provided much lower stiffness results than aligned needles, which coincides quite well with Gorsse *et al* [71] experimental data of transverse versus longitudinal direction, for 20 and 40 vol% TiB. It was also concluded by Philliber *et al* that randomly oriented needles provide slightly more stiffness than spherical particles.

Another approach by Cox [85], and subsequent further development by Nardone and Prewo [86] rationalized the total MMC

stiffness via what is known as shear-lag principle. The basis of this model is that load is transferred from the matrix to the fiber by means of a shear stress operating on the matrix-fiber interfaces parallel with the loading direction [65]. The model is often used for material reinforced with short fibers (i.e. TiB phase), as is the case with the Ti-B alloys. The modified shear-lag model calculates the total stiffness with the following equation [87]:

$$E_c/E_m = (1-V_p) + V_p(E_p/E_m) \times (1 - \tanh(X)/X) \quad (5)$$

where

$$X = (1/d) [(1+u_m) (E_p/E_m) \ln(V_p)^{-1/2}]^{-1/2} \quad (6)$$

with  $u_m$  and  $1/d$  the Poisson's ratio of the matrix and whisker aspect ratio (length to diameter), respectively.  $E_m$  and  $E_p$  are equal to 110 and 482 GPa, and  $V_p$  equal to 0.09 and 0.06 for 1.7B alloy and 1.0B alloy, respectively. And using  $u_m = 0.34$  and  $1/d = 10$ , respectively, predictions of 124 and 125 GPa for the two alloys 1.0B and 1.7B are made. The shear-lag predictive values underestimate the stiffness of both alloys when compared to the experimental values of 142 and 150 GPa, respectively, which appears in agreement with Srivatsan et al's [82] study. The predicted values do, however, fall between the upper and lower predicted stiffness bounds.

Finally, Halpin-Tsai formulated a relationship of matrix/whisker modulus and volume fraction, which also takes into account the whisker aspect ratio,  $l/d$ . The longitudinal stiffness is expressed as [88]

$$E_c = [(1+2(l/d)\eta V_p)/(1-\eta V_p)]E_m \quad (7)$$

where

$$\eta = (E_p - E_m)/[E_p + 2(l/d)E_m] \quad (8)$$

with nomenclature and associated values the same as mentioned earlier. Using the Halpin-Tsai model the stiffness for the 1.0B and 1.7B alloys result in 129 and 139 GPa, respectively.

### Conclusions

By working and/or heat treating alpha+beta alloys below or above the  $\beta$  transus, substantial microstructural variations can be produced in titanium alloys. Consequently, alpha+beta alloys can be hardened by heat-treatment, such as solution treating and aging (STA) for maximum strength. Microstructures in Figs. 1 and 28, give an indication of the potential final morphologies that can be produced for Ti-6Al-4V and the Ti-B alloys, Ti-6Al-4V-1.0B and Ti-6Al-4V-1.7B. There are benefits to producing particular microstructures and morphologies that are shown in Figs. 28(a-o). The following lists some of the major conclusion points that can be drawn from the heat treatment study:

- The ability to tailor  $\alpha+\beta$  phases via heat treatments, while TiB phase remains virtually unchanged is an important attribute of Ti-6Al-4V-xB alloys to allow use in specific applications.
- There is a near linear relationship of volume fraction TiB versus strength and stiffness, and strength and stiffness is a function of TiB volume fraction, orientation, size, distribution.
- The strength is related to heat treatment condition as expected, indicating vital role of the  $\alpha+\beta$  phases, while stiffness range across heat treatment conditions was quite level, with the exception of drop in modulus for the HBA conditions, indicating the stiffness-controlling factor of the TiB phase.
- 1.7B alloy had higher strength (up to 1695 MPa) and stiffness (150 GPa) than 1.0B alloy (up to 1371 MPa and 142, respectively), but 1.0B alloy had higher ductility (up to 13.5% elong), the 1.0B alloy has good ductility for all heat treatment conditions, as low as 9.6% and as high as 13.5%, which compares favorably with standard Ti-6Al-4V.
- An important eutectic point of 1.55 wt% exists for Ti-6Al-4V-xB materials.
- A classical ductile fracture for 1.0B alloy in an elastic-plastic behavior, while 1.7B alloy response of ductile fracture with limited plastic deformation due to the primary TiB limiting ductility, and verified as fracture initiation site of hypereutectic alloy 1.7B.

- Primary strength contributions of TiB phase via load sharing mechanism. Grain refinement (i.e. H-P) also plays a key role in the overall alloy strength.
- Models for total stiffness slightly underestimates bulk stiffness of Ti-B alloys studied, with Halpin-Tsai comparing best with the experimental results.

### Recommendations

Results indicate heat treatment parameters optimized for conventional Ti-6Al-4V may not be optimum for PA Ti-6Al-4V-xB alloys due to variations in  $\alpha/\beta$  phase proportions and effect of the TiB phase on the  $\beta \rightarrow \alpha$  phase transformation. Consider, for example, a solution treatment higher in the  $\alpha+\beta$  phase for if optimum hardness is to be achieved. Additional studies are required to optimize heat treatment-microstructure-property relationships for hypoeutectic Ti-6Al-4V-B alloys. For hypereutectic Ti-6Al-4V-B alloys, heat treatment has no significant effect on the ductility as it is controlled by the primary TiB. Also, in stiffness modeling of the alloy an approach can be taken whereby the TiB size-scale individual stiffness contributions can be weighted appropriately in order to determine the overall alloy stiffness.

Also, the T-T-T relationship of the heat treatment schedule plays an integral part in the final microstructure-property relationship. Specifically, the effect of the heat treatment on the presence of the nano-TiB phase needs to be monitored when selecting a specific heat treatment schedule. In the as-extruded state boron may still be trapped in solid solution, providing a different strengthening mechanism. Additional nano-TiB appear after short-time (<2hr depending on temperature) heat treatment. Depending on the duration of anneal time and temperature, the TiB phase (as-well as the  $\alpha+\beta$ ) can be in the form of nano-TiB and micro-TiB, or micro-TiB only. For example, heat treating above the  $\beta$ -transus will dissolve the nano-TiB quicker than a solution treatment below the  $\beta$ -transus at the same duration. The dissolution of the nano-TiB at the expense of the micro-TiB plays a key role in the overall material property relationship. Therefore, from an engineering standpoint, it is imperative in the course of heat treating the Ti-B alloy that controls are in place to assure correct monitoring of the heat treatment parameters. The next chapter provides an in-dept analysis of the TiB phase kinetics, and this information can be very helpful when selecting and monitoring a heat treatment schedule.



### CHAPTER III

#### THERMAL STABILITY OF TiB PHASE

##### Summary

In this study, the same PA powder was utilized, composition Ti-6Al-4V-1.7B, as in the previously discussed heat treatment study. The powder was compacted and hot extruded in like manner as to previous baseline material. The extruded material was further sectioned and subjected to predetermined annealing parameters. After typical metallography techniques were used to prepare the post-annealed material for SEM analysis, digital images of the microstructures were captured. Further stereological image analysis was performed on the captured SEM images as to ascertain quantitative data. The data was used in conducting the coarsening kinetic study of the TiB phase in the aforementioned Ti-B alloy. Finally, selected coarsening models were used in order to gain a better understanding of the growth behavior of the TiB phase under thermal exposure. A flow diagram summarizing the sequence of steps used in this study is shown in Fig 34.

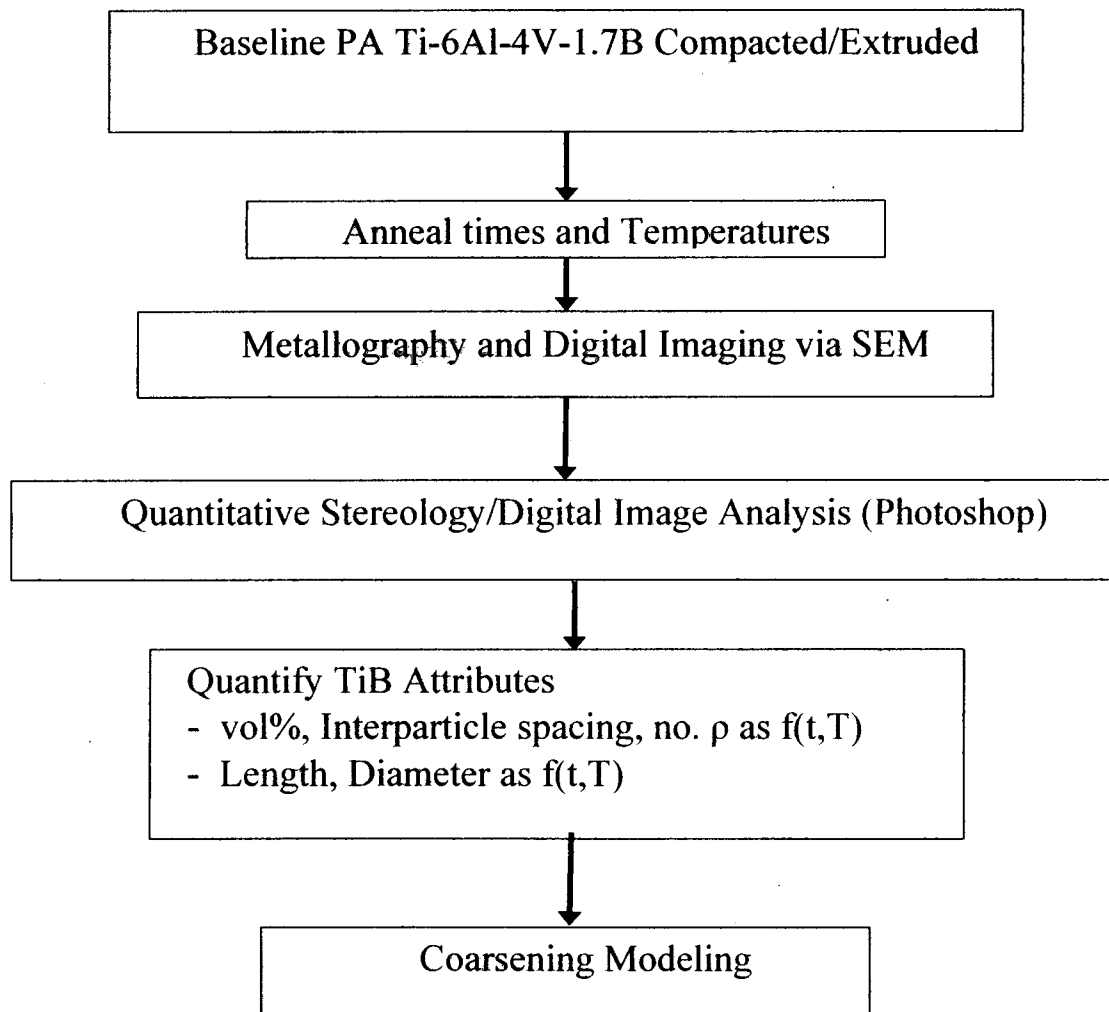


Figure 34 Flow diagram summarizing the sequence of steps used in the thermal stability study of the TiB phase.

### Experimental

#### Program Materials

The powder used in this study was the same powder as the higher B-containing alloy used in the heat treatment study. The material composition, Ti-6Al-4V-1.7B, used in this study was produced in like manner

as the powders used in the heat treatment study via a pre-alloyed (PA) powder metallurgy approach. The chemical composition of the material in wt% is provided in Table 3 in Chapter II. The inert gas-atomized powder, at a maximum diameter -100#, was procured from Crucible Research Corporation, Pittsburgh, PA. Figure 16 in Chapter II details the typical size distribution, and Figure 17b (see Chapter II) SEM image shows typical diameter and morphology of the PA powder used in the study. Figure 17d (see Chapter II) also shows a higher magnification SEM image of the sectioned powder particle, which illustrates the existence of the TiB whiskers (dark particles) within the rapidly solidified powder particles prior to thermo-mechanical processing or heat treatment.

The same processing parameters (see Fig. 4, Chapter II) as used in the heat treatment study was used, with the powder transferred into a wrought Ti-6Al-4V 6.35mm (0.25 in) thick canister with dimensions 15.2cm (6 in) length x 7.6cm (3 in) diameter, degassed at 300°C for 24 hours and sealed via crimp and weld under vacuum. The sealed can was thermally soaked for 1 hour at 1200°C, and subjected to 1400 MPa pressure for 3 minutes in a blind die extrusion chamber. Finally, the compacted canister was subsequently extruded at 1100°C, under a ram speed of 6 mm/s and extrusion ratio of 15:1, utilizing a round-to-round conical extrusion die. The flow diagram in Fig 4 (see Chapter II) illustrates the processing steps used in creating the final material to be subjected to further annealing

parameters. The extruded material became the baseline for comparison to the thermally treated specimens.

#### Annealing Parameters

The extruded rod of approximately 1.5 m x 2cm diameter, was sectioned into smaller 40-50mm thickness disks that were subsequently

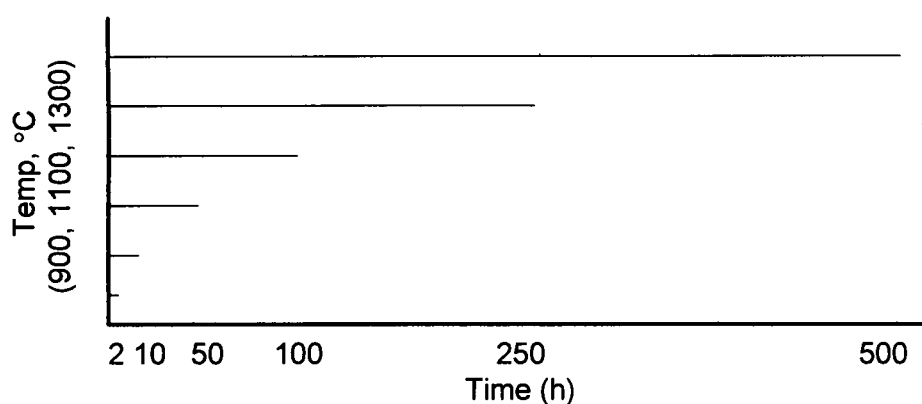


Figure 35 Summary of anneal temperatures and times for coarsening study.

furnace annealed in Ar atmosphere at pre-determined times and temperatures. The schematic in Fig 35 summarizes the relative times and temperatures used in the coarsening study.

#### Metallography and Preparation

The furnace annealed discs were sectioned in half parallel to the extrusion direction in order to expose both transverse and longitudinal surfaces. The transverse and longitudinal sections for all applicable time-temperature parameters were separately mounted in conductive mount material for future SEM analysis. The mounted specimens were further

subjected to standard metallographic laboratory techniques for surface preparation. The surfaces were prepared using a typical routine for rough polishing of 240 to 600 grit SiC papers, followed by final surface finish preparation using diamond paste from 15 $\mu$ m to 3 $\mu$ m in size. The surfaces were final polished to 1 $\mu$ m, and finally 0.05 $\mu$ m using an automatic laboratory vibromet. The mounted specimens that comprised the transverse direction material were subsequently cleaned and ready for SEM analysis. The longitudinal specimens were further subjected to 10-15 minute etching using standard Kroll's etchant, which allowed for full exposure of the TiB lengths. These longitudinal specimens were final similarly prepared for SEM via submersion in alcohol.

#### Image Analysis and Microstructural Quantification

Digital images were captured for all the specimens via SEM back-scattered electron imaging (BEI) for the transversely sectioned specimens, and secondary mode for the longitudinally and etched specimens. The micrographs detailing the transverse section were used in the TiB diameter study, while the etched longitudinal sections were used in the length study analysis.

Digital imaging analysis procedures were performed on the captured SEM images in order to quantify the dimensional change in TiB phase as a function of time and temperature. Two separate techniques

were used to measure the TiB lengths and diameters, respectively. Digital imaging analysis procedures, using Photoshop™ with the addition of FoveaPro™ software plugins, were performed on the captured SEM images in order to quantify the dimensional change in TiB phase as a function of time and temperature. Using the digital images captured for the etched specimens as shown in Fig. 36a the lengths of the TiB were measured manually with the aforementioned digital imaging software.

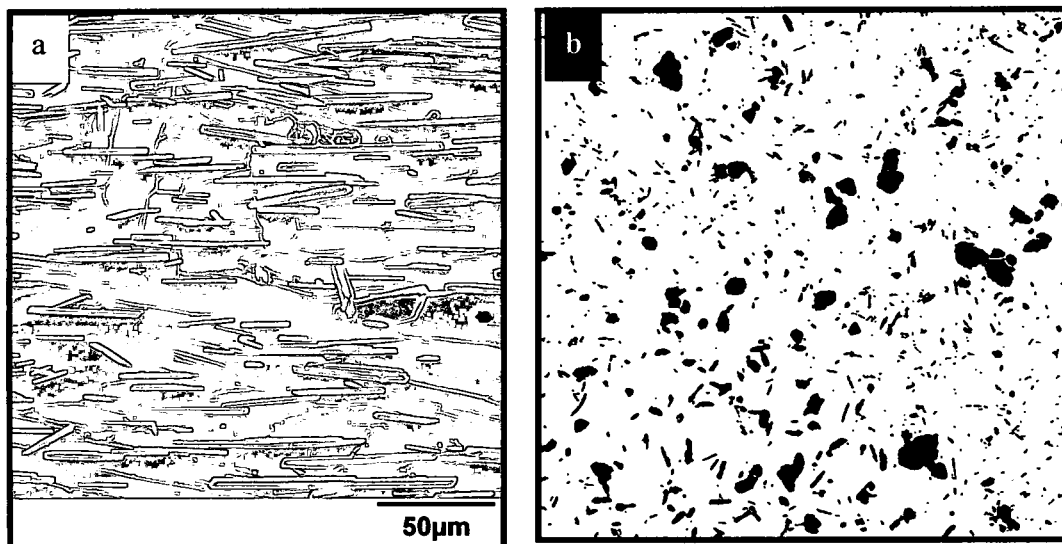


Figure 36 Illustration of SEM images used in thermal stability study, (a) secondary image of longitudinal etched sample capturing TiB lengths, (b) thresholded TiB cross-sections (diameters). Horizontal is extrusion direction for 3a.

The transverse BEI SEM images captured for the diameters were thresholded to reveal only the TiB cross-sections (diameters), as shown in Fig. 36b, and were measured automatically via writing a computer macro within the Photoshop™ software. The TiB cross-sections were measured as equivalent diameters. The equivalent diameter of a feature is a linear

distance, often used for size distributions of particles, that corresponds to the diameter of a circle having the same area as the feature [89].

## Results and Discussion

### Starting Microstructure

The extruded material had an equiaxed- $\alpha$  microstructure with about 10 vol% finely dispersed TiB precipitates. The TiB precipitates in the form of needles with the highest percentage generally 0.5-5  $\mu\text{m}$  in diameter and aspect ratio of about 10. These TiB fall into the micron-scale category and are eutectic needles. A lower fraction of TiB needles was also present with a diameter range of 30-50 nm and similar aspect ratio. Figure 37 illustrates the typical starting material microstructure (baseline) used in this study, with the longitudinal (extrusion) direction shown in 37a and transverse direction shown in 37b, revealing uniformly distributed TiB needles throughout the matrix. The eutectic needles typically align themselves along the extrusion direction. The images in Figs. 37c and d, represent the etched and thresholded versions of the longitudinal and transverse directions, respectively, revealing only the TiB phase of the material. The etching of the longitudinal sections, as shown in Fig. 37c, was not only useful in TiB length measurement, it also assisted in verifying

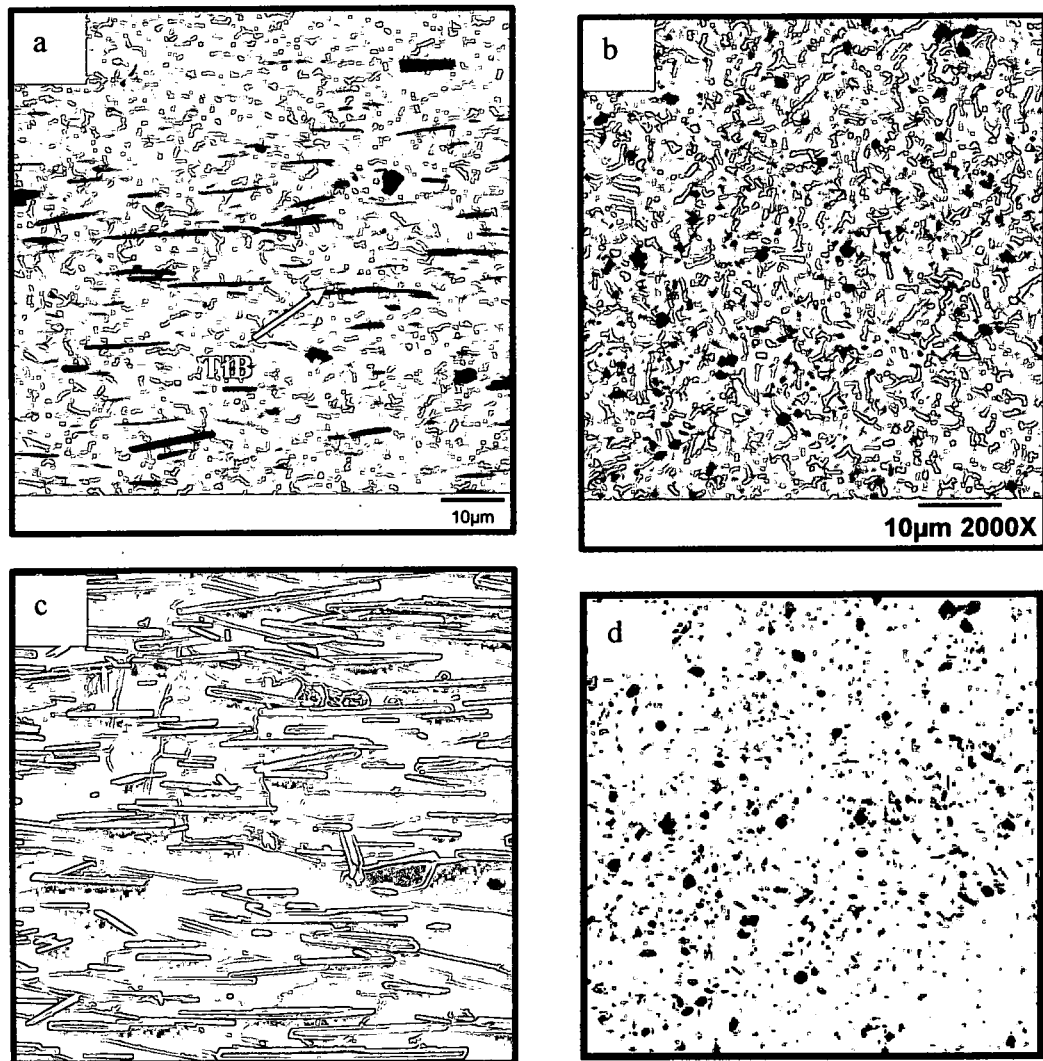


Figure 37 SEM images of starting microstructure (a) longitudinal, (b) transverse, and subsequent images of (c) etched specimen in longitudinal, and (d) digitally thresholded image in transverse directions, used in TiB coarsening study.

the morphology of the TiB phase to be in the form of needles. A third, very small fraction ( $<0.5\text{wt}\%$ ) of primary TiB needles were also present, but were disregarded in this experiment. These large primary borides have subsequently been avoided in future alloys primarily via remaining in the hypoeutectic region of the applicable phase diagram. Figure 26 in



Chapter II depicts the tri-modal TiB size scale presence in this material. The primary TiB is assumed to have limited effect on the coarsening kinetics primarily due to its minimal volume %, large interparticle spacing, and minute point density relative to the other two size scales. For this study, the primary TiB size will be disregarded with focus only on the micron and sub-micron scale TiB.

The nano-scale needles remain randomly dispersed throughout the matrix even after extrusion, as can be seen in the micrograph in Figure 38. Figure 38a is a transverse cross-section of the extrusion, clearly illustrating the randomly dispersed nano-scale TiB throughout the matrix, within the equiaxed structure of the micron-scale TiB. Fig 38b, shows a higher magnification of the same specimen to reveal the typical nano-scale TiB particles present. Both of these TiB size-scales were taken into account in this particular coarsening study.

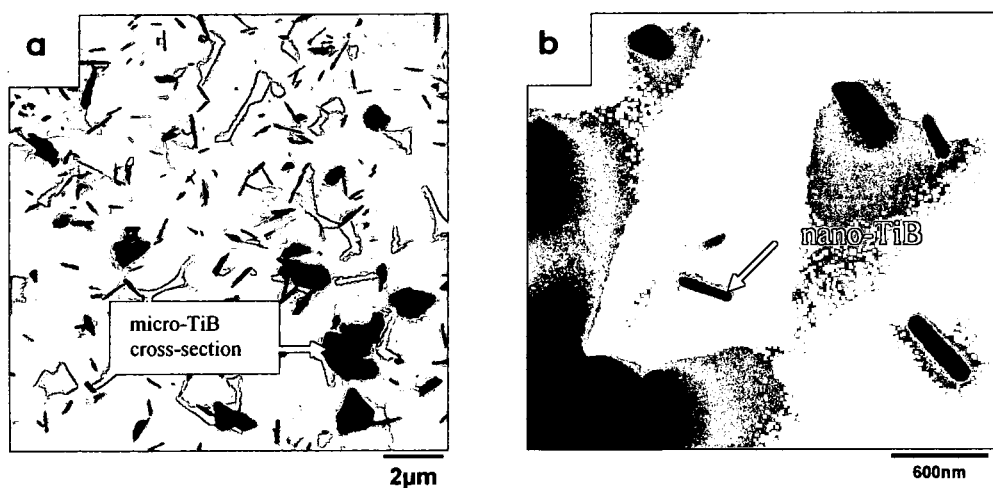


Figure 38 Higher magnification SEM images in the transverse direction, showing the nano-scale TiB needles randomly dispersed throughout the matrix microstructure, and micro-TiB cross-sections.

## Annealing Parameters

The range of chosen times and temperatures was sufficient in addressing kinetics above and below the  $\beta$ -transus for this particular Ti alloy (see Fig 35). It has been experimentally shown by Tamirisakandala et al the  $\beta$ -transus is around 1050C +/- 10C [54] for this PA processed Ti-6Al-4V-1.7B alloy. Therefore, the lower temperature, 900°C, was assured to be below the  $\beta$ -transus, and the highest temperature, 1300°C, was known to be above the  $\beta$ -transus. The anneal times from 2 to 500 hours gave a range near potential processing design parameters on the lower end, and the extreme case of 500 hours to provide ample information to facilitate understanding of the coarsening kinetics of the material system during service.

## Microstructural Evolution

### Diameter and Length

Digitally thresholded SEM images of specimens annealed from 2 to 500 hours at various temperatures are shown in Figure 39. The images are representative microstructures revealing only the TiB phase in the transverse direction. In the transverse direction showing the nearly

equiaxed structure of the TiB, the TiB cross-sections were measured as an

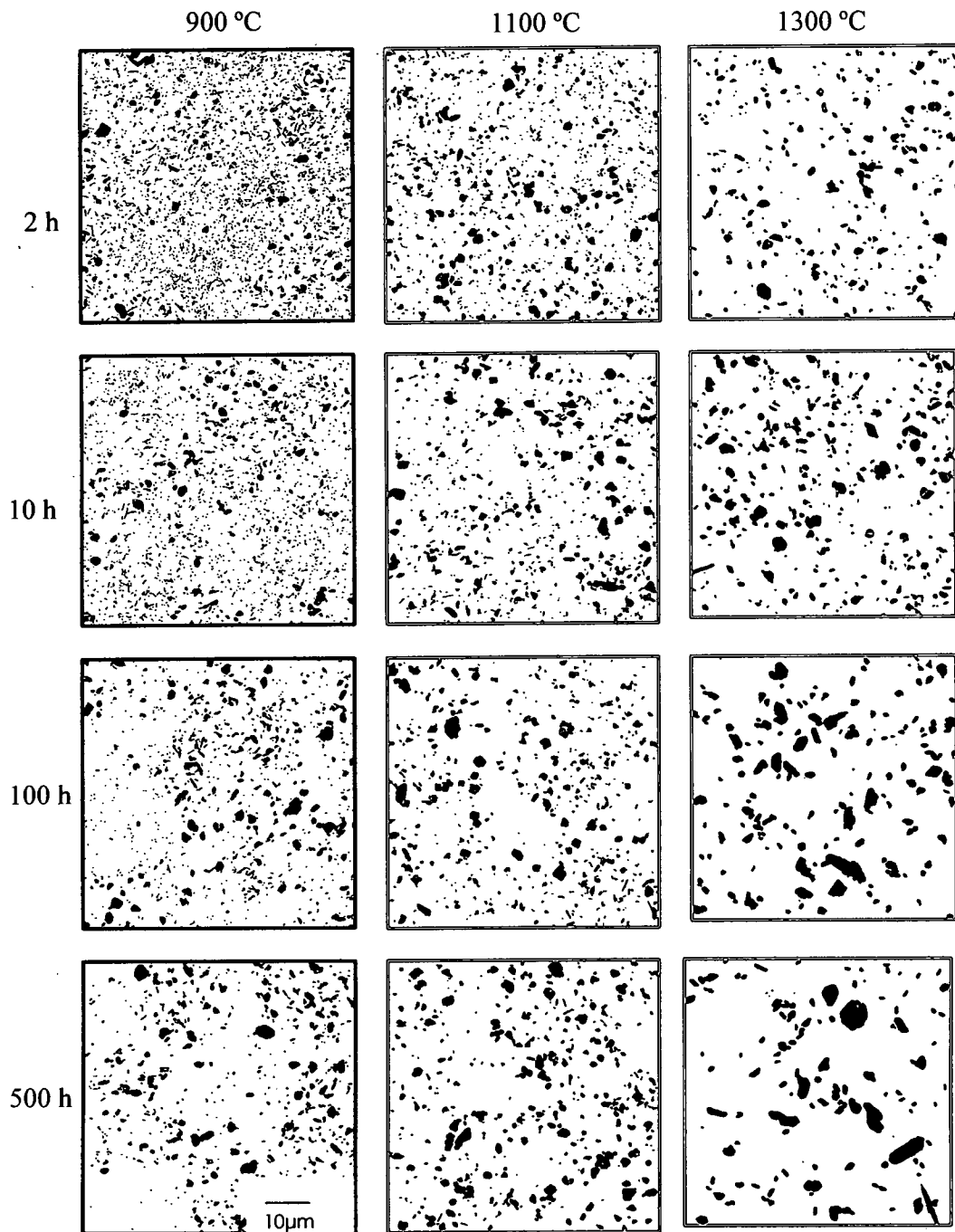


Figure 39 Thresholded SEM images of samples heat treated at different times and temperatures revealing only the TiB cross-section (diameter).

equivalent diameter. The mean equivalent diameter increases with increasing annealing temperature and dwell time. It is also evident from these thresholded images time-dependent particle coarsening is occurring, while the total number of particles per unit volume is decreasing. Figure 40 illustrates the increase and distributional change in the TiB mean equivalent diameter as a function of time and temperature. The baseline (no anneal time) distribution clearly shows a tight distribution with a mean at around .2  $\mu\text{m}$ , whereas after 500 hours at 1300°C, a shift in the entire equivalent diameter distribution has occurred with a mean of approximately 1.5  $\mu\text{m}$ . The range of the equivalent diameter for the maximum temperature of 1300°C is relatively small, with a maximum equivalent diameter of approximately 7.5  $\mu\text{m}$ . The mean diameter increases from 0.21  $\mu\text{m}$  in the as-extruded condition to 0.67, 0.84, and 1.51 for 900, 1100, 1300°C for 500 hours anneal, respectively. Even though the mean diameter increases up to approximately 7x for 500 hours at 1300°C, the mean diameter remains relatively small, giving strong verification of the good thermal stability of the TiB phase.

Figure 41 compares the distribution in length-scale of the TiB needles as a function of temperature and 500 hours anneal time versus no heat treat condition (baseline). Clearly there is a shift in mean length from the baseline condition (mean = 5  $\mu\text{m}$ ) for all three temperatures studied, with the largest shift at 1300°C (mean = 24  $\mu\text{m}$ ). The sub-micron needles are still

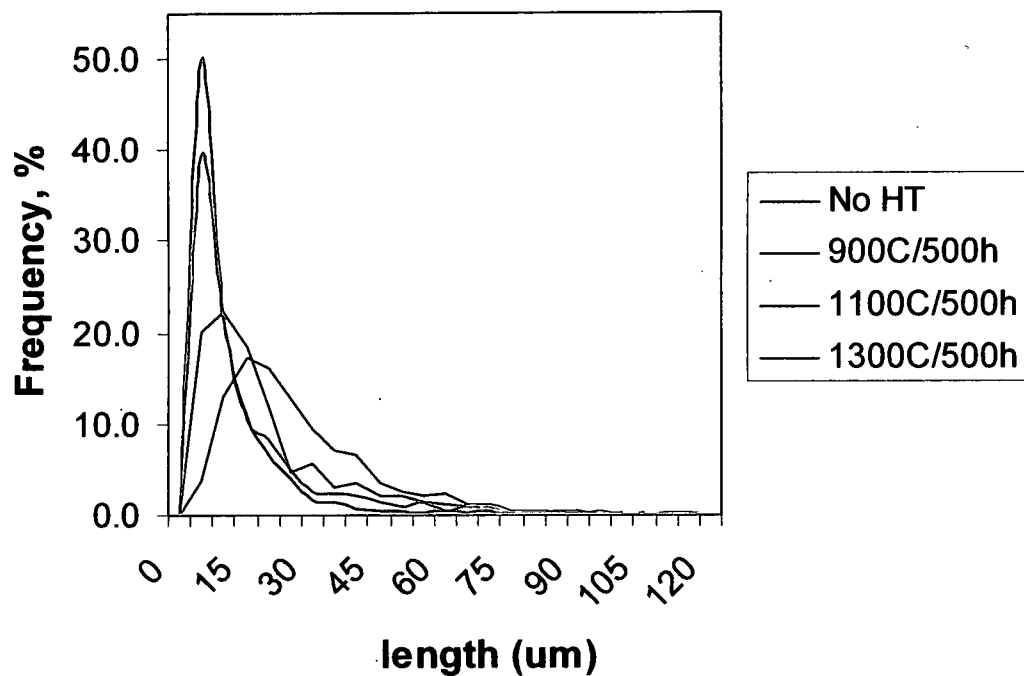
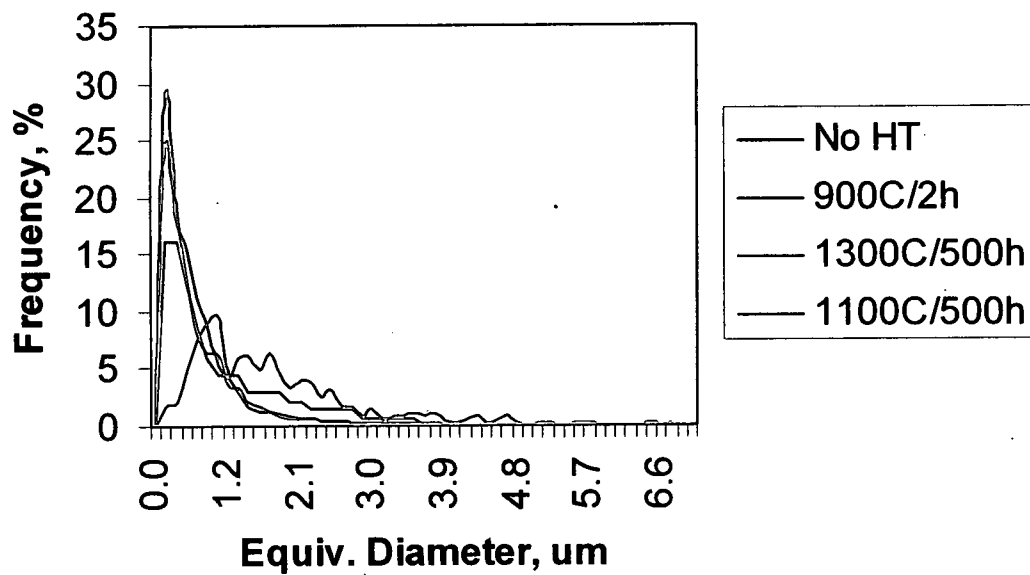
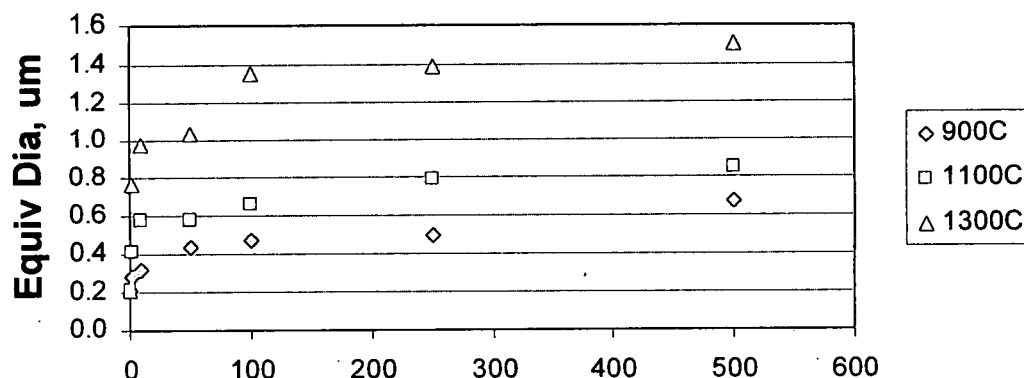


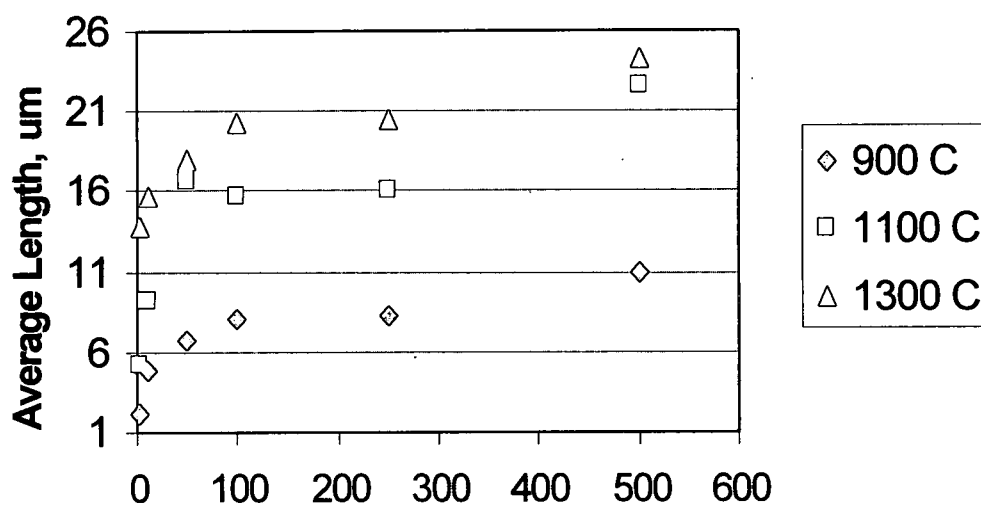
Figure 41 Distribution of TiB average length versus frequency as a function of time and temperature.

present at 900°C, and influence the overall mean even at 900°C for 500 h.

However, exposure to 1100 and 1300 °C for 500 hours completely consumed the sub-micron TiB needles, with only micron-scale TiB needles remaining. Figures 42a and b show mean equivalent diameter and



(a) time, h



(b) time, h

Figure 42 (a) Mean equivalent diameter, and (b) average length at various times as a function of temperature.

average length results summary of the coarsening of the TiB needles as a function of various times and temperatures. There is relatively small growth of the TiB needles along the diametral direction, where the mean equivalent diameter, even at the combination 500 h @ 1300°C, coarsened to only around 1.5  $\mu\text{m}$ . The mean equivalent diameter for conditions at 900 and 1100 °C, respectively, indicate a somewhat level coarsening up to approximately 0.9  $\mu\text{m}$ . The coarsening rate of the length appears to be faster than it is for the diameter, with a range in mean length from 2  $\mu\text{m}$  (2 h @ 900°C) to 24  $\mu\text{m}$  (500 h @ 1300°C).

#### Point density and Interparticle spacing

A plot of point density versus  $\log t$  indicates a rather abrupt change in slope from the 0 to 2 hours anneal time range versus 2 hours and longer (see Fig. 43a). At 1300C, the point density quickly decreases from 121 at 0 hours to approximately 11 per  $\mu\text{m}^2$  (1/100) with only 2 hours anneal time, and appears to level off thereafter. It is apparent that dissolution of the smaller particles at the higher temperature is occurring relatively early on, while the subsequent diametric coarsening increases relatively slowly. Below the  $\beta$ -transus at 900C, the rate of coarsening progresses slower, while the point density decreases near linearly versus log time, and the interparticle spacing (see Fig. 43b) increases from 0.2 $\mu\text{m}$  to around 0.8 $\mu\text{m}$

throughout the range of times. The relative coarsening parameters suggest good thermal stability of the TiB phase.

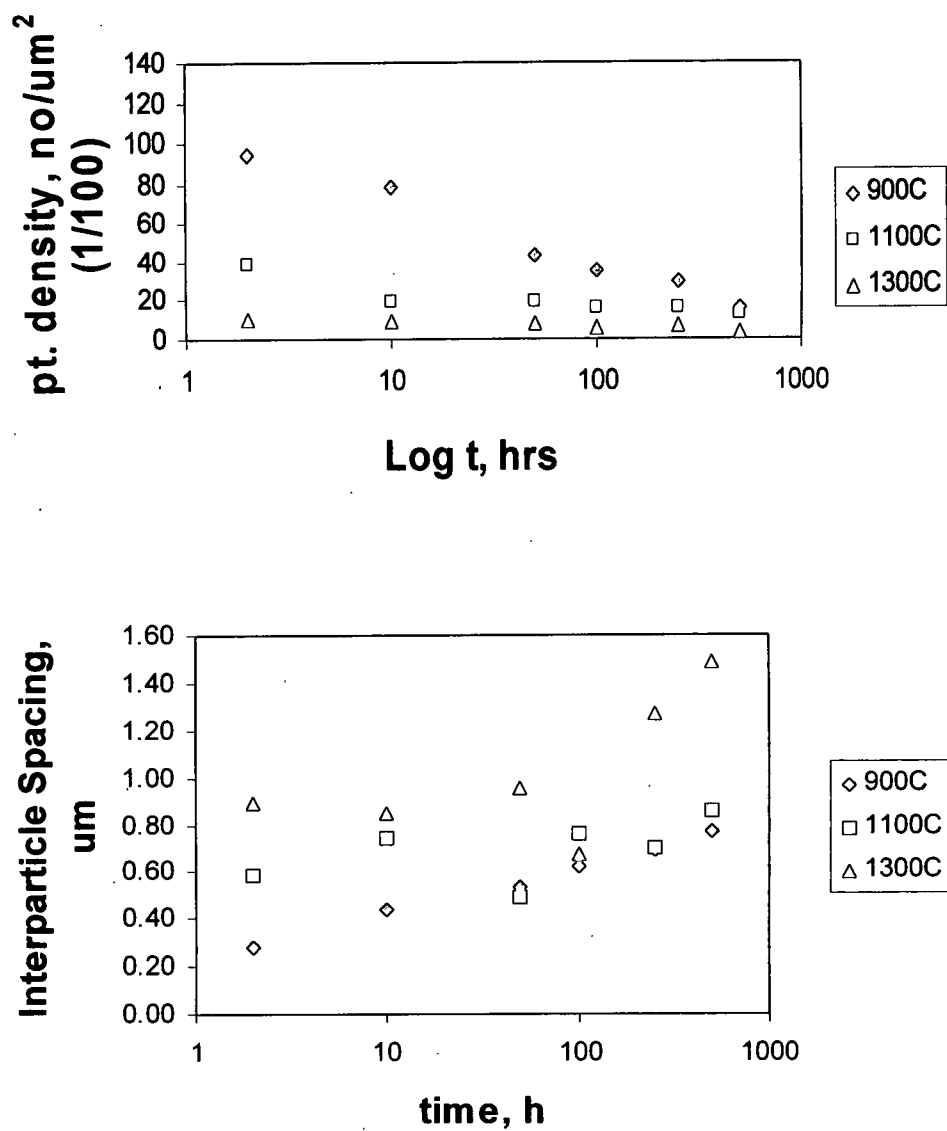


Figure 43 Plots of (a) point density and (b) interparticle spacing for TiB phase as a function of time and temperature.



The coalescence of the TiB needles can be described by the classical Ostwald-Ripening (to be discussed in more detail in the modeling section) effect especially at the highest temperature of 1300°C, whereby the finer nano-scale (length < 500 nm) TiB have completely dissolved after only 2 hours exposure to temperature. However, the rate at which the finer TiB needles are alleviated at 900 and 1100°C is quite different. After 10 hours exposure to 1100°C a very small amount of nano-TiB needles can be found, and none after 50 hours, yet after 500 hours at 900°C the smaller needles are still present to some degree. Figures 44(a-c) illustrate the time-temperature dependence on the nano-scale TiB presence with representative micrographs at the relevant times and temperatures.

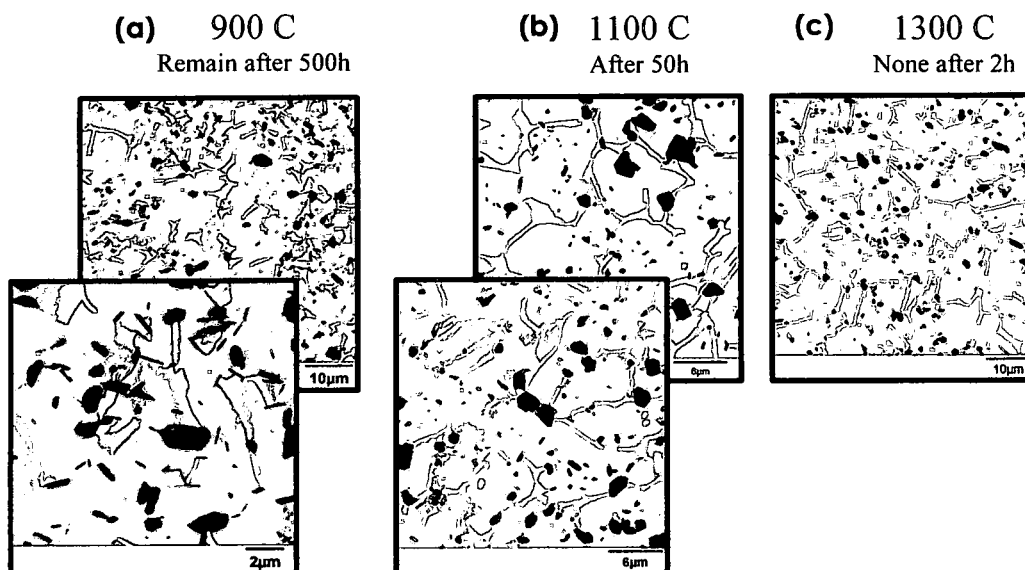


Figure 44 Illustration of the time-temperature dependence for Ostwald-ripening effect at various temperatures for dissolution of sub-micron TiB.

## Origin of nano-TiB

Another interesting discovery was made regarding the nano-scale TiB. It was discovered that additional nano-scale TiB appear after annealing at the lower 900C temperature for 2 hours. This phenomenon was experimentally evident after quantitatively comparing the results for the as-extruded average length versus the results at 900C for 2 hours. The average length decreased, as opposed to increasing which is expected. The mean diameter increased only slightly but within the standard deviation range. During the rapid solidification process of producing the powder, boron is trapped in solid solution, even though boron has very limited equilibrium solubility in titanium. After exposing the material to compaction at 1200C, hot extrusion at 1100C, and post-annealing, the boron is released forming additional TiB. Figs 38a,b high resolution SEM images illustrate the additional randomly dispersed nano-TiB present within the Ti-6Al-4V-1.7B alloy after 2 h anneal at 900C. This evolution of TiB is short lived as the driving force controlling the system kinetics becomes dominated by the particle coarsening after a relatively short period of time. After 10 hours at 900 °C the mean equivalent diameter and lengths increase beyond that of the baseline no heat treat condition. The higher temperatures of 1100 and 1300°C essentially eliminated the sub-micron TiB needles after 50 and 2 hours, respectively.

## Coarsening Kinetics Modeling

### *Ostwald-Ripening and LSW Theory*

In a two-phase alloy (i.e. Ti-6Al-4V) coarsening of a precipitate phase during high-temperature exposure is known to be driven by reduction in energy associated with the matrix-precipitate interfaces [90]. The driving force for particle coarsening is a process in which the material system lowers its total energy by reducing its interfacial area. The microstructure is said to be unstable until the total interfacial free energy is at a minimum [90, 91]. Coarsening occurs by the dissolution of the smaller particles, and concurrent growth of the larger particles, with diffusion in the direction of the larger particles. This growth in larger particles at the expense of the smaller particles is classically known as Ostwald-ripening effect. This results in an increase in the average particle size as a function of time, and a simultaneous decrease in the number of particles in the system. In the Ostwald ripening theory, several assumptions are made pertaining to the material system: a low volume fraction of particles ( $<0.2$ ), mass transport due solely to diffusion within the matrix, spherical particles (giving rise to an isotropic interfacial energy), and a stress-free matrix [92].

Lifshitz, Slyonov and Wagener (LSW) in 1961 found that in the long-time limit, the system approaches a self similar regime. In this regime, the

particle size distribution becomes time invariant when scaled by the time-dependent average particle radius [92]. The following section will focus on the LSW theory for particle coarsening as it pertains to the TiB phase in this material system.

Several available models to describe the particular coarsening kinetics for the TiB needles were evaluated to determine the rate-controlling mechanism(s). Initially, the volume diffusion-controlled particle coarsening was analyzed using the classical LSW modified by Greenwood [93-95] model for coarsening. In this model, there is an independent relationship between the growth of the particles and locations of all the other particles. An assumption for the LSW theory is generally restricted to small volume fractions (<0.2) of dispersed phase. The theory states the particle coarsening can be described using the equation

$$d^3 - d_0^3 = k(T)t \quad (10)$$

where  $d$  is the average particle size at a time  $t$ ,  $d_0$  is the average particle size at  $t=0$ ,  $T$  is the temperature, and  $k$  is rate constant at the temperature  $T$ .

Eventually, there have been modifications of the LSW model to allow for higher volume fractions of particles [96-98]. Ardell, Voorhees and

Davies et al allowed for a volume fraction factor within the original LSW equation. The rate constant  $k(T)$  was replaced by  $k(f,T)$  and Eq.1 became

$$d^3 - d_0^3 = k(f,T)t \quad (11)$$

where  $f$  is the volume fraction of particles and  $k$  is a function of  $f$  as well as the temperature. The modified model allows for a broader particle size distribution, with increasing particle volume fraction, while still being based on volume diffusion. This model will not be used in the TiB coarsening study, as the original assumptions of  $f < 0.2$  for the LSW model is valid for Ti-6Al-4V-1.7B where TiB  $f=0.1$ .

Other models have been developed which concentrate on particles that are generally assumed to be along the grain boundaries instead of inside grains in the matrix [99]. In this case, the rate of coarsening increases due to grain boundary –controlled diffusion, and at a magnitude greater,  $d^4$ . Speight, Kirchner, and Ardell et al [96,100-101] predicted the rate of coarsening based on the modification of Eq. 1 for grain boundary diffusion by the following,

$$d^4 - d_0^4 = k(T)t \quad (12)$$

The general form can ultimately be written as,

$$d^n - d_0^n = k(T)t \quad (13)$$

After evaluating the coarsening kinetics for the TiB phase using the aforementioned equations, and also looking at  $n=2$  to 5, it was apparent the particular equation up to  $n=5$  did not accurately describe the diametric and length coarsening. Figure 45 illustrates the inaccuracy in fit for the experimental data attained in the TiB coarsening study utilizing the LSW equation, shown for  $T = 1100^\circ\text{C}$  in this example. A slope of around 1 is necessary for an accurate mathematical description. The most likely reason for the inaccuracy in fit could be attributed to the assumptions that go along with the equation. In particular, the equation is said to be valid for spherical or equi-axed particle growth, and since the TiB phase is needlelike in morphology, the relationship could not be found at the typical lower powers, i.e.  $n=2$  to 4. D. Hu et al [99] was successful in using the coarsening equation at  $n=4$  for describing TiC coarsening, which has an equiaxed structure. Also, the inability to use this equation for typical diffusion-control growth of the TiB needle can be attributed to the relatively slow rate of coarsening of the TiB phase as a  $f(T,t)$ .

Therefore, using a stereological approach of modeling the TiB morphology as ellipsoidal for volumetric comparative study to a sphere [102], the effective diameter,  $D_{\text{eff}}$  was calculated.

$$D_{\text{eff}} = D_{\text{eq}} / (2/3\lambda)^{1/3} \quad (14)$$

where  $\lambda$  is aspect ratio, and  $D_{\text{eq}}$  is the TiB equivalent diameter attained from the image analysis process.

Using this method of analysis gave a linear relationship of  $D_{\text{eff}}$  versus  $\log t$ , see Fig.46, as a function of the temperatures studied. Inserting  $D_{\text{eff}}$  into the general equation 13 for LSW coarsening, and using non-typical  $n=6, 8$  and  $8$  at temperatures  $900, 1100$ , and  $1300^{\circ}\text{C}$ , respectively, a fit could be found. Fig. 47 illustrates the goodness of fit log-log plot for the aforementioned  $n$  values. This difference in  $n$  values at temperatures can most likely be attributed to the difference in coarsening kinetics and driving mechanisms that are occurring below ( $900^{\circ}\text{C}$ ) and above ( $1100$  and  $1300^{\circ}\text{C}$ ) the  $\beta$ -transus. The beta phase, with a bcc structure, above the  $\beta$ -transus allows for an increase in diffusion rate versus the alpha phase with hcp structure. Therefore, the author believes the coarsening kinetics for TiB phase is a non-typical case for study, as compared to past work that has utilized standard LSW [96-98] and modified versions of LSW [96, 100-101].

Other researchers have found similar non-typical LSW coarsening results for other particulates. In a study conducted at Taiwan University, Wen-Cheng et al characterized Mo particulate coarsening within an

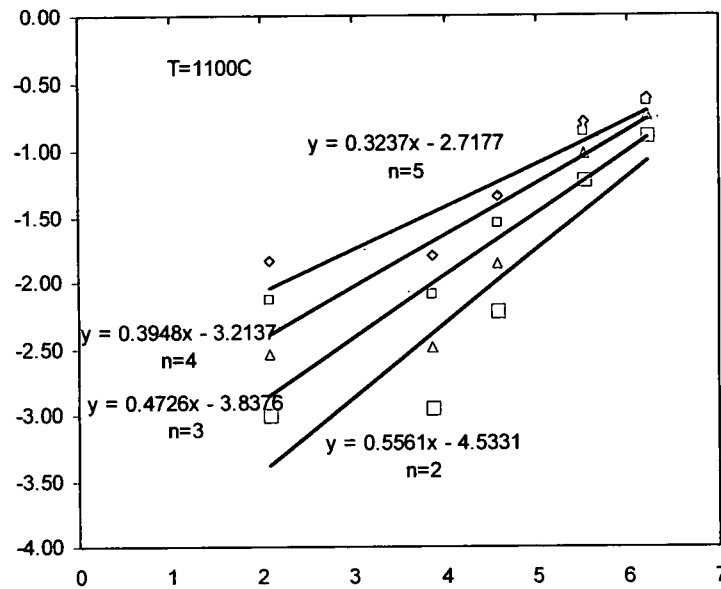


Figure 45 Goodness of fit for TiB coarsening using LSW equation up to  $n=5$ , for  $1100^{\circ}\text{C}$ .

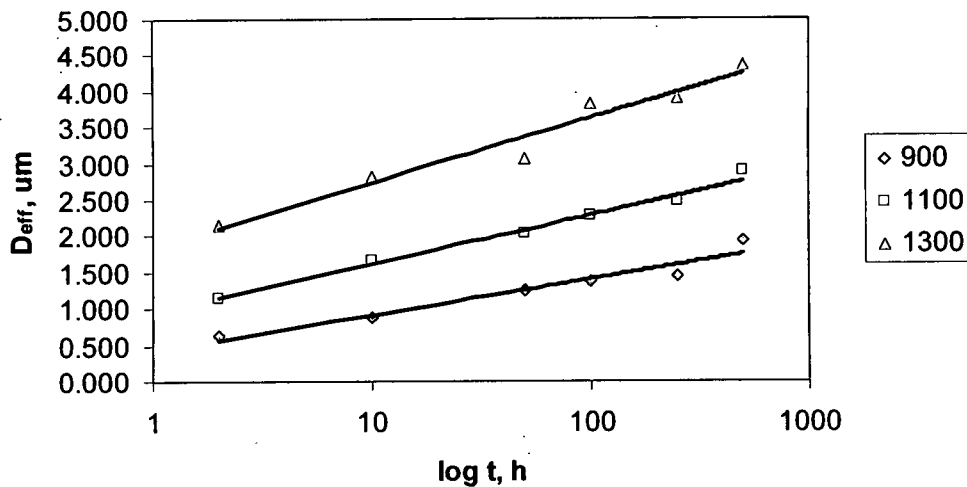


Figure 46 Coarsening of effective diameter,  $D_{\text{eff}}$ , for the TiB phase as a function of  $f(t, T)$ .



alumina composite. The results revealed that Mo particulates did not grow via the traditional Ostwald ripening process with  $n$  value less than 4. Instead, there appeared to be a different coarsening-controlling

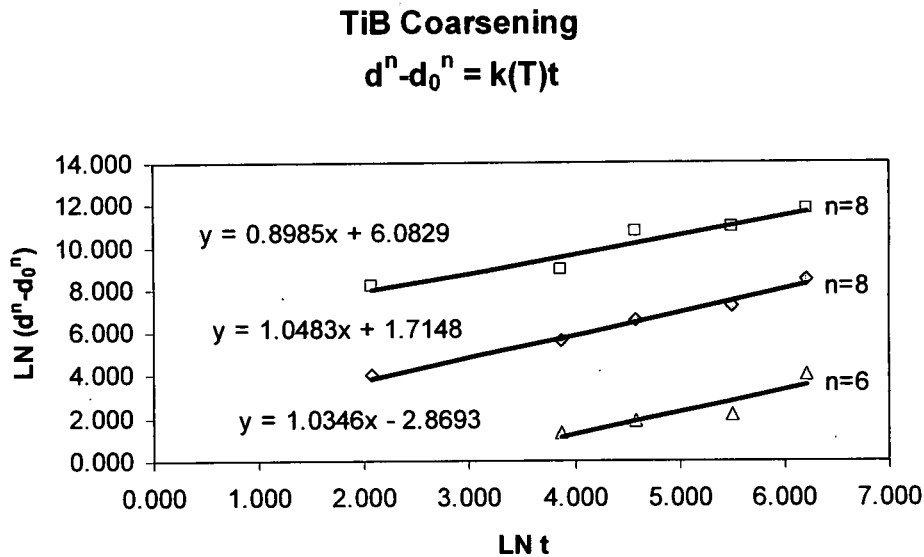


Figure 47 TiB coarsening modeled with LSW equation at  $n=6$  for 900C, and  $n=8$  for 1100 and 1300C.

mechanism, with time exponent,  $n$ , between 7 and 8. Therefore, a surface diffusion mechanism between the Mo particulates was considered, using the model discussed by Coblenz et al [103]

$$(d/d_0)^n \text{ proportional to } \delta D_s \gamma \Omega m (1/kT) \quad (15)$$

where  $D$  is the interface diffusion coefficient,  $\delta$  is the interface layer for diffusion,  $\gamma$  is surface energy, the  $\Omega$  is the atomic value for the particulate.

The time exponent,  $n$ , is in the range of 5 to 7 depending upon the contact shape between particles.

In like manner it could be proposed that the TiB phase follows a coarsening behavior whereby an interface diffusion mechanism between the TiB particulates are driving the dissolution and coarsening. This is consistent with earlier observations in Ti-TiB<sub>2</sub> diffusion couples. A dense compact TiB layer increased in thickness with increasing time and temperature via a parabolic rate, consistent with volume diffusion of B. However, TiB needles also grew in advance of this continuous layer at a rate much higher than could be explained by bulk diffusion [104]. The present analysis of interface diffusion provides a plausible description for this previously unexplained result. Also, the present analysis is the first time that a credible suggestion of interface diffusion in the Ti-B material system has been developed. The standard LSW equation for modeling assumes a spherical particle. Even though the TiB needles were volumetrically modeled as spheres via the effective diameter,  $D_{eff}$ , the differentiating rates of coarsening of the lengths and diameters is not factored in with the standard LSW models. The preferential growth of the TiB to a needle-like morphology, and increase in aspect ratio as a function of time and temperature should also be considered when modeling the continued growth of the TiB over time.

## Conclusions

The TiB phase precipitates *in-situ* to form a needle-like morphology, with a initial aspect ratio of approximately 10. The highest volume percent TiB is present on the order of micron scale (2-10  $\mu\text{m}$ ), with a lower volume percentage of sub-micron scale (0.4-0.9  $\mu\text{m}$ ) randomly dispersed throughout the matrix, even after extruding the material. The coarsening kinetics of the TiB phase can be attributed in-part to the classical Ostwald-ripening effect, whereby, the finer sub-micron needles eventually dissolve, and only micron-scale TiB preferentially remain for 1100 and 1300°C. It was interesting that the amount of finer sub-micron TiB phase increases after exposure to 900°C for only 2 hours, which can be attributed to super-saturated B within the Ti-6Al-4V matrix after powder processing. The TiB phase coarsening study at times from 2 to 500 hours and temperatures of 900, 1100, and 1300°C, respectively, indicated a non-typical fit to the frequently used LSW model for particle coarsening. The LSW model assumes an equiaxed or spherical type particle for coarsening, and has been shown to fit quite well in many cases [6,99] where  $n=3$  or 4 for volume or grain boundary diffusion-controlled coarsening. However, using a volumetric modeling of the TiB phase as ellipsoidal for attaining  $D_{\text{eff}}$ , a fit could be found at  $n=6$  and 8 depending on the anneal temperature.

The following conclusions can be made from the study:

- Evidence of classical Ostwald-Ripening of the TiB needles occurs under the times and temperatures used in the study.
- Coarsening of the TiB needles using the ellipsoidal model for effective diameter follows a diffusion-controlled growth via the classical LSW model for coarsening,  $r^n - r_0^n = k(T)t$ , but using non-typical exponents of  $n=6$  and  $8$  below and above the beta transus, respectively.
- Explanation of the coarsening kinetics of the TiB phase can be given in terms of interface diffusion, which also supports earlier studies of TiB growth utilizing diffusion couples.
- Super-saturated B is expelled from within supersaturated alloy, forming additional sub-micron TiB needles after 900C/2h exposure.
- A decrease in point  $p$  as a function of  $t$  &  $T$  is evident, and an increase in interparticle spacing as a function of  $t$  &  $T$  is also apparent.
- A shift to larger mean size (equivalent diameter and length) is evident in the distribution curves. The shift is more dramatic at 1300°C vs. 900°C as a function of time.
- TiB forms *in-situ* in a needle-like morphology, whereby the length coarsening at a faster rate than the diameter.

## Recommendations

This study focused on the TiB phase in a powder metallurgy titanium-boron material system. This particular system produced a tri-modal size-scale distribution for the TiB phase. The evolution of the TiB size-scales (i.e. nano-, micro-, primary) are governed by different thermodynamic mechanisms, which have strong implications on the total material system microstructural evolution. The nano-TiB is generally produced via entrapment of the B in the solution and subsequent exposure to increased temperatures forcing out the remaining B in the form of TiB. The highest volume of TiB is in on the order of micro-TiB. The origin of this size scale can be explained by the eutectic reaction that is present in the Ti-6Al-4V-1.7B phase diagram. Finally, the largest TiB on the order of 100-500  $\mu\text{m}$  in length, which were disregarded in this particular study, forms in the liquid phase early on as primary TiB, allowing for non-equilibrium particle growth. The author recommends thermal stability analysis of a Ti-B alloy without the presence of primary TiB, utilizing the same procedure as described in this paper, and subsequent coarsening modeling.

## REFERENCES

1. Titanium Alloy Guide, RMI Titanium Company, copyright 2000.
2. M.J. Donachie, Titanium: a Technical Guide, 2<sup>nd</sup> Ed., Materials Park, OH: ASM International, c2000.
3. ASM Handbook, Property and Selection: Nonferrous Alloys, vol. 2, 2000.
4. R.Boyer and S.Lampman, Materials Property Handbook Titanium Alloys, ASM International, 1998.
5. Ibid
6. S.L.Semiatin, B.C.Kirby and G.A.Salishchev, *Metall and Met Trans A: Phys Metall and Mat Sc*, v35A, n9, Sept, 2004, p2809-2819.
7. J.W.Martin, R.D.Doherty and B.Cantor: *Stability of Microstructures in Metallic Systems*, Cambridge University Press, Cambridge, United Kingdom, 1997.
8. M.McLean: *Met Sci.*, 1978, v12, pp113-22.
9. S.L.Semiatin, V.Seetharaman, I.Weiss: *Mater Sci Eng A*, 1999, vA263, pp 257-71.

10. S.L.Semiatin, J.F.Thomas, Jr. and P.Dadras: *Metall Trans A*, 1983, v14A, pp. 2363-74
11. E.B.Shell and S.L. Semiatin: *Metall Mater Trans A*, 1999, v30A, pp. 3219-29.
12. A.A.Korshunov, F.U.Enikeev, M.I.Mazurskii, G.A.Salishchev, A.V.Muravlev, P.V.Chistyakov and O.O.Dimitriev: *Russ Metall*, 1994, v3, pp.103-08.
13. G.Welsch, I.Weiss, D.Eylon and F.H.Froes: in *Advances in the Science and Technology of Titanium Alloy Processing*, TMS, Warrendale, PA, 1997, pp. 169-83.
14. S.L.Semiatin, S.L.Knisley, P.N.Fagin, F.Zhang, D.R.Barker: *Metall Trans A*, v34A, October 2003.
15. G.W.Kuhlman: in *Microstructure/Property Relationships in Titanium Aluminides and Alloys*, Y-W Kim and RR Boyer, eds, TMS, Warrendale, PA, 1991, pp.465-91.
16. D.Eylon, C.M.Pierce, *Metall Trans 7A*, 1976, 111.
17. A.T.K. Assadi, H.M.Flower, D.R.F.West, *Met Technol* 6, 1979, 8.
18. Donachie, *Ibid*.
19. ASM Handbook, *Forming and Forging*, v14, 1998.
20. Donachie, *Ibid*.
21. D.Eylon, Graduate Studies, University of Dayton, Dayton, OH, USA.
22. S.L.Semiatin, J.F.Thomas, P.Dadras, *Metall Trans 14A*, 1983, 2363.
23. S.L.Semiatin, G.D.Lahoti, *Metall Trans 12A*, 1981, 1705.

24. J.J.Jones, R.A.Holt, C.E.Coleman, *Acta Metall* 24, 1976, 911.
25. ASM Handbook, Property and Selection: Nonferrous Alloys, vol. 2, 2000.
26. Daniel Eylon and Kuang-O (Oscar) Yu, Titanium – First Six Decades: Past, Present and Future: International Titanium Conference, P.R.China.
27. International Titanium Association, A Historical Perspective, Rev2005.
28. Eylon and Yu, Ibid.
29. Private Conversation with R.R.Boyer.
30. Eylon and Yu, Ibid.
31. S.Abkowitz. The Emergence of the Titanium Industry and the Development of the Ti-6Al-4V Alloy, Journal of Metals Monograph Series, v1, TMS, 1999.
32. Eylon and Yu, Ibid.
33. D.B.Miracle ASM Handbook, Composites, vol.21, 2001.
34. D.B.Miracle, Ibid.
35. ASM Handbook, Composites, vol.21, 2001, A.Pandey.
36. A.Pandey, Ibid.
37. T.Saito, *Adv. Perform. Mater.*, v2, 1995, p 121.
38. T.Yamaguchi, H.Morishita, S.Iwase, S.Yamada, T.Furuta, and T.Saito, "Development of P/M Titanium Engine Valves," SAE Technical Paper 2000-01-0905, SAE International, 2000.



39. F.H.Froes and R.H.Jones, *14<sup>th</sup> International Titanium Application Conf. and Exhibition*, Oct 1998, Monte Carlo, Monaco.
40. A.E.Paltry, H.Margolin, and J.P.Nielsen, *Transactions of the ASM*, pp.313-327, 1953.
41. A.R.B.Brown, H.Brooks, K.S.Jepson, and G.I.Lewis, *Journal of the Institute of Metals*, v.91, 1962-53.
42. K.S.Chandran and D.B.Miracle, *JOM*, pp. 32,41, May 2004.
43. S.Abkowitz, S.M.Abkowitz, H.Fisher, and P.Schwartz, *JOM*, pp. 37-41, May 2004.
44. S.Abkowitz, *Ibid*.
45. McDonnell Douglas report MDC CRAD-9408-TR-2679, *High Speed Research-Airframe Technology*, yearly report, 1997.
46. T.Saito, *JOM*, pp. 33-36, May 2004.
47. T.Saito et al, "Development of P/M Titanium Engine Valves", *Proc. SAE 2000 Technical Paper Series*, 2000-01-0905, March 2000
48. T.Saito, *Ibid*.
49. S.Tamirisakandala, R.B.Bhat, V.A.Ravi, and D.B.Miracle, *JOM*, pp. 60-63, May 2004.
50. R.B.Bhat, S.Tamirisakandala, D.B.Miracle, V.A.Ravi, *Met. Mater. Trans. A*, v36A, 2005.
51. R.B.Bhat, *Ibid*.

52. R.B.Bhat, S.Tamirisakandala, D.J. McEldowney, D.B.Miracle,  
Preceedings: Titanium-Boron International Workshop, UES, Inc 2005.
53. R.Banerjee, P.C.Collins, A.Genc, H.L.Fraser, *Acta Mater.* A358 (2003)  
343-349.
54. S.Tamirisakandala, R.B.Bhat, D.B.Miracle, S.Boddapati, R.Bordia,  
R.Vanover, V.K.Vasudevan, *Scripta Mater.* (2005).
55. R.Banerjee, *Ibid.*
56. S.Tamirisakandala, R.B.Bhat, D.B.Miracle, Patent pending.
57. R.Boyer, *Ibid.*
58. O.M.Ivasishin, Unpublished Research, Kurdyumov Institute for Metal  
Physics NASU, Kyiv, Feb 20004.
59. S.Sahay, K.Ravichandran, and R.Atri, *J.Mater.Res.* v14 no.11 Nov.1999
60. S.Sahay, *Ibid.*
61. K.S.Ravi Chandran, K.B.Panda, and S.Sahay, Development of  
Titanium Boride Whisker (TiB<sub>w</sub>) Reinforced Titanium Composites:  
Processing, Properties, Application Prospects and Research Needs.
62. T.Saito, *Advanced Performance Materials*, 2, 121-144 (1995).
63. S.Tamirisakandala, R.B.Bhat, D.J.McEldowney, D.B.Miracle, MS&T,  
pp. 185-193, Conf. Proc. TMS Fall 2003.
64. T.Saito, T.Furuta, H.Takamiya, Proc. 8<sup>th</sup> World Conf. on Titanium, P.A.  
Blenkinsop ed., TIM London, 1995.

65. J.A.Philliber, Microstructural Evolution and Mechanical Behavior of beta-Titanium Alloys Reinforced with *in-situ* Grown TiB, PhD Dissertation, University of California, August 1997.
66. D.J.McEldowney, S.Tamirisakandala, D.B.Miracle, Heat Treatment Study of Titanium-Boron Alloys, *Met Trans* submitted 2006.
67. R.Ding, Z.X.Guo, A.Wilson, Materials Science & Engineering A, A327 (2002) 233-245.
68. S.Tamirisakandala, R.B.Bhat, J.S.Tiley, D.B.Miracle, *Scripta Mat*, 53 (2005) 1421-1426.
69. S.Tamirisakandala, D.B.Miracle, patent pending.
70. Private conversation with R.Boyer, M.LaSonde, B.Crawford.
71. S.Gorsse, D.B.Miracle, *Acta Mater*, 51 (2003) 2427-2442.
72. W.O.Soboyejo, R.J.Lederich, S.M.Sastry, *Acta Metall Mater*, v42, no.8, pp. 2579-2591, 1994.
73. J.A.Philliber, F.C.Dary, F.W.Zok, C.G.Levi, Proceedings Fall 1994 Materials Week, Chicago, IL. (TMS 1995), 213-224.
74. V.C.Nardone, J.R.Strife, *J. Mater. Sci.*, 22 pp. 592-600 (1987).
75. W.D.Callister, *Material Science and Engineering: An Introduction*, 4<sup>th</sup> ed, J.Wiley & Sons, 1997.
76. C.J.Boehlert, C.J.Cowen, S.Tamirisakandala, D.J.McEldowney, D.B.Miracle, *Scripta Mater*. 55 (2006) 465-468.

77. G.Bao, J.W.Hutchinson, and R.M.McMeeking: *Acta Metall. Mater.* 39 (1991) 1871-1882.
78. R.W.Hertzberg, *Deformation and Fracture Mechanics of Engineering Materials*, 3<sup>rd</sup> Ed, J.Wiley & Sons, 1989.
79. E.O. Hall: *Proc. Phy. Soc. B* 64 (1951) 747-53.
80. N.J. Petch: *J. Iron Steel Inst.* 174 (1953) 25-8.
81. J.Murray, ed., *Phase diagrams of binary titanium alloys*, ASM Int, Materials Park, OH, 1990.
82. T.S.Srivatsan, W.O.Soboyejo, R.J.Lederich, *Composites Part A*, 28A (1997) 365-376.
83. D.Hull and T.W.Clyne, *An introduction to Composite Materials*, 2<sup>nd</sup> Ed, Cambridge Solid State Science Series, Cambridge (1996).
84. T.W.Clyne and P.J.Withers in *An Introduction to Metal Matrix Composites*, Cambridge University Press, Cambridge (1993).
85. H.L.Cox, *Br.J.Appl.Phys. K.M.*, *Scripta Metall.*, 1987, 21, 349-354.
86. V.C.Nardone, K.M.Prewo, *Scripta Metall.*, 1985, 20, 43-48.
87. M.Taya, R.J.Arsenault, *Scripta Metall.*, 1987, 21, 349-354.
88. P.K.Mallick. *Fiber-reinforced composites: materials manufacturing and design*. New York: Marcel Dekker, 1988.
89. E.E. Underwood, *Quantitative Stereology*, Addison-Wesley, NY, NY (1970).

R702032897

90. D.A. Porter and K.E. Easterling, Phase Transformations in Metals and Alloys, Van Nostrand Reinhold (UK) Ltd., 1984.
91. R.T. Dehoff, Acta Metall. V32, No.1, pp. 43-47, 1984.
92. V.A. Snyder, J. Alkemper and P.W. Voorhees, Acta Mater. 49 (2001) 699-709.
93. M. Lifshits and V.V. Slyosov, J. Phys. Chem. Solids, 19 (1961).
94. C. Wagner, Z. Elektrochem. 65 (1961) 581.
95. G.W. Greenwood: Acta Metall., 1956, v4, pp. 243-48.
96. A.J. Ardell, Acta Metall. 20 (1972) 61.
97. C.K.L. Davis, P. Nash, R.N. Stevens, Acta Metall., 28 (1979) 179.
98. P.W. Voorhees and M.E. Glicksman, Acta Metall., 32, (1984) 2001.
99. D. Hu and M.H. Loretto, Journal of Alloys and Compounds, 209 (1994) 167-173.
100. M.V. Speight, Acta Metall., 16 (1968) 133.
101. H.O.K. Kirchner, Metall. Trans., 2 (1971) 2861.
102. E.E. Underwood Quantitative Stereology, Addison-Wesley, 1970.
103. W.S. Coblenz, J.M. Dynys, R.M. Cannon, R.L. Coble, Proceedings of the 5<sup>th</sup> International Conf. on Sintering and Related Phenomena, ed. Kuczynski, Plenum Press, NY, 1983.
104. C. Rivello, D.B. Miracle, unpublished work, AFRL, 2002.